Magnetoconvection with Walls of Finite Electrical Conductivity

by

Ali Akhtari

A dissertation submitted in partial fulfillment
of the requirements for the degree of
Doctor of Philosophy
(Mechanical Sciences and Engineering)
in the University of Michigan-Dearborn
2024

Doctoral Committee:

Professor Oleg Zikanov, Chair
Assistant Professor Hugo Casquero
Professor Dewey Jung
Associate Professor Cheol Lee

Ali Akhtari
aakhtari@umich.edu
ORCID iD: 0000-0003-4522-7156

DEDICATION

To my family, teachers, and mentors – for lighting the path that led me here, and to all those who have guided and supported me throughout this journey.

ACKNOWLEDGEMENTS

This journey would not have been possible without the help and support of many people. First and foremost, I want to thank my advisor, Prof. Oleg Zikanov. His invaluable advice, endless encouragement, and great patience have been the foundation of my Ph.D. experience. His vast knowledge and experience have constantly inspired me, and I am deeply grateful to have had such a dedicated and passionate mentor guiding me through this journey.

I also want to thank Prof. Dmitry Krasnov, whose expertise with the numerical solver was essential to my work. His help and insights were crucial in overcoming many challenges. My heartfelt thanks also go to Ruslan and Linyan, whose support and willingness to answer every question I had were invaluable. Their friendship and collaboration made my Ph.D. journey much more rewarding.

This research was supported in part through computational resources and services provided by Advanced Research Computing at the University of Michigan, Ann Arbor and the University Computing Center at the Technical University Ilmenau.

Lastly, and most importantly, I want to express my deepest gratitude to Shekoufeh. Her immense support and unwavering encouragement were my anchor throughout this journey. Shekoufeh, your belief in me and your constant presence were vital in navigating the ups and downs of this endeavor.

To everyone who has been part of this journey, thank you for your contributions, support, and belief in me. This achievement is as much yours as it is mine.

Thanks for the financial support from US NSF (grant CBET 1803730 'Extreme magneto-convection').

TABLE OF CONTENTS

CHAPTER

LIST OF TABLES

TABLE

LIST OF FIGURES

FIGURE

ABSTRACT

A flow with combined effects of magnetohydrodynamics (MHD) and thermal convection is called magnetoconvection. Its presence drastically affects the nature of flows of electrically conducting fluids such as liquid metals and plasmas. This dissertation investigates magnetoconvection in systems with walls of finite electrical conductivity, a critical aspect in various advanced technologies. The study focuses on understanding the interaction between thermal convection and magnetic fields in electrically conducting fluids, such as liquid metals, within confined spaces. The research aims to provide insights into the flow dynamics and heat transfer characteristics, with particular attention to the effects of wall electrical conductivity.

Performing such numerical investigation required a robust and accurate numerical scheme and solver. Thus, using a well tested second order finite difference scheme, a new solver was developed. It is based on the Tensor-product-Thomas (TPT) method. This solver is able to approach and efficiently handle the boundary conditions associated with walls of finite electrical conductivity without iterative processes. The accuracy of the method is verified through comparisons with established results for both electrically conducting and insulating walls. This validation ensures the reliability of the numerical simulations conducted in subsequent chapters.

Having a verified and robust numerical solver, a parametric study of the effects of wall electrical conductivity on magnetoconvection is conducted. Different configurations are explored, including cases, where all walls have the same electrical conductivity, and the cases with only specific walls being electrically conductive. The results reveal significant changes in the flow field and heat transfer patterns, underscoring the necessity of considering wall conductivity in magnetoconvection studies.

Additionally, the dynamics of an isolated thermal plume affected by strong magnetic fields is studied. This study is conducted for two different plume generation configurations. One configuration results from a point heat source and the other from a line heat source (e.g. thin wire). In the first configuration, the effect of the magnetic field direction is also studied. The results showed that the direction of the magnetic field has a strong effect on the development of the flow. A transverse magnetic field results in a transient, oscillating plume, in which the transient behaviors will decrease by increasing magnetic field intensity. However, a vertical magnetic field results in a completely different behavior.

The plume generated by the hot wire also shows the transient, oscillating behavior when a transverse magnetic field is applied to the domain. Velocity and temperature time signals at a series of points were recorded. This data is intended to be used for future experiments, as preliminary experimental results showed a significant difference in the damping caused by the magnetic field.

This research contributes to the understanding of magnetoconvection in systems with finite wall conductivity, offering valuable insights into the effect of wall conductivity on the evolution of the internal magnetoconvection flows.

CHAPTER 1

Introduction

Magnetoconvection is the convection motion of electrically conducting fluids, e.g. plasma or liquid metals, in the presence of a magnetic field. It is a complex process, where the fluid's movement is influenced by both thermal convection, and by magnetic field. In such systems, the interaction between the fluid's thermal properties, its electrical conductivity, and the external magnetic field leads to a unique pattern of flow and heat transfer. This phenomenon is significant in flows found in nature and advanced technologies [1].

The dynamics of planetary cores and stellar convective shells are examples of the magnetoconvection flows found in nature in geophysical and astrophysical systems [2]. Technological flows in which magnetoconvection plays an important role can be seen in manufacturing of high-quality steels [3], liquid metal batteries [4, 5] and growth of semiconductor crystals [6]. Another technological example is liquid-metal breeding blankets used in future tokamak fusion reactors [7, 8]. These blankets will be tested in the International Thermonuclear Experimental Reactor (ITER).

In a tokamak fusion reactor, as shown in figure 1.1, the plasma, which is the site of the fusion reaction, is confined within a toroidal chamber. An intense toroidal magnetic field maintains the trajectories of charged particles within a torus. The field intensity can reach 5 to 10 T or even higher. The blanket system, a key part of a fusion reactor, surrounds the plasma and helps shield the rest of the reactor and its outer parts from heat and powerful neutrons created during fusion. It serves as a heat exchanger diverting the energy into an external electric power-generation circuit. It is also used to make tritium by reacting with neutrons emitted from the plasma [9]. A dis-

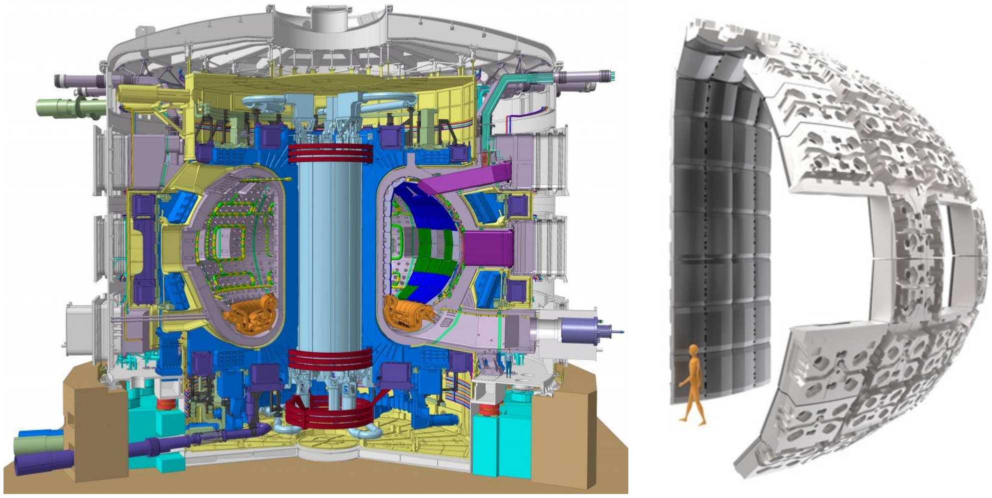

Figure 1.1: The ITER design and blanket modules on the left and right, respectively (www.iter.org).

tinctive feature of this blanket system is that the convection and magnetic field effects are both exceptionally strong.

Different concepts are proposed for designing these blankets: separately-cooled liquid-metal blanket e.g. helium-cooled lead-lithium (HCLL), self-cooled lead-lithium (SCLL), dual coolant lead-lithium (DCLL) and others [7, 8, 10, 11]. The liquid metal flow in separately-cooled and dual cooled blanket concepts has velocities in the order of $0.1 - 1\ mm/s$ and $10\ cm/s$, respectively [7]. Buoyancy effects is sufficient to drive the flow within separately-cooled blankets, however in DCLL blankets, the flow is driven by pumps, and convection is added to the pumping-caused circulation. Such low velocities are beneficial to reduce pressure drop in the liquid metal flow and therefore making such designs more feasible for reactors. Magnetoconvection flow of liquid metals inside those blankets in the presence of the magnetic field experiences a transformation that affects the flow field and thus the heat transfer.

This research is particularly relevant to the separately-cooled liquid-metal blanket concepts. In these blankets, compartments containing a liquid metal (e.g. a lead-lithium alloy) is in contact with flow of a separate coolant (for example, in HCLL blankets). The lead captures neutrons and other radiations from the plasma and returns their energy in the form of thermal agitation. The lithium undergoes a nuclear reaction with the neutrons from the plasma, regenerating tritium, the fuel for thermonuclear fusion. The alloy is then extracted from the blanket at a low flow rate to allow for tritium extraction in an appropriate facility. The heat absorbed by the liquid metal in these compartments is then transferred to the coolant. This will cause a natural convection flow, which is then influenced by the external magnetic field.

Due to presence of the magnetic field, an induced current pattern forms inside the electrically conducting liquid metal, which then results in an additional force called Lorentz force to be exerted on the flow. Interaction between Lorentz force and buoyancy force have significant impacts on the flow field. The consequences of these interactions include suppression of turbulence velocity fluctuations, development of a thin MHD boundary layer, and reducing the gradients of flow variables along the magnetic field which results in an anisotropic state or in extreme cases a quasi two-dimensional behavior.

This work consists of three parts, all of which involve magnetoconvection. In the first part, a new numerical scheme is introduced and validated for its accuracy in simulating magnetoconvection in a box in strong magnetic fields. Then this scheme is used to perform a parametric study of the effect of wall electrical conductivity on the magnetoconvection, in a long vertical box. Finally, in the last part, an isolated plume, which is common in convection flows, is studied in two different configurations. The general goal of this work is to form a better understanding of magnetoconvection of liquid metal in strong magnetic fields.

As it is shown later in chapter 5, the electrical conductivity of the walls can play a major role in the distribution of the electric currents in the flow field. Changed current loops in general means changed pattern and strength of currents flowing inside the domain. This leads to different pattern and strength of Lorentz forces –the force applied to the flow field as a result of interaction between the magnetic field and electrical current– thus changing the flow [12]. With electrically insulating walls, all current paths are forced to close in the flow domain. On the other hand, introducing electrical conductivity to the walls, allows some of current paths close in the wall rather than in the flow field.

A parameter which is used to describe electrical conductivity of the wall with respect to the that of the flow is the wall conductance ratio C_w (which is defined later in chapter 2). Usually high values of electrical conductivity for the liquid metals mean low values of the wall conductance ratio, even when the walls are actually made of electrical conducting material. Low values of wall conductance ratio directed previous numerical researches to mainly focus on the domains with electrically insulating walls. However, several theoretical [13, 14] and numerical [15, 16, 17, 18, 19, 20, 21, 22, 23, 24] studies of magnetoconvection were done without considering such assumption and predicted profound, and sometimes counter-intuitive, changes in flow structure even at a very small conductance ratio. Findings of the research presented in this dissertation supports such finding. It is later shown in this work that introducing electrical conductivity to the walls can change the flow field drastically and thus approximating the walls with low electrical conductivity with electrically insulating walls, is not accurate. As a result, it is of great importance to study and understand the effect of the wall electric conductivity on megnetoconvection in order to validate such simplifications.

Studying effects of the electrical conductivity of the walls requires solving the Maxwell equations in the walls as well as in the liquid flow. This can be achieved by extending numerical domain to the walls and solve discretized equations governing flow of electrical current as well as conserving electric charges in the interface between liquid and solid wall. Another way to conduct such simulations when the wall thickness (τ_w) is much smaller compared to the flow typical length scale (L) ($\tau_w \ll L$) is to use the so called thin-wall boundary condition. This assumption is explained further in chapter 2.

One of the consequences of using the thin-wall boundary condition is introduction of a non-conventional boundary condition on the electric potential at the interface of liquid and solid walls, which is now considered to be the boundary of the numerical domain. Traditionally, this boundary condition used to be solved iteratively, which is computationally expensive. This motivated the development of a new numerical method in collaboration with colleagues at the TU-Ilmenau. This method, which is described in chapters 3 and 4 allows us to solve the boundary condition directly without the need of iterations, which results in much faster simulations. After verifying the method for its accuracy in both electrically conducting and insulating walls, it is used to conduct a study of the effect of different configurations and values of the wall electrical conductivity on magnetoconvection flow in a tall box driven by a temperature difference between vertical walls.

Another interesting and not well studied phenomenon, is the internal magnetohydrodynamics (MHD) flow of liquid metal driven by a thermal plume. Plumes are common in convection flows. Their dynamics is drastically changed by the magnetic field. Here an isolated, artificially created plume in a box is studied the final part of this dissertation. It is divided into two separate studies. In the first one, the plume is generated by a point heat source located at the bottom quarter of a cubic box. In the second, the plume is generated by a vertical line heat source in an elongated box.

The rest of this dissertation is structured as follows. Physical model, governing equations, boundary conditions in non-dimensional form and the approximations used in developing such equations along with non-dimensional parameters governing the system are discussed in chapter 2. Chapter 3 explains the numerical scheme, which is used to descritize the equations in both the time and space domains and the setup of the numerical solver. Chapter 4 presents the Tensor-product-Thomas (TPT) numerical method developed and explained in [25] to solve electrical boundary conditions at walls with finite electrical conductivity, and the verification results of the developed method. The Direct Numerical Simulation (DNS) results for a long vertical box with different configurations of electrical conducting walls are presented and discussed in chapter 5. Finally, the results of the study on how liquid-metal thermal plumes behave are presented in chapter 6.

In the end, the concluding remarks of the research and ideas for future work are presented in chapter 7.

CHAPTER 2

Physical Model

2.1 General Equations

Flow of a Newtonian, viscous, electrically conducting, non-magnetizable, single-phase fluid (liquid metal) with constant physical properties contained in a box is considered. A constant uniform external magnetic field with strength of B_0 is imposed on the flow domain. The flow includes heat transfer and natural convection effects. Such system is governed by the equations of conservation of mass, momentum and energy, along with Maxwell equations governing electric and magnetic fields.

The conservation equations for an incompressible fluid are:

$$\boldsymbol{\nabla} \cdot \boldsymbol{u} = 0, \tag{2.1}$$

$$\frac{\partial \boldsymbol{u}}{\partial t} + (\boldsymbol{u} \cdot \boldsymbol{\nabla})\, \boldsymbol{u} = -\frac{1}{\rho} \boldsymbol{\nabla} p + \nu \nabla^2 \boldsymbol{u} + \boldsymbol{F}, \tag{2.2}$$

$$\rho C_p \left(\frac{\partial T}{\partial t} + \boldsymbol{u} \cdot \boldsymbol{\nabla} T \right) = \kappa \nabla^2 T + Q, \tag{2.3}$$

where $\boldsymbol{u}$, P , and T are the fields of velocity, pressure, and temperature, ρ and ν are the density and kinematic viscosity of the fluid, respectively, and $\boldsymbol{F}$ is the body force acting on fluid, which in this case, consists of buoyancy and Lorentz forces. The heat capacity and heat conductivity of the flow are c_p and κ, respectively, and Q represents the internal volumetric heating source.

The Maxwell's equations are:

$$\nabla \cdot \boldsymbol{E} = \frac{\rho_e}{\epsilon_0} \quad \text{(The Gauss's Law)}, \tag{2.4}$$

$$\nabla \cdot \boldsymbol{B} = 0, \tag{2.5}$$

$$\nabla \times \boldsymbol{E} = -\frac{\partial \boldsymbol{B}}{\partial t} \quad \text{(The Faraday's Law)}, \tag{2.6}$$

$$\nabla \times \boldsymbol{B} = \mu_0 \left(\boldsymbol{J} + \epsilon_0 \frac{\partial \boldsymbol{E}}{\partial t} \right) \quad \text{(The Ampére-Maxwell equation)}, \tag{2.7}$$

where $\boldsymbol{E}$, $\boldsymbol{B}$ and $\boldsymbol{J}$ are the electric field, magnetic field and electric current density, respectively. ρ_e is the charge density, ϵ_0 is the electric constant (also called the permittivity of free space), and μ_0 is the magnetic constant (also called the permeability of free space). Equation (2.5) is the solenoidal nature of magnetic field.

In addition to Maxwell's equations, we have:

$$\nabla \cdot \boldsymbol{J} = -\frac{\partial \rho_e}{\partial t}, \tag{2.8}$$

$$\boldsymbol{J} = \sigma \left(\boldsymbol{E} + \boldsymbol{u} \times \boldsymbol{b} \right) \quad \text{(The Ohm's Law)}, \tag{2.9}$$

$$\boldsymbol{F_L} = q \left(\boldsymbol{E} + \boldsymbol{u} \times \boldsymbol{b} \right) \quad \text{(The Lorentz force)}, \tag{2.10}$$

where σ is electric conductivity and q is the electric charge. Equation (2.8) shows the charge conservation.

In the MHD applications, the Maxwell's equations (2.4) - (2.7) can be significantly simplified. In an electrically conducting fluid, charge density ρ_e is extremely small and plays no significant role. It is assumed that any positive and negative charges are equilibrated on the time scale related to the speed of light, i.e., practically immediately in comparison to the typical time scale of the flow. Thus, the Gauss's law may be dropped and the charge conservation equation may be reduced to the simplified statement The electric portion of Lorentz force $q\boldsymbol{E}$ is small by comparison with the Lorentz force. The displacement currents are negligible by comparison with the current density in conducting fluids. Therefore, the Ampére-Maxwell equation reduces to the differential form of Ampére's law. Detailed derivations can be found in many textbooks, such as [1, 26].

Considering the mentioned simplifications, the following equations can be derived:

$$\nabla \cdot \boldsymbol{J} = 0, \tag{2.11}$$

$$\nabla \cdot \boldsymbol{B} = 0, \tag{2.12}$$

$$\nabla \times \boldsymbol{B} = \mu_0 \boldsymbol{J}, \tag{2.13}$$

$$\nabla \times \boldsymbol{E} = -\frac{\partial \boldsymbol{B}}{\partial t}, \tag{2.14}$$

$$\boldsymbol{J} = \sigma \left(\boldsymbol{E} + \boldsymbol{u} \times \boldsymbol{B} \right), \tag{2.15}$$

$$\boldsymbol{F}_L = \boldsymbol{J} \times \boldsymbol{B}. \tag{2.16}$$

2.2 Approximations

In conducting numerical and theoretical studies of magnetoconvection flows of liquid metal in the technical settings, usually three approximations are made [11]. These approximations result in less complex governing equations. The first approximation is Boussinesq approximation, which neglects the variation of the physical properties of the liquid with temperature, except for density, for which a linear relation between density and temperature is assumed. The only term that contains this relationship is the buoyancy force term in the momentum equation.

The validity of this approximation is investigated by analysing the change in physical properties of the material by temperature. For example, considering mercury and a base temperature of 293, an increase in temperature by $30K$ results in relatively low change in all of the properties except for kinematic viscosity and thermal conductivity, for which the changes are less than 5%. For the studies of chapters 4 and 5, the maximum temperature difference in the flow domain is less than $5K$, which further enhances the Boussinesq approximation validity. Regarding the study of thermal plume described in chapter 6, the validity of Boussinesq approximation needs further attention due to higher temperatures in the domain.

The second approximation is the quasi-static (induction-less) approximation [1, 26, 27]. To explain this approximation further, consider a case with constant imposed magnetic field $\boldsymbol{B_0}$. In this case, the electric currents induced in the flow generate induced perturbations in the magnetic field $\boldsymbol{b}$. As a result, the total magnetic field $\boldsymbol{B}$ will be the sum of the imposed $\boldsymbol{B_0}$ and induced $\boldsymbol{b}$ magnetic fields $\boldsymbol{B} = \boldsymbol{B_0} + \boldsymbol{b}$. Using the quasi-static approximation, the induced perturbations in the magnetic field can be neglected, which implies a one-way interaction between magnetic field and fluid motion. This approximation requires that magnetic Reynolds number (Re_m) and magnetic Prandtl number (Pr_m) to be both small:

$$Re_m = \sigma\mu_0 UL \ll 1, \qquad Pr_m = Re_m/Re = \sigma\mu_0\nu \ll 1, \tag{2.17}$$

where μ_0, σ and ν are respectively magnetic permeability of vacuum, and electrical conductivity and kinematic viscosity of fluid. It is known that liquid metal flows in technical and laboratory settings typically satisfy the conditions. For example for mercury (Hg) $Pr_m = 0.14 \times 10^{-6}$, for gallium (Ga) $Pr_m = 1.3 \times 10^{-6}$ and for PbLi $Pr_m = 0.21 \times 10^{-6}$ [28]. Regarding small values of Re_m, since the model remains accurate up to $Re_m \sim 0.1$, flows with Reynolds number Re up to 10^5 satisfy this condition. Experimental and numerical studies verify this approximation [11]. Detailed derivation and applicability of this approximation is discussed in [1].

The last approximation ignores the heat generation caused by Joule and viscous dissipation and drops the corresponding terms in energy equation. This approximation is justified by the very high electrical conductivity of the liquid, very low values of Eckert number $Ec \equiv U^2 \left(c_p \Delta T\right)^{-1}$, and/or by high applied thermal load. The Eckert number is the ratio of the advective mass transfer to the heat dissipation potential, and it demonstrates the influence of self-heating of a fluid as a result of dissipation effects. The thermoelectric Thomson, Peltier, and Seebeck effects can also be neglected with exception of the applications characterized by extreme temperature gradients.

2.3 Non-dimensional Governing Equations

Using said approximations, the non-dimensional equations are:

$$\boldsymbol{\nabla} \cdot \boldsymbol{u} = 0, \tag{2.18}$$

$$\frac{\partial \boldsymbol{u}}{\partial t} + (\boldsymbol{u} \cdot \boldsymbol{\nabla})\, \boldsymbol{u} = -\boldsymbol{\nabla} p + \sqrt{\frac{Pr}{Ra}} \left(\nabla^2 \boldsymbol{u} + Ha^2 \boldsymbol{j} \times \boldsymbol{e}_B\right) - T\boldsymbol{e}_g, \tag{2.19}$$

$$\frac{\partial T}{\partial t} + \boldsymbol{u} \cdot \boldsymbol{\nabla} T = \sqrt{\frac{1}{RaPr}} \left(\nabla^2 T + q\right), \tag{2.20}$$

$$\boldsymbol{j} = -\boldsymbol{\nabla}\phi + \boldsymbol{u} \times \boldsymbol{e}_B, \tag{2.21}$$

$$\nabla^2 \phi = \boldsymbol{\nabla} \cdot (\boldsymbol{u} \times \boldsymbol{e}_B) \tag{2.22}$$

In these equations, $\boldsymbol{u}$, p, T, q, $\boldsymbol{j}$ and ϕ are respectively dimensionless fields of velocity, pressure, temperature, volumetric heat generation, electric current density and electric potential. $\boldsymbol{e}_g$ and $\boldsymbol{e}_B$ are the unit vectors in the direction of gravity and magnetic field respectively. The equations are non-dimensionalized using the typical domain size L, strength of the imposed magnetic field B_0 and the free-fall velocity $U \equiv \sqrt{g\beta\Delta T L}$ (here β and g are the thermal expansion coefficient and the acceleration of gravity respectively). Electric potential and electric current density are scaled using the combinations UB_0L and σUB_0. Typical time scale is L/U. Typical temperature scales to be defined shortly.

If the flow is driven by a temperature difference between the walls and there is no volumetric heat generation (Cases discussed in chapters 4 and 5) temperature difference between these walls $\Delta T = T_{hot} - T_{cold}$ is used in the process of deriving the dimensionless equations. On the other hand for the case of thermal plume explained in chapter 6, the volumetric average of total heat generation, is used to define a characteristic temperature difference $\Delta T = q_{tot} L^2 \left(\forall k\right)^{-1}$, in which q_{tot} is total volumetric heat generation rate, $\forall$ is the total volume of the domain, and k is the heat conductivity of the liquid. This temperature difference is equivalent to the temperature difference which results in a pure conduction heat transfer across the domain equal to the heat generated by the source.

Typical scales used for the flows in upcoming chapters are as follows:

$$L \equiv \begin{cases} L_z \text{ (Distance between hot and cold walls)} & \text{Cases in chapter 4} \\ L_x \text{ (Distance between hot and cold walls)} & \text{Cases in chapter 5} \\ d \text{ (Heating sphere diameter)} & \text{Case 1 in chapter 6} \\ L_x/2 \text{ (Half distance between side walls)} & \text{Case 2 in chapter 6} \end{cases} \tag{2.23}$$

$$U \equiv \sqrt{g\beta\Delta T L} \tag{2.24}$$

$$t \equiv L/U \tag{2.25}$$

$$\Delta T \equiv \begin{cases} T_{hot} - T_{cold} \text{ (difference between walls)} & \text{Chapters 4 and 5} \\ q_{tot} L^2 \, (\forall k)^{-1} & \text{Chapter 6} \end{cases} \tag{2.26}$$

$$p \equiv \rho U^2 \tag{2.27}$$

$$\phi \equiv U B_0 L \tag{2.28}$$

$$j \equiv \sigma U B_0 \tag{2.29}$$

In these equations, L, U, t, ΔT, p, ϕ and j are typical scales for length, velocity, time, temperature, pressure, electric potential and electric current density. B_0 is the magnitude of the imposed magnetic field.

The non-dimensional parameters are the Reynolds, Prandtl, Rayleigh, Grashof and Hartmann numbers which are defined as follows:

$$Re \equiv \frac{UL}{\nu} \tag{2.30a}$$

$$Pr \equiv \frac{\nu}{\alpha} \tag{2.30b}$$

$$Ra \equiv \frac{g\beta\Delta T L^3}{\nu\alpha} \tag{2.30c}$$

$$Gr \equiv \frac{g\beta\Delta T L^3}{\nu^2} \tag{2.30d}$$

$$Ha \equiv BL\sqrt{\frac{\sigma}{\rho\nu}} \tag{2.30e}$$

where α and ρ are respectively thermal diffusivity and mass density. Using the velocity scale (2.24), the Reynolds number can be written as:

$$Re \equiv \frac{UL}{\nu} \equiv \sqrt{\frac{Ra}{Pr}} \equiv \sqrt{Gr} \tag{2.31}$$

The boundary conditions for velocity at all walls are no-slip boundary condition ($\boldsymbol{u} = 0$). The temperature boundary condition for each wall can be either constant temperature $T = const.$ or zero heat flux (i.e. thermally insulating wall) $\partial T/\partial n = 0$. The thermal boundary conditions used for each study will be further explained in the corresponding chapters.

The last set of boundary conditions is related to the electric potential. One of the goals of this work is to understand the effect of finite electric conductivity of walls on magnetoconvection flow, when walls are considered to be thin so we can use the approximate thin-wall boundary condition. As a result of thin walls assumption, the distribution of the electric potential across the walls can be ignored. This approximation enables us to use a boundary condition for electric potential at the boundary between fluid and walls instead of solving the elliptic equation for electric potential in both fluid domain and walls. This so-called thin-wall boundary condition, which was initially proposed in [29], is defined as follows:

$$\left.\frac{\partial\phi}{\partial n}\right|_{wall} = C_w \nabla_\perp^2 \phi\big|_{wall} \tag{2.32}$$

where:

$$C_w = \frac{\sigma_w \tau_w}{\sigma L} \tag{2.33}$$

is the wall conductance ratio, the ratio between the total electric conductance of wall and the liquid. In these equations, σ_w is the electric conductivity of the wall, n is the outward-facing normal to the boundary and $\nabla_\perp^2$ is the two-dimensional Laplacian in the plane of the boundary.

The physical meaning of (2.32) is that the normal component of electric current carries electrical charges into the thin wall and while the electrical charge is conserved, it redistributes tangentially in the wall. Different values of C_w result in different electric boundary conditions at walls, with limits of $C_w = 0$ and $C_w = \infty$ corresponding to perfect electrically insulating and conducting cases. However because σ is high for liquid metals, and it typically results in C_w to be small, a perfectly electrically conducting wall is rarely relevant.

It is important to discuss the more complex situation when $C_w \to 0$ in more detail. This limit is often used to justify the idealization of a perfectly insulating wall. A more careful analysis reveals the special role of the MHD boundary layers, through which the electric currents induced in the fluid are predominantly closing. A non-negligible fraction of the currents is redirected into the wall if the wall's electric conductance is not much smaller than the conductance of the adjacent boundary layer, rather than of the entire flow domain assumed in the definition (2.33). The redirection means a reduction of the cumulative resistance to the flowing electric currents, which is expected to result in non-negligible increase of the magnitude of the currents and, thus, change of the Lorentz force.

Two types of MHD boundary layers are identifiable in a rectangular flow domain with an imposed magnetic field parallel to one set of walls. Thin (of the thickness $\delta_{Ha} \sim Ha^{-1}L$) Hartmann boundary layers form near the walls perpendicular to the magnetic field. Sidewall boundary layers of thickness $\delta_{Sw} \sim Ha^{-1/2}L$ develop at the walls parallel to the field. The logic leading to the definition (2.33) is, strictly speaking, not valid here, because the wall is not necessarily much thinner than the MHD boundary layer. As a qualitative estimate, however, we can use the ratio between the conductances of the wall and the adjacent layer:

$$C_w^{Ha} \equiv \frac{\sigma_w \tau_w}{\sigma \delta_{Ha}} = C_w Ha \qquad \text{Hartmann layer} \tag{2.34}$$

$$C_w^{Sw} \equiv \frac{\sigma_w \tau_w}{\sigma \delta_{Sw}} = C_w Ha^{1/2} \qquad \text{Sidewall layer} \tag{2.35}$$

A significant effect of the wall conductivity on the flow is expected when at least one of these coefficients is not small. The situation is especially acute for the Hartmann walls. Considering that $Ha \sim 10^4$ is typical for blanket applications, even very small conductivity of the Hartmann wall may significantly affect the flow.

CHAPTER 3

Method

3.1 Discretization approach

The equations (2.18) - (2.22) are solved numerically using the finite difference method described in [30] and [31] and further extended in [25] to support direct solution of problems with thin wall boundary conditions (2.32). The spatial discretization scheme is of the second order and nearly fully conservative, conserving mass, momentum, internal energy and electric charge exactly, and the kinetic energy with a dissipative 3rd-order error. The time discretization is semi-implicit and based on the Adams–Bashforth/backward-differentiation method of the second order. For the cases discussed in chapters 4 and 5, all terms are treated explicitly except for the diffusive term in (2.20). Implicit treatment of the diffusive term in (2.20) alleviates the severe limitation on the time step imposed on fully explicit schemes by small Pr. For the thermal plume cases discussed in chapter 6, the time discretization is also implicit for the viscous terms. Using the projection method for pressure and incompressibility at every time step, either three or six elliptic equations – velocity components, temperature, pressure and electric potential – are solved using the Tensor-product-Thomas (TPT) method.

In the TPT method, eigenvalue decomposition of the discretized equations is done in two directions and in the third direction a tridiagonal matrix is solved using the Thomas algorithm. An explanation of the TPT method applied to a conventional elliptic problem can be found in [32]. The unconventional boundary condition for the thin-walls impacts the separability of the governing equation. To solve that, the discretized boundary condition normal to directions of the eigenvalue decomposition and their corresponding coefficients in the matrix is changed so that the discretized equation remains separable and in the third direction the eigenvalue transformation is applied. A more detailed description of the discretized equation and the matrix components calculation can be found in chapter 4.

3.2 Computational grid

The computational grids for which the final results are reported, are chosen based on the grid-sensitivity study done for each problem. The distribution of the grid points in the spacial domain is controlled by the number of grid points, and using two different methods of point clustering. Points are either positioned with equal distance from each other (uniform grid) or based on the coordinate transformations which are used to generate clustered grid points. One of the challenges to the computational grid, is the need to resolve the velocity and thermal boundary layers. In magnetoconvection, resolving the Hartmann layer is especially difficult due to the fact that the width of this layer is estimated as $\delta_{Ha} \sim 1/Ha$. In the flows in a strong magnetic field, Hartmann layer can be extremely thin. As a result the two following grid clustering method were used.

The first one is a linear combination of uniform grid and Chebyshev transform and the second one is the tanh transformation. Assuming the walls are at $x_i = \pm L_i/2$, transformations are defined as follows:

$$x_i = \frac{L_i}{2}\left[\gamma \sin\left(\frac{\pi}{2}\xi\right) + (1-\gamma)\xi\right], \tag{3.1}$$

$$x_i = \frac{L_i}{2}\frac{\tanh(A\xi)}{\tanh(A)}, \tag{3.2}$$

where $-1 \le \xi \le 1$ is the transformed coordinate, in which the grid is uniform. γ is the constant determining the mixture of the uniform and Chebyshev-Gauss-Lobatto grids (the typical value is $\gamma = 0.96$), and A is the constant determining the degree of tanh grid clustering, typically taken in the range between 2 and 3.5.

The coordinate transformation used in each direction can be different, and is chosen based on the flow regime inside the box. In all of the computational grids, Hartmann layer is resolved by not less than 3 grid points. It is worth mentioning that the developed solver is capable of solving any computational grid with arbitrary grid points.

The time steps Δt are chosen to be not bigger than 50% of the value which causes the solution to become numerically unstable.

3.3 Simulation procedure

Simulations were started from initial conditions which consists of random velocity fluctuations with uniform distribution and a linear temperature profile representing pure conduction profile between walls with constant temperature in cases with temperature difference between walls (chapters 4 and 5) or a uniform temperature distribution for the case of volumetric heating (chapter 6). For simulations of thermal plume with non-zero magnetic field ($Ha \neq 0$), the result of the case with no magnetic field ($Ha = 0$) was used as initial condition.

The simulations are conducted for a duration long enough to capture any development in the flow, which can also happens after the flow appears to be in a fully-developed state. In order to observe the evolution of the flow and identify fully-developed flow, values of the Nusselt number $Nu(t)$ –the ratio of total heat transfer rate over pure conductive heat transfer rate–, the mean kinetic energy $E(t)$ and the total outward heat flux from the walls $q_{tot,out}(t)$ were used. These values are calculated using:

$$Nu = \langle Nu(t) \rangle_t = \left\langle \frac{1}{\forall} \int_V \left(u_m T \sqrt{Ra}\,\mathrm{Pr} - \frac{\partial T}{\partial m} \right) d\forall \right\rangle_{t_n}, \tag{3.3}$$

$$E = \langle E(t) \rangle_t = \left\langle \frac{1}{\forall} \int_V \left(u_x^2 + u_y^2 + u_z^2 \right) d\forall \right\rangle_{t_n}, \tag{3.4}$$

$$q_{tot,out} = \left\langle q_{tot,out}(t) \right\rangle_t = \left\langle \int_A \left(\frac{\partial T}{\partial n} \right) dA \right\rangle_{t_n} = \left\langle \int_V \left(\nabla^2 T \right) dV \right\rangle_{t_n}. \tag{3.5}$$

where, m is the direction parallel to temperature gradient and $\langle \cdot \rangle_t$, indicates time average over the last t_n non-dimensional time units. The value of t_n is calculated based on the time signals recorded from the flow field, to assure that it captures enough of transient fluctuations of the flow.

The time signals were recorded with a frequency not lower than 100 samples per time unit. The flow considered to be in a fully-developed state when $Nu(t)$, $E(t)$, or $q_{tot,out}$ are fluctuating around a steady mean. $Nu(t)$, $E(t)$ are also used as a mean to compare different flows with each other and study the effect of wall electrical conductivity on the flow. Numerical integrals in (3.3) - (3.5) are computed using the trapezoidal method.

CHAPTER 4

Tensor-Product-Thomas Solver and Verification

This chapter is based on the results published in [25]. In the first step toward conducting numerical studies of magnetohydrodynamics (MHD) flow with walls of finite electrical conductivity efficiently, a new solver was developed based on the Tensor-product-Thomas (TPT) method. This method is a modification of the classical tensor-product technique [33] of solution of separable elliptic equations in simple domains. A description of the method and a discussion of its efficiency can be found in [25, 32], while examples of its use in high-*Ra* hydrodynamics and magnetohydrodynamics are available in, e.g., [34, 35]. Therefore, only a brief discussion is provided here.

Eigenvalue decompositions of the discretization matrices of the one-dimensional differential operators in two directions are computed. The feature separating the TPT method from the classical tensor-product method is that the eigenvalue decomposition is not applied to the third direction typically chosen as the direction with the largest grid size. The equation resulting from this transformation has a tridiagonal matrix. The tridiagonal matrix equations are solved by the simple Thomas (double-sweep) algorithm (see, e.g., [36]).

The Dirichlet and periodic conditions are implemented by modifying the discretization matrix and the right-hand side so that these conditions are satisfied at the boundary points. For the Neumann and Robin conditions, the modification requires introduction of ghost points located outside the fluid domain. The equation and the boundary conditions discretized at the boundary using the ghost-point value are combined to exclude this value and obtain a two-point formula. The formula is used to modify the discretization matrices for the eigenvalue expansions and the tridiagonal matrix of the Thomas algorithm.

To demonstrate this procedure, consider the following Poisson equation for electric potential in a three-dimensional domain:

$$\frac{\partial^2\phi}{\partial x^2} + \frac{\partial^2\phi}{\partial y^2} + \frac{\partial^2\phi}{\partial z^2} = r, \tag{4.1}$$

where r is the right-hand side of (2.22). The second derivatives are discretized using second-order over an arbitrarily stretched (non-uniform) orthogonal three-dimensional grid. For example, the second derivative in x-direction at $i-$th point can be written as [37, 38]:

$$\left.\frac{\partial^2\phi}{\partial x^2}\right|_i \approx \left.\frac{\delta^2\phi}{\delta x^2}\right|_i \equiv 2\frac{(x_i - x_{i-1})\phi_{i+1} - (x_{i+1} - x_{i-1})\phi_i + (x_{i+1} - x_i)\phi_{i-1}}{(x_{i+1} - x_{i-1})(x_{i+1} - x_i)(x_i - x_{i-1})}, \tag{4.2}$$

where $\phi_i = \phi(x_i)$.

Equation (4.1) discretized using (4.2) results in:

$$\frac{\delta^2\phi}{\delta x^2} + \frac{\delta^2\phi}{\delta y^2} + \frac{\delta^2\phi}{\delta z^2} = r. \tag{4.3}$$

Now consider the Neumann boundary condition applied at the boundary $x = x_1$.

$$\left.\frac{\partial\phi}{\partial x}\right|_{x_1} = g1. \tag{4.4}$$

In order to solve for this boundary, ghost point x_0 is introduced such that $x_1 - x_0 = x_2 - x_1 = h_1$. Discretizing (4.4) by a central difference of the second order, the following is obtained:

$$\frac{\phi_2 - \phi_0}{2h} = g_1, \tag{4.5}$$

Dividing (4.5) by h_1 and rearranging the equation results in:

$$\frac{\phi_0}{h_1^2} = \frac{\phi_2}{h_1^2} - \frac{2g_1}{h_1}. \tag{4.6}$$

Now, expanding the first term in (4.3) using (4.2) at $i = 1$ results in:

$$\frac{\phi_2}{h_1^2} - \frac{2\phi_1}{h_1^2} + \frac{\phi_0}{h_1^2} + \left(\frac{\delta^2\phi}{\delta y^2} + \frac{\delta^2\phi}{\delta z^2}\right)_{x_1} = r_1. \tag{4.7}$$

Combining (4.6) and (4.7) leads to:

$$\frac{2\phi_2}{h_1^2} - \frac{2\phi_1}{h_1^2} + \left(\frac{\delta^2\phi}{\delta y^2} + \frac{\delta^2\phi}{\delta z^2}\right)_{x_1} = r_1 + \frac{2g_1}{h_1}, \tag{4.8}$$

which is realized by modifying the coefficient of the discretization matrix and the right-hand side vector.

A similar approach is used to implement the thin-wall condition (2.32). Unlike previously used approaches, such as that of [39], it is realizable via modification of matrix elements and does not require outer iterations. Considering thin-wall boundary condition at the boundary $x = x_1$, equation (2.32) can be written as:

$$\left.\frac{\partial\phi}{\partial x}\right|_{x_1} = C_w \nabla_{yz}^2\phi\Big|_{x_1}. \tag{4.9}$$

Discretizing this equation using the ghost point x_0 introduced similar to the example for Neumann boundary condition, the following is obtained:

$$\frac{\phi_2 - \phi_0}{2h} = C_w \left(\frac{\delta^2\phi}{\delta y^2} + \frac{\delta^2\phi}{\delta z^2}\right)_{x_1}, \tag{4.10}$$

Dividing by h_1 and rearranging the equation, results in:

$$\frac{\phi_0}{h_1^2} = \frac{\phi_2}{h_1^2} - \frac{2C_w}{h_1}\left(\frac{\delta^2\phi}{\delta y^2} + \frac{\delta^2\phi}{\delta z^2}\right)_{x_1} \tag{4.11}$$

Substituting (4.11) in (4.7), leads to:

$$\frac{2\phi_2}{h_1^2} - \frac{2\phi_1}{h_1^2} + \left(1 - \frac{2C_w}{h_1}\right)\left(\frac{\delta^2\phi}{\delta y^2} + \frac{\delta^2\phi}{\delta z^2}\right)_{x_1} = r_1. \tag{4.12}$$

Since two different approaches is used in the TPT method, equation (4.12), is written in two different forms. If the boundary is normal to the direction associated with Thomas-algorithm, equation (4.12) is used to modify the elements of discretization matrix and right-hand side vector. If the boundary is normal to one of the directions which eigenvalue decomposition is used, due to requirement of separability, the following form is used:

$$\frac{2\phi_2}{h_1^2}\frac{h_1}{h_1-2C_w}-\frac{2\phi_1}{h_1^2}\frac{h_1}{h_1-2C_w}+\left(\frac{\delta^2\phi}{\delta y^2}+\frac{\delta^2\phi}{\delta z^2}\right)_{x_1}=r_1\frac{h_1}{h_1-2C_w}. \tag{4.13}$$

This form of the thin-wall boundary condition can be implemented in the TPT method. Although, these two approaches are not identical due to discretization and round-off errors, the difference is expected to be negligible on sufficiently fine grids. A detailed explanation of the mathematical approach and the implementation of this method can be found in [25].

4.1 Validation

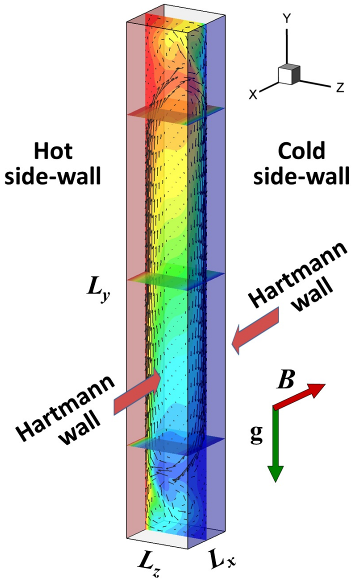

Figure 4.1: Principal flow configurations used for verification tests. Natural convection in a box. Flow geometry and temperature and velocity distributions found at $Gr = 3\times10^7$, $Ha = 570$, aspect ratio $A = 7.5$, and electrically insulating walls (see table 4.1 and text) are shown. Arrows indicate the orientation of the applied magnetic field $\boldsymbol{B}$, and the gravity force $\boldsymbol{g}$ (convection).

After the implementation and development of the solver, a series of numerical simulations were conducted to ensure the accuracy of the method. Two flow configurations of a horizontally driven natural convection flow in a rectangular box (see figure 4.1) are considered. Their main parameters are listed in table 4.1. In both configurations, liquid metal is contained within a cuboid box of dimensions $L_x \times L_y \times L_z$. The gravity force is in the negative y-direction. The magnetic field is uniform and directed along the horizontal x-axis. The vertical walls perpendicular to the horizontal z-coordinate are maintained at constant temperatures (a hot wall with $T = 0.5$ and a cold wall with $T = -0.5$). The other walls are thermally insulated. The imposed magnetic field and temperature gradient are, thus, both horizontal and perpendicular to each other. In these cases, the typical length scale of the problem is L_z – horizontal size of the box along the temperature gradient.

The validation Case 1 reproduces the experiment [16, 40]. The configuration is listed as one of the benchmark problems of numerical modeling of liquid-metal MHD flows in [41]. Flow of mercury in a tall box with $L_y = 7.5$ and $L_x = L_z = 1$ is studied. All walls are perfectly electrically insulated. For the verification tests we select flows with $Gr = 3 \times 10^7$ (the Rayleigh number $Ra = PrGr = 7.5 \times 10^5$) and varying strength of the magnetic field corresponding to $0 \leq Ha \leq 796$. Reynolds number (2.31) for this case is approximately $Re = \sqrt{Gr} \approx 5500$, which results in magnetic Reynolds number of $Re_m \approx 8 \times 10^{-4}$ for mercury.

The Case 2 corresponds to the system studied in numerical simulations [18]. Flow of a lithium-lead alloy in a cubic box at $Gr = 3.15 \times 10^6$ ($Ra \approx 10^5$) and $Ha = 100$ is computed. In this case, we test the model's ability to reproduce the effect of finite electrical conductivity of walls in thermal convection flows by varying C_w, with the same values applied at all walls, in the range between 0 and 50. A flow without electromagnetic effects is calculated for comparison.

In both cases and at every combination of parameters, a grid sensitivity study was carried out to determine the size of the grid and the parameters of clustering sufficient for accuracy. In each simulation of the Case 1, the Hartmann layer was resolved by 4 to 5 grid points except for the three highest high Hartmann numbers, where it was resolved by 3 grid points. For the Case 2,

	Case 1			Case 2
L_x	1			1
L_y	7.5			1
L_z	1			1
Gr	3×10^7			3.115×10^6
Pr	0.025			0.0321
C_w	0			$0 - 50$
Ha	0, 85	162, 240	$325 - 796$	100
N_x	64	128	96	64
N_y	480	480	720	64
N_z	64	64	96	64
x	$\gamma = 0.96$	$\gamma = 0.96$	$A = 3.0$	$A = 2.5$
y	$\gamma = 0$	$\gamma = 0$	$\gamma = 0$	$A = 2.5$
z	$\gamma = 0.96$	$\gamma = 0.96$	$\gamma = 0.96$	$A = 2.5$

Table 4.1: Non-dimensional geometry and flow parameters for thermal convection cases. The last three lines show the types and parameters of grid clustering in each direction: blended Chebyshev and uniform grids (3.1) with the weight γ, hyperbolic tangent (3.2) with the clustering coefficient A, and a purely uniform grid $\gamma = 0$.

in all of the simulations, the Hartmann layer was resolved using not less than 5 grid points. The Nusselt number (3.3), and mean kinetic energy (3.4) were used for grid-to-grid comparison. For this study the number of non-dimensional time units which the time averaging is done (t_n) is 100 for unsteady flow regimes except for the case with $Ha = 0$, in which time-averaging was done over 50 non-dimensional time units. A grid was deemed sufficient for accurate simulations if further increase of its size by 50% in each direction or a significant modification of the clustering scheme did not change the first two digits of Nu and E. Table 4.1 lists the parameters defining the grid with sufficient accuracy. The list of the grids used for the grid sensitivity study is reported in table 4.2. Results of the grid sensitivity study for case 1 is reported in table 4.3.

The results of simulations of Case 1 are presented in figures 4.2 and 4.3, and table 4.4. We see the anticipated strong effect of the magnetic field on the flow. As Ha increases, velocity and temperature fields become quasi-two-dimensional. Small-scale turbulent fluctuations are suppressed. Time-averaged total kinetic energy starts to decrease with a sharp change at $Ha = 162$, then after $Ha = 240$ starts to increase with a peak at $Ha = 400$ followed by a decrease at higher Ha (see figure 4.2a and table 4.4).

Grid #	N_x	N_y	N_z	Clustering		
				x	y	z
1	32	480	64	$A = 3.5$	$\gamma = 0$	$\gamma = 0.96$
2	64	480	64	$\gamma = 0$	$\gamma = 0$	$\gamma = 0$
3	64	480	64	$\gamma = 0$	$\gamma = 0$	$\gamma = 0.96$
4	64	480	64	$\gamma = 0.96$	$\gamma = 0$	$\gamma = 0.96$
5	64	480	64	$A = 2.0$	$\gamma = 0$	$\gamma = 0.96$
6	64	480	64	$A = 3.0$	$\gamma = 0$	$\gamma = 0.96$
7	64	480	64	$A = 3.5$	$\gamma = 0$	$\gamma = 0.96$
8	96	480	64	$\gamma = 0$	$\gamma = 0$	$\gamma = 0.96$
9	128	480	64	$\gamma = 0.96$	$\gamma = 0$	$\gamma = 0.96$
10	96	720	64	$\gamma = 0$	$\gamma = 0$	$\gamma = 0$
11	96	720	64	$A = 3.0$	$\gamma = 0$	$\gamma = 0.96$
12	32	32	32	$A = 2.5$	$A = 2.5$	$A = 2.5$
13	48	48	48	$A = 2.5$	$A = 2.5$	$A = 2.5$
14	64	64	64	$A = 2.5$	$A = 2.5$	$A = 2.5$

Table 4.2: Different grid parameters used for grid sensitivity study. The last three columns show the types and parameters of grid clustering in each direction: blended Chebyshev and uniform grids (3.1) with the weight γ, hyperbolic tangent (3.2) with the clustering coefficient A, and a purely uniform grid $\gamma = 0$. Grids 1 - 12 used for the case 1 and grids 12-14 used for case 2

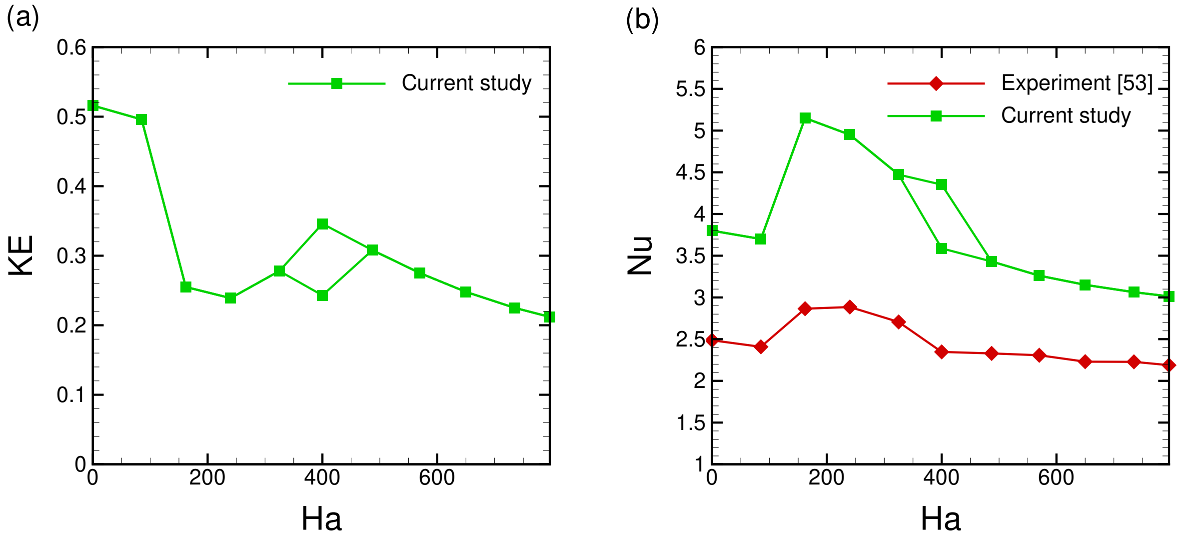

Figure 4.2: Thermal convection flow in a tall box (Case 1). Volume- and time-averaged kinetic energy (3.4) and Nusselt number (3.3) are shown as functions of Ha in (a) and (b), respectively. Experimental data [16] are shown for comparison.

Ha	Grid	Nu (3.3)	$E \times 10$ (3.4)
0	2	3.73	4.74
0	3	3.76	4.97
0	4	3.80	5.16
0	5	3.77	5.11
0	8	3.81	5.10
0	10	3.80	5.14
85	4	3.69	4.96
85	5	3.69	4.96
85	9	3.69	4.92
162	1	5.15	2.57
162	4	5.15	2.55
162	5	5.15	2.56
162	6	5.17	2.56
162	7	5.15	2.57
162	9	5.15	2.55
240	4	4.95	2.34
240	6	4.56	3.03
240	9	4.95	2.40
240	11	4.973	2.40
325	4	4.447	2.66
325	6	4.487	2.73
325	9	4.472	2.78
325	11	4.435	2.78
400	4	4.352	2.34
400	6	3.587	3.45
400	9	3.588	3.46
400	11	4.286	2.43
487	4	3.333	2.98
487	6	3.436	3.11
487	9	3.389	3.10
487	11	3.437	3.10
570	4	3.197	2.59
570	6	3.264	2.74
570	9	3.241	2.73
570	11	3.262	2.75
650	4	3.083	2.29
650	6	3.15	2.46
650	9	3.145	2.43
650	11	3.151	2.48
735	4	3.001	2.09
735	6	3.06	2.23
735	9	3.05	2.20
735	11	3.063	2.25
796	4	2.94	1.95
796	6	3.01	2.10
796	9	3.002	2.10
796	11	3.013	2.12

Table 4.3: Results of the performed grid study for case 1.

Ha	Nu	$E \times 10$
0	3.80	5.16
85	3.69	4.96
162	5.15	2.55
240	4.95	2.39
325	4.44	2.78
400	4.29/3.59	2.43/3.46
487	3.44	3.08
570	3.26	2.75
650	3.15	2.48
735	3.06	2.25
796	3.01	2.12

Table 4.4: Thermal convection flow in a tall box (Case 1). Values of the volume- and time-averaged Nusselt number (3.3) and kinetic energy (3.4) computed at various Ha are shown (see figure 4.2 for a graphical illustration).

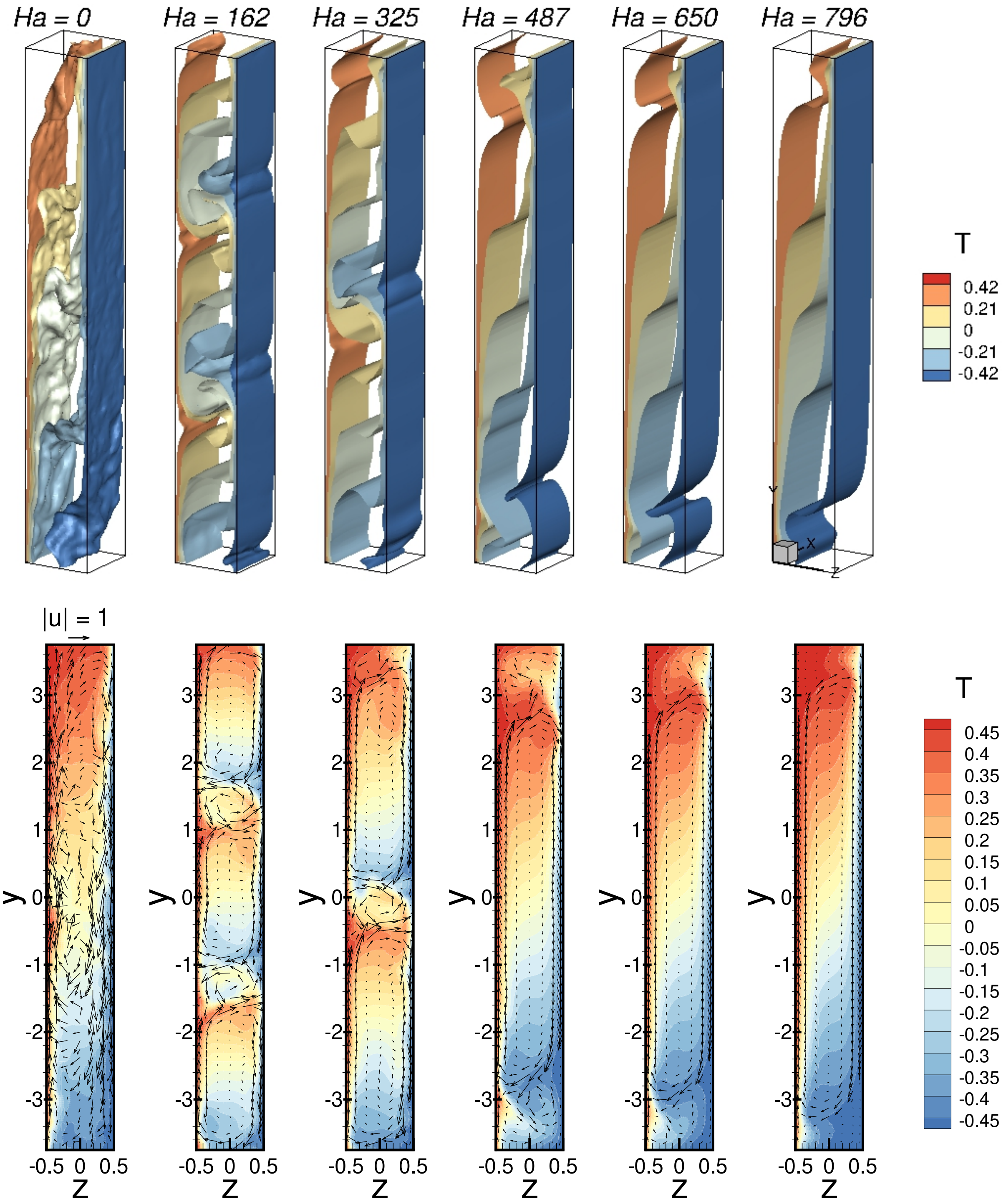

Figure 4.3: Thermal convection flow in a tall box (Case 1). Fully developed flows at various values of *Ha* are shown. Top row: Isosurfaces of temperature field T. Bottom row: Distributions of temperature T and velocity vectors (u_z, u_y) in the midplane perpendicular to the magnetic field. The vectors are drawn every 8 points for $Ha = 0$ and 162 and every 12 points for others.

The magnitude of heat transfer measured by the dimensionless *Nu* also changes substantially with Ha. We see in figure 4.2b and table 4.4 a slight drop as *Ha* changes from 0 to 85 followed by rapid increase with the strongest heat transfer increased at $Ha = 162$, and gradual decay at higher Ha. In a wide range of strong magnetic fields, at $162 \leq Ha \leq 400$, the Nusselt number is higher than in the turbulent flow at zero magnetic field.

The magnetic field also affects the time fluctuations of the Nusselt number $Nu(t)$ and mean kinetic energy $E(t)$. Irregular fluctuations with high amplitude typical for a turbulent flow are found at $Ha = 0$. Their amplitude decreases as *Ha* grows. At $Ha \geq 650$ the fluctuations become sinusoidal, and at $Ha = 798$ the fluctuations disappear demonstrating a steady state of the flow.

Considering the flow structure in figure 4.3, we see that, with the exception of the turbulent flow at $Ha = 0$, the structure is dominated by large-scale quasi-two-dimensional eddies with small eddies between them and in the box corners. The number of such eddies gradually decreases with *Ha*, so that only one major eddy occupying almost the entire box remains at $Ha \geq 487$. It must be stressed that figures 4.2, 4.3 and table 4.4 present fully developed flow states achieved in the course of long flow evolution involving, in some cases, transitions between states with different numbers of large eddies and markedly different values of *Nu* and E. The evolution is assumed completed when no such transitions occur for at least 150 time units.

Peculiar results are obtained at $Ha = 400$. Here, simulations conducted for as much as 600 time units do not allow us to identify an ultimate flow regime. One of the two distinct states, with one or two major eddies (see figure 4.4), appear depending on the grid and initial conditions. Once realized, the state persists for the remaining duration of the simulation run, not less than 200 time units.

The results obtained in our simulations are in good qualitative agreement with the experimental results of [16, 40]. Existence of quasi-two-dimensional flow regimes dominated by a few large eddies was found in the simulations and indirectly suggested by the experimental data. The variation of *Nu* with *Ha* obtained in our computations is consistent with the experiments (see fig-

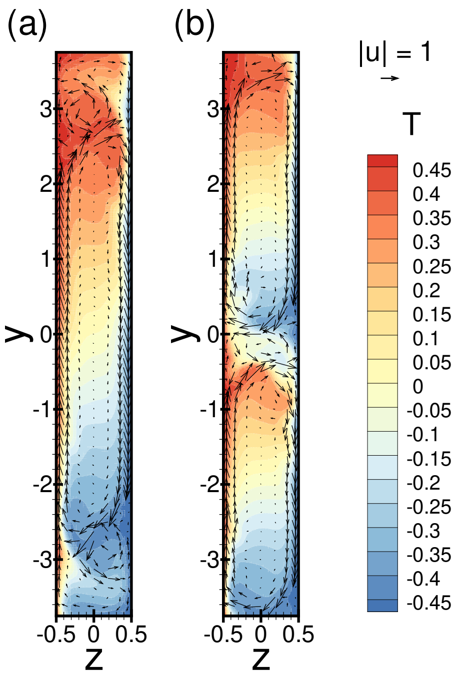

Figure 4.4: Thermal convection flow in a tall box (Case 1). Flow states realizable $Gr = 3 \times 10^7$, $Ha = 400$ are shown. (a) The state with $Nu = 3.59$ and $E = 3.46 \times 10^{-1}$. The vectors are drawn every 8 points. (b) The state with $Nu = 4.29$ and $E = 2.43 \times 10^{-1}$. The vectors are drawn every 12 points.

ure 4.2b).

The peculiar behavior with two realizable states of the flow at $Ha = 400$ was also found in [16, 40]. In the experiment, measurements were done both in the direction of increasing magnetic field intensity as well as decreasing magnetic field intensity. Those measurements show a notable difference, which suggests that the flow in this Ha range is quite sensitive. In the numerical simulations performed in [40], large uncertainty of measured Nu (much larger than at other values of Ha) was found at Ha (ranging between 200 and 300) close to the experiments. The simulations produced two states of the system similar to the states in figure 4.4 and the possibility of a hysteretic transition between them. Transient response of another numerical simulation of the same problem [42], shows the same behavior as well. A more in depth study of this transient behavior would require calculation of the flow evolution over periods of time orders of magnitude longer than the periods covered in this study, which is infeasible in the framework of a fine-resolution numerical model.

C_w	Current Study	[18]
No MHD	3.331	3.267
0	3.245	3.286
0.01	3.046	3.092
0.1	2.277	2.334
1	1.527	1.567
50 (∞)	1.390	1.403

Table 4.5: Results of simulations of thermal convection in a cubic box (Case 2). Values of Nu computed at various values of C_w are shown. Results of simulations [18] are shown for comparison.

At the same time, there is a significant quantitative difference between the predictions of our numerical model and the experimental data of [16, 40]. One can see in figure 4.2b that the computed values of Nu are about 30-40% higher than in the experiments. A similar disagreement was consistently observed between the experiments and the numerical simulations in [40, 41]. As discussed in [11], the discrepancy is common in liquid-metal flows with heat transfer and thermal convection. High thermal conductivity of liquid metals makes it impossible to experimentally reproduce the idealized boundary conditions of constant wall temperature used in simulations. A plausible explanation confirmed by our preliminary solutions of the conjugate heat transfer problem is that in the experiment the temperature perturbations penetrate the walls thus causing reduction of the heat transfer rate. In standard Rayleigh-Bénard convection in closed cylindrical cells at aspect ratio 1, moderate effects of the conjugate heat transfer on the Nusselt number were reported recently [43]. Here, such effects might be even further amplified by the slender geometry.

The results obtained for the case 2 are presented in figure 4.5 and table 4.5. All flows except one at $Ha = 0$ are steady-state. The strong influence of the wall electric conductivity on the flow is evident. Growth of C_w results in suppression of velocity, reduction of Nu and, generally, smaller role played by thermal convection. At the same time, even at $C_w = 50$, which approaches the limit of an electrically perfectly conducting wall, the convection-generated flow is significant, and the temperature distribution is markedly distinct from that of a pure conduction state.

The results are in good qualitative and quantitative agreement with those of numerical

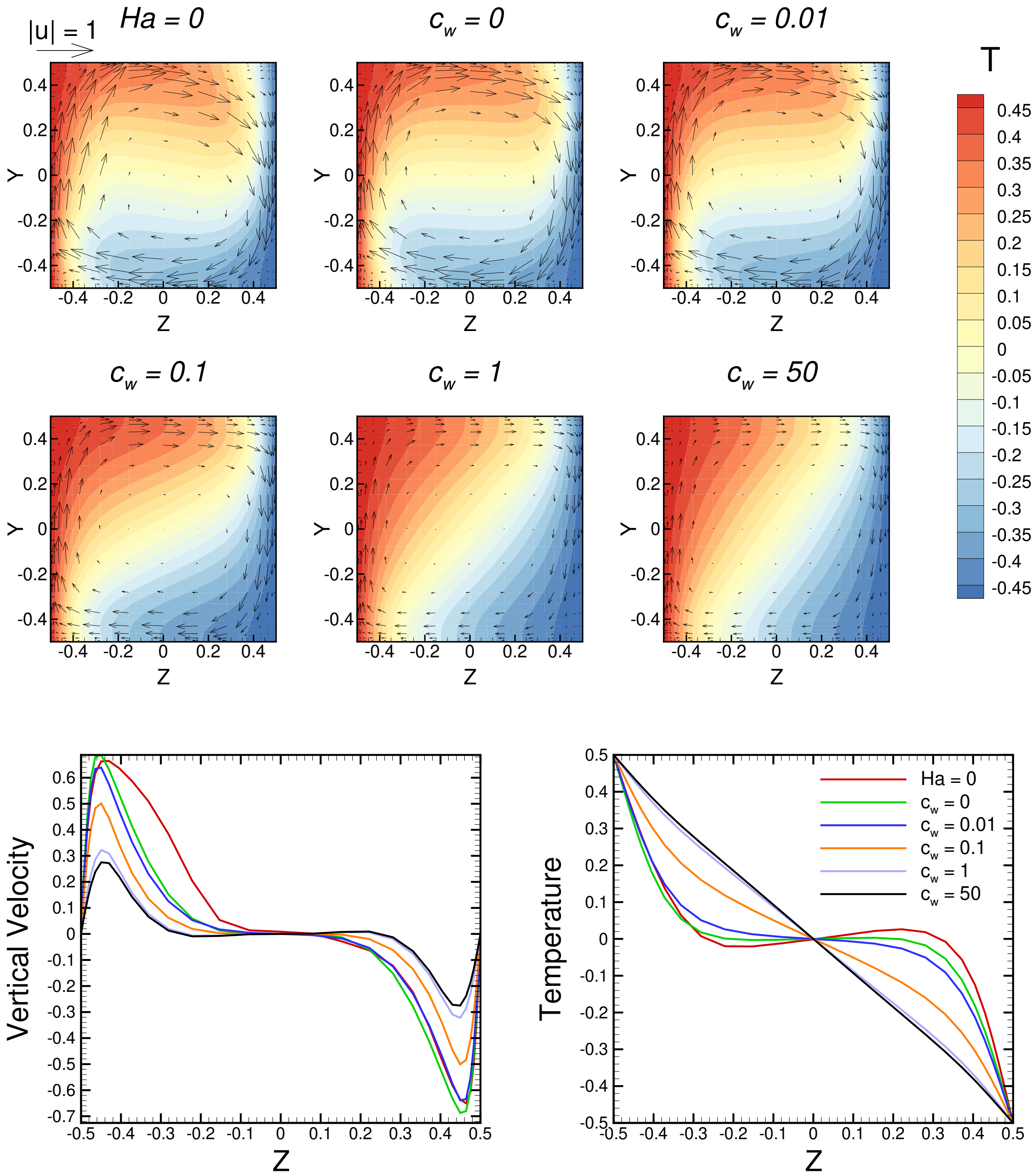

Figure 4.5: Thermal convection flow in a cubic box (Case 2). Simulations results for fully developed flows at $Ra = 10^5$, $Ha = 100$ and various values of C_w are shown. Top two rows: distributions of temperature and velocity vectors in the mid-plane $x = 0$ perpendicular to the magnetic field. The vectors are drawn every 4 points. Bottom row: profiles of u_y and T along the central line perpendicular to the magnetic field $x = 0$, $y = 0$. The non-MHD case $Ha = 0$ is shown for comparison.

simulations [18]. The temperature and velocity distributions in figure 4.5 are similar to those in [18]. The difference in computed values of Nu does not exceed 3.5% (see table 4.5). The quality of the agreement is somewhat surprising, since the simulations of [18] are performed in a way quite different from ours: on a grid of $N_x \times N_y \times N_z = 24 \times 90 \times 90$ finite-volume cells. The low resolution and a uniform grid was used in the magnetic field direction because the Hartmann boundary layers at $x = \pm L_x/2$ were not numerically resolved, but modeled. The good agreement with our results can be partially attributed to relatively low values of Ra and Ha, but also considered as a cross-verification of the two approaches and corresponding methods of numerical simulation.

It is worth mentioning other verification and validation tests demonstrating situations with uniform and non-uniform magnetic fields, duct and isothermal flows were conducted by our colleagues at the TU-Ilmenau in Germany (Dr. Krasnov). The results of those tests can be seen in [25].

4.2 Concluding remarks

A new approach to solution of elliptic problems arising in simulations of liquid-metal MHD flows is presented. The central element of the approach is the TPT method based on tensor-product expansion in two directions and the Thomas algorithm solution in the third direction. Its main novelties are that *(i)* the TPT method is combined with the conservative discretization of proven accuracy and efficiency [30] and *(ii)* the method is extended to permit solution of electric potential problems in domains with thin walls of finite electric conductivity.

Extensive verification and validation tests have demonstrated accuracy of the method in applications to flows of various types: steady-state and unsteady, and with walls of various electric conductivities. The conservative discretization, ability to handle arbitrarily non-uniform grids, and use of efficient tools of numerical algebra make the approach especially effective in simulations of flows with pronounced boundary layer behavior, in particular liquid-metal MHD flows at high Hartmann and Stuart numbers.

CHAPTER 5

Effect of Walls of Finite Electrical Conductivity

This chapter is based on the results published in [44]. Using the solver verified and tested in the previous chapter, an investigation of the effect of the wall conductivity and the configuration of conductive walls based on the case 1 in chapter 4 was carried out. The case 1 is selected for two reasons; availability of experimental data [16, 40] and relevance of the geometry to the concept of separately cooled liquid metal blankets for future nuclear fusion reactors [7, 13]. The configuration was proposed as a benchmark for numerical models of magnetoconvection flows [41]. It must be stressed that the flow studied in our work does not correspond to any specific blanket design.

The effect of wall conductivity on the flow is determined not just by the value of the wall material's conductivity but by the ratio between the total conductances of the wall and the fluid (wall conductance ratio (2.33)). As discussed earlier high electrical conductivity of liquid metals as well as small thickness of walls leads to low values of this ratio, even when the walls are made of well-conducting materials. This consideration has directed many previous studies to the idealized model in which walls are assumed to be perfectly electrically insulating.

This study aims to investigate the effect of wall conductance ratio on the properties of magnetoconvection flow within a specific geometry - a tall cuboid enclosure subjected to heating and cooling at opposite vertical sides in the presence of an external transverse magnetic field parallel to the heated/cooled walls (see Fig. 5.1). This is an example of a system, in which the three major direction – those of gravity, temperature gradient and magnetic field – are perpendicular to each other. The configuration was studied before using linearized two-dimensional model

Property	$L_x \times L_y \times L_z$	Ra	Pr	Ha
Value	$1 \times 1 \times 7.5$	7.5×10^5	0.025	0 – 796

Table 5.1: Non-dimensional geometry and parameters of the studied flow, (see text for a detailed discussion and definition of Ra, Pr, and Ha in (2.30)).

[13, 14], experiment [16, 40], and numerical simulations [16, 40, 45, 46]. Unique features of the flow, such as thin quasi-two-dimensional jets near the hot and cold walls, were found.

The only previous attempt of analysis of this system based on high-resolution numerical simulations was [45]. The authors used OpenFOAM to study the effect of wall conductivity (with all walls having the same wall conductance ratio) and the direction of magnetic field at $Ra = 10^5$. The study was limited to one low value of the Hartmann number $Ha = 100$, thus missing the most interesting features observed at moderate and high Ha.

Two different configurations of electrical conducting walls are considered. In the first, all the walls have finite electric conductivity with the same conductance ratio. In the second, only walls with constant temperatures are considered to have finite electric conductivity with the same conductance ratio, while other walls are perfectly electrically insulating ($C_w = 0$). Four different wall conductance ratios are considered, $C_w = 0.01, 0.1, 1$ and 50. The value of 50 is chosen as a representative of cases with almost perfectly electrically conducting walls.

The flow domain is similar to the domain introduced in the chapter 4, except that in this study the directions of (x, y, z) axes is changed. The dimensions of the box and physical properties of the flow are listed in table 4.1. An illustration of the flow domain is given in figure 5.1. In this problem, the typical length scale is $L = L_x$.

Considering the results of the grid-sensitivity study explained in chapter 4, a similar grid setup regardless of the wall electrical conductance value is used. In the flows with $C_w > 0$, the boundary layers are not the only available current paths, so accurate numerical resolution of them becomes an even less stringent requirement. Based on this argument, the grid parameters shown in Table 5.2 are used in the simulations irrespective of the value of the wall conductance ratio C_w. Due to strong suppression of velocity gradients parallel to magnetic field direction at high Ha, the

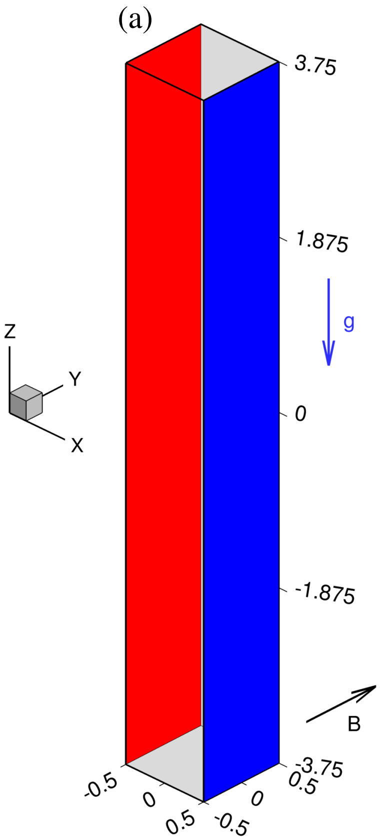

Figure 5.1: Schematic of the flow domain. *(a)*, Geometry - a cuboid box with two side walls maintained at constant temperatures: red (hot wall) and blue (cold wall). The other four walls are perfectly thermally insulating. The directions of the applied magnetic field $\boldsymbol{B}$ and the gravity acceleration $\boldsymbol{g}$ are indicated. *(b)*, Lines, along which velocity, temperature, and induced current profiles are recorded in simulations. Each line passes through the point $(x, y, z) = (-0.47, 0, 0)$ and is parallel to the x, y or z direction. (c) Cross-section planes, in which velocity, temperature, and induced current distributions are recorded in simulations. Each surface contains the point $(x, y, z) = (0, 0, 0)$ and has a normal parallel to the x, y or z direction.

Ha	0, 85	162, 240	325 – 796
N_x	64	64	96
N_y	64	128	96
N_z	480	480	720
x	$\gamma = 0.96$	$\gamma = 0.96$	$\gamma = 0.96$
y	$\gamma = 0.96$	$\gamma = 0.96$	$A = 3.0$
z	$\gamma = 0$	$\gamma = 0$	$\gamma = 0$
Δt	1×10^{-3}	5×10^{-4}	1.6×10^{-4}

Table 5.2: Computational grid parameters. The last three lines show the types and parameters of grid clustering in each direction: blended Chebyshev and uniform grids (3.1) with the weight γ, hyperbolic tangent (3.2) with the clustering coefficient A, and a purely uniform grid $\gamma = 0$.

$tanh$ grid transformation method (3.2) is used in y-direction (parallel to magnetic field) for cases with $Ha \geq 325$, which allows for more grid points within the Hartmann boundary layers, while keeps the number of grid points manageable.

In this study each simulation runs for either 200 or 400 non-dimensional time units based on the volume averaged signals recorded over time which are explained later in text. All of the results presented in this section are for the fully-developed flow. The flow is considered to be in a fully developed state when $Nu(t)$ (3.3) and $E(t)$ (3.4) are fluctuating around a steady mean. Visualizations of the velocity and temperature distributions were also used to confirm that the number, location, and general shape of large-scale circulation eddies dominating the flow structure remain unchanged during this period. The length of the runs assures that a long (never less than 100 non-dimensional time units) evolution of a fully developed flow is calculated. Time-averaged flow properties, such as the mean values of the Nusselt number and kinetic energy are computed during the last 100 time units of this period. As illustrated by the curves of computed $Nu(t)$ and $E(t)$ presented below, this duration is sufficient to minimize the effect of individual velocity fluctuations on the evaluation of time-averaged properties.

It is worth noting, while no systematic analysis of the effect of the initial conditions was carried out, tests were conducted for the flow with $Ha = 650$ and all walls electrically conducting. First, the evolution of the flow with $C_w = 50$ was computed starting from the initial conditions in the form of the two previously computed fully developed flow fields: one with $Ha = 0$ and one with $Ha = 650$ and $C_w = 0$. In the second test, the flows with $C_w = 0.1$ and $C_w = 1$ were computed starting from the fully developed flow at $Ha = 0$ as an initial condition. It was found in both tests that the change of the initial state did not affect the final fully developed state of the flow.

Since two different sets of boundary conditions are considered, the results are discussed separately. First the results for the configuration in which all walls have the same electrically conductance ratio C_w is discussed. After that the results for the case in which only hot and cold walls are considered to be electrically conducting and have the same electrical conductance ratio C_w

are presented. Hereafter these setups are called configurations A and B, respectively. Due to the fact that the results of the simulations in which all of the walls are electrically insulating is repeated in both sections, those results are only discussed in the beginning of the section 5.1, and this discussion is omitted in section 5.2.

5.1 Configuration A: all walls have the same electric conductivity

Figure 5.2 shows the time evolution Nu and E during the entire simulations for two typical cases, one with moderately high $Ha = 325$ and the other with high $Ha = 650$. The results obtained for the pure convection flow at $Ha = 0$ are included for comparison. As it is mentioned earlier, each simulation is conducted over either 200 or 400 time units. Simulations first run for 200 time units and, if random fluctuations are observed such that it justifies the need for further simulations, simulation is continued for another 200 time units, totalling to 400 non-dimensional time units. As it is shown in the figure 5.2, calculating the time averaged values over the last 100 time units, seems sufficient.

The time averaged values Nu and E obtained for the configuration A for all the explored values of Ha and C_w are reported in tables 5.3 and 5.4 and shown in Fig. 5.3. The discussion will also use the distributions of the time-averaged flow fields within the flow domain shown in Figs. 5.4-5.9.

5.1.1 All walls are perfectly electrically insulating

We start with a brief discussion of the behavior in the case of electrically insulating walls, the results for which are obtained in chapter 4. At first, we see in tables 5.3 and 5.4 and figure 5.3 that increasing magnetic field causes a slight decrease in heat transfer followed by a jump to higher values of Nu at $Ha = 162$ and then a monotonic decrease. The mean kinetic energy E also decreases as magnetic field intensity increases, up to $Ha = 162$. At higher values of Ha, the

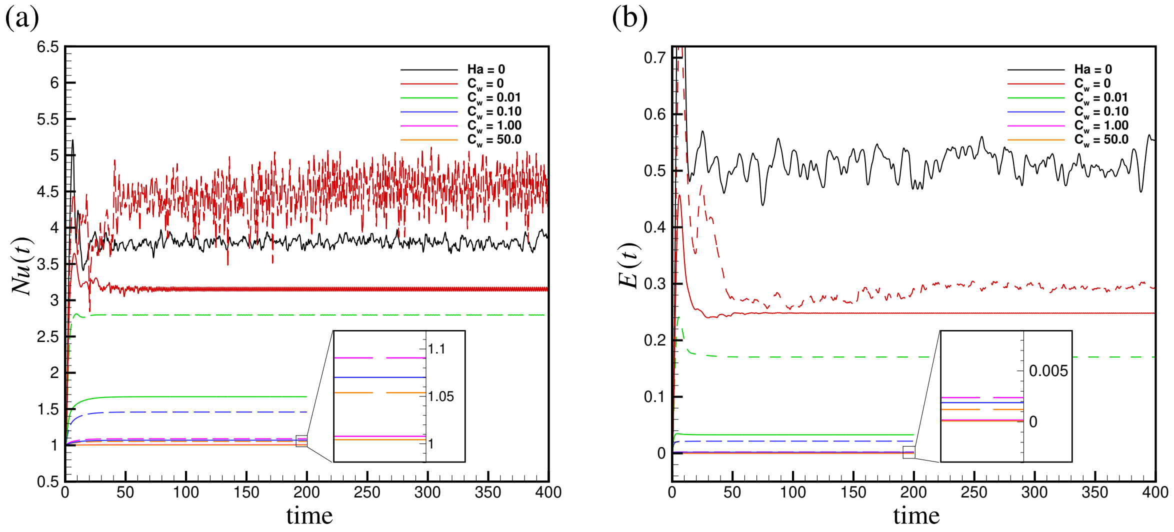

Figure 5.2: *(a)* $Nu(t)$ and *(b)* $E(t)$ (see (3.3) and (3.4)) for $Ha = 325$ (dashed line) and $Ha = 650$ (solid line) for the configuration A of the wall conductivity conditions. Black solid line represents the case $Ha = 0$. In this and all the following figures, the results are obtained for $Ra = 7.5 \times 10^5$ and $Pr = 0.025$.

kinetic energy remains high indicating that the magnetic field does not prevent strong large scale circulation in the flow with $C_w = 0$.

		C_w				
		0	0.01	0.1	1	50
	0			$\overline{3.80}$		
	85	$\overline{3.69}$	$\overline{3.63}$	$\overline{3.36}$	$\overline{2.59}$	$\overline{2.28}$
	162	$\overline{5.15}$	$\overline{3.62}$	$\overline{2.54}$	1.55	1.37
	240	$\overline{4.95}$	$\overline{3.15}$	1.86	1.22	1.14
Ha	325	$\overline{4.47}$	$\overline{2.80}$	1.46	1.09	1.05
	400	$\overline{4.35}$	2.46	1.28	1.05	1.03
	487	$\overline{3.43}$	2.11	1.17	1.02	1.01
	570	$\overline{3.26}$	1.85	1.11	1.01	1.01
	650	$\overline{3.15}$	1.67	1.07	1.02	1.00
	735	$\overline{3.06}$	1.52	1.04	1.01	1.00
	796	3.01	1.45	1.04	1.00	1.00

Table 5.3: Time averaged values of Nu (3.3) computed for the configuration A (all walls have the same conductance ratio C_w). Values marked with an overline indicate cases in which $Nu(t)$ fluctuates significantly in a fully developed flow. In other cases, the signal is steady-state after an initial transient.

		C_w				
		0	0.01	0.1	1	50
	0			$\overline{5.16 \times 10^{-1}}$		
	85	$\overline{4.96 \times 10^{-1}}$	$\overline{4.38 \times 10^{-1}}$	$\overline{3.13 \times 10^{-1}}$	$\overline{1.62 \times 10^{-1}}$	$\overline{1.16 \times 10^{-1}}$
	162	$\overline{2.55 \times 10^{-1}}$	$\overline{3.33 \times 10^{-1}}$	$\overline{1.48 \times 10^{-1}}$	3.00×10^{-2}	1.60×10^{-2}
	240	$\overline{2.39 \times 10^{-1}}$	$\overline{2.53 \times 10^{-1}}$	5.68×10^{-2}	7.32×10^{-3}	3.79×10^{-3}
Ha	325	$\overline{2.78 \times 10^{-1}}$	$\overline{1.70 \times 10^{-1}}$	2.15×10^{-2}	2.38×10^{-3}	1.21×10^{-3}
	400	$\overline{2.43 \times 10^{-1}}$	1.14×10^{-1}	1.05×10^{-2}	1.10×10^{-3}	5.57×10^{-4}
	487	$\overline{3.08 \times 10^{-1}}$	7.30×10^{-2}	5.28×10^{-3}	5.26×10^{-4}	2.66×10^{-4}
	570	$\overline{2.75 \times 10^{-1}}$	4.81×10^{-2}	3.02×10^{-3}	2.93×10^{-4}	1.48×10^{-4}
	650	$\overline{2.48 \times 10^{-1}}$	3.28×10^{-2}	1.89×10^{-3}	1.80×10^{-4}	9.08×10^{-5}
	735	$\overline{2.25 \times 10^{-1}}$	2.24×10^{-2}	1.22×10^{-3}	1.14×10^{-4}	5.76×10^{-5}
	796	2.12×10^{-1}	1.74×10^{-2}	9.16×10^{-4}	8.52×10^{-5}	4.21×10^{-5}

Table 5.4: Time averaged values of E (3.4) computed for the configuration A (all walls have the same conductance ratio C_w). Values marked with an overline indicate cases in which $E(t)$ fluctuates significantly in a fully developed flow. In other cases, the signal is steady-state after an initial transient.

The observed variation of Nu and E with Ha may appear to contradict to the known ability of an imposed magnetic field to suppress fluctuations of velocity. A monotonic decrease of both Nu and E may appear more natural. An explanation of the effect is based on the role played by large-scale circulation in the flow field and heat transfer. As demonstrated in Figs. 5.4, 5.5, 5.6 and 5.7, the flow is dominated by planar jets, an ascending one near the hot wall and a descending one near the cold wall. This is expected behavior for a natural convective flow in a box with hot and cold walls on the side. As these jets, ascend and descend near the walls, they form large scale eddies in the x-z-plane.

The large-scale circulation may consist of just one eddy, with secondary smaller eddies in the corners (see Fig. 5.4b), or several large eddies. The number of these structures exist in the flow impacts the effectiveness of heat transfer as well as kinetic energy of the flow. The presence of multiple eddies increases the heat transfer rate via two mechanisms. One is the direct transport of heat by horizontal streams separating the eddies. The second is that eddies not extending through the entire height of the box disrupt the thermal boundary layers and remove hot fluid

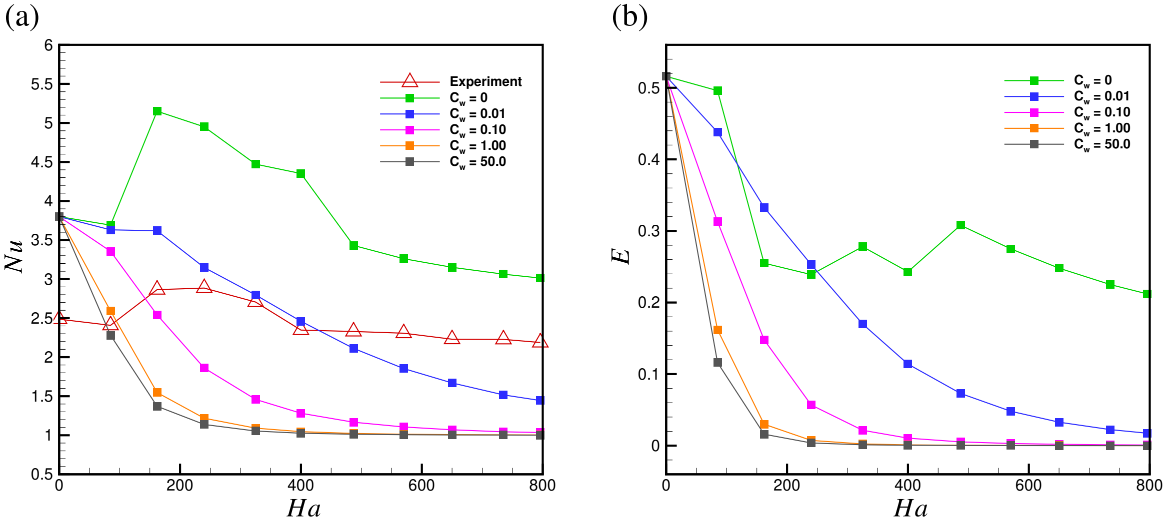

Figure 5.3: Time averaged values of *Nu* and *E* for configuration A (all walls have the same conductance ratio C_w). Data for the case of all walls electrically insulating and the experimental data [16] (available only for *Nu*) are shown for comparison.

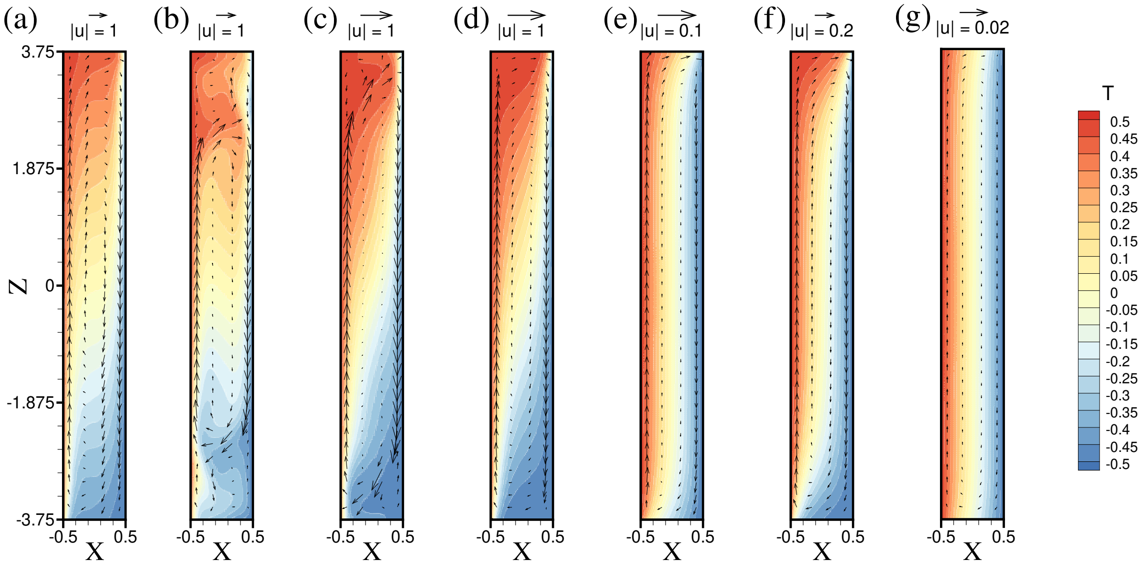

Figure 5.4: Time-averaged distributions of *T* and a projection of the velocity on the vertical mid-plane cross-sections $y = 0$ perpendicular to the magnetic field direction (see Fig. 5.1c) for configuration A. Results for the flows with $Ha = 0$ *(a)*, $Ha = 85$, $C_w = 0.01$ *(b)*, $Ha = 85$, $C_w = 1.0$ *(c)*, $Ha = 400$, $C_w = 0.01$ *(d)*, $Ha = 400$, $C_w = 1.0$ *(e)*, $Ha = 796$, $C_w = 0.01$ *(f)* and $Ha = 796$, $C_w = 1.0$ *(g)* are shown.

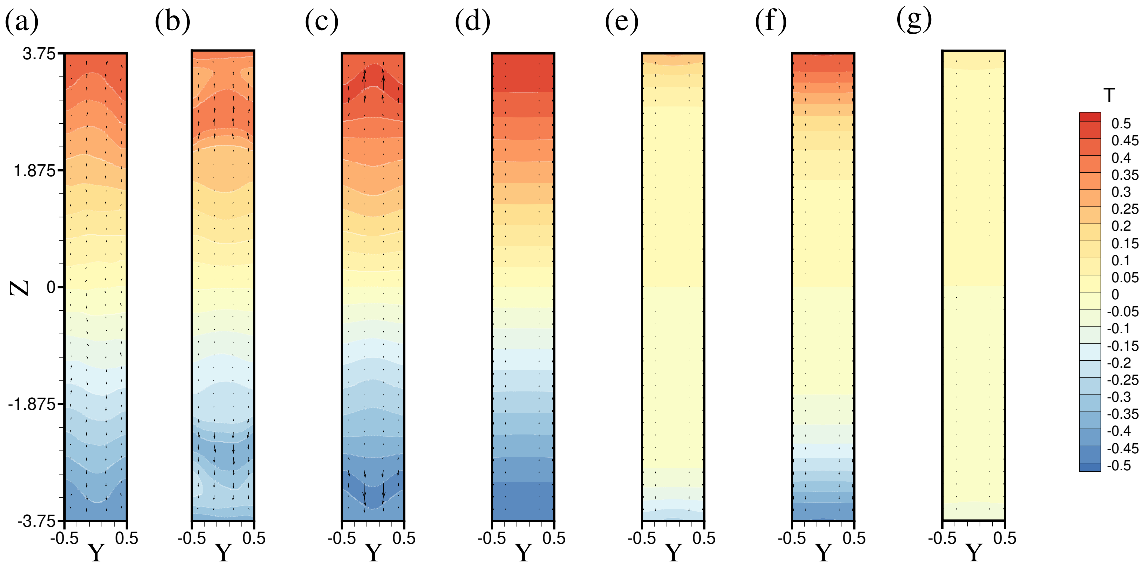

Figure 5.5: Time-averaged distributions of T and a projection of the velocity on the vertical mid-plane cross-section $x = 0$ parallel to the magnetic field direction (see Fig. 5.1c) for configuration A. Results for the flows with $Ha = 0$ *(a)*, $Ha = 85$, $C_w = 0.01$ *(b)*, $Ha = 85$, $C_w = 1.0$ *(c)*, $Ha = 400$, $C_w = 0.01$ *(d)*, $Ha = 400$, $C_w = 1.0$ *(e)*, $Ha = 796$, $C_w = 0.01$ *(f)* and $Ha = 796$, $C_w = 1.0$ *(g)* are shown.

from the hot wall and cold fluid from the cold wall early, effectively reducing the average thickness of the boundary layer and, thus, its thermal resistance. Another effect of the formation of multiple eddies is that it limits the range, where the vertical jets near the walls can accelerate, thus resulting in lower jet velocity and lower mean kinetic energy.

It will be shown later that if the number of circulations remains constant, the maximum speed of jets near the wall in addition to the jet width can determine how high the heat transfer rate will be. In the absence of the magnetic field, as it is shown in figures 5.4.a and 5.12.a, only one big circulation forms in the mean flow which fills the entire flow domain. Introducing magnetic field to the domain cause changes in the resulting flow both directly and indirectly.

The direct effect of an imposed magnetic field on the flow is, typically, two-fold. Firstly, the flow becomes anisotropic and, at high Ha, quasi-two-dimensional (see Fig. 5.7a). Another effect is the suppression of velocity fluctuations leading to stabilization of the near-wall jets and large-scale circulation eddies. Indirectly, the imposed magnetic field also affects the pattern of the large-scale circulation, which explains the change of values of Nu and E visible in Tables 5.3, 5.4

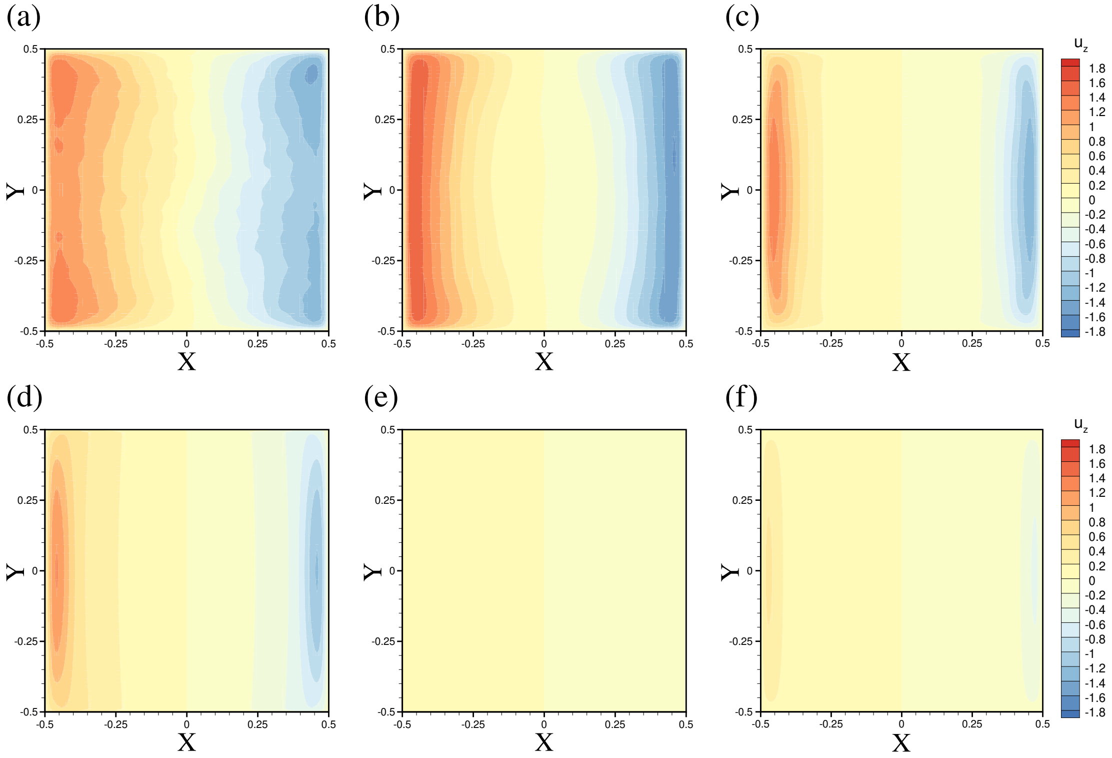

Figure 5.6: Time-averaged distributions of vertical velocity u_z on the horizontal mid-plane cross-section $z = 0$ (see Fig. 5.1c) for configuration A. Results for the flows with $Ha = 0$ *(a)*, $Ha = 85$, $C_w = 0.01$ *(b)*, $Ha = 85$, $C_w = 1.0$ *(c)*, $Ha = 400$, $C_w = 0.01$ *(d)*, $Ha = 400$, $C_w = 1.0$ *(e)* and $Ha = 796$, $C_w = 0.01$ *(f)* are shown.

and Fig. 5.3. Magnetic field suppresses turbulent fluctuations and makes the flow Q2D. However, large scale Q2D vortices are not suppressed. They are also stabilized so, they can be strong even at $Ha \ll 1$. The change of the pattern is presented in figure 4.3 and further illustrated by the vertical profiles of velocity and temperature in Figs. 5.8a and 5.9a. The mean flow has one large-scale circulation vortex at $Ha = 0$ and $Ha = 85$. Three circulation vortices appear at $Ha = 162$, which causes strong increase of Nu and drop of E. Two circulation vortices are found at $Ha = 325$. Circulation patterns with just one large eddy and gradually decreasing strength of the mean flow are found at $Ha \geq 487$.

As demonstrated in chapter 4 and [25] the flow regime when $Ha = 400$ is sensitive to computational grid. In this study only the finer grid as reported in table 5.2 is considered and values related to this computational grid is reported in tables 5.3 and 5.4 and figure 5.3. As a result of this decision, such behavior is not observed. The flow also shows a transient behavior in a way that large circulations can form and merge as the flow develops. The same situation applies to the results reported in the section 5.2.

Increasing the intensity of magnetic field, regardless of wall electrical conductivity, results in a more restricted flow, the jet velocities decreases, as demonstrated in figure 5.7, and as a result of that, the heat transfer rate and Nu decreases. Another outcome of lower jet velocities is that the flow does not separate from the wall and thus results in disappearance of small vortices that appear at the corners of the box.

5.1.2 All walls are electrically conducting

Upon introducing electrical conductivity of the walls, flow and its fluctuations are drastically suppressed. The suppression of the flow, as it can be seen in the vertical velocity profiles shown in figures 5.7 and 5.8, is amplified by increasing the electrical conductivity of the walls. As for the non-time-averaged flow and the flow fluctuations around the mean, it is observed that introducing wall conductivity even for the lowest value $C_w = 0.01$ removes all flow fluctuations as the Ha goes beyond 400. For the lower values of Ha, except $Ha = 85$, there is a value of C_w, such

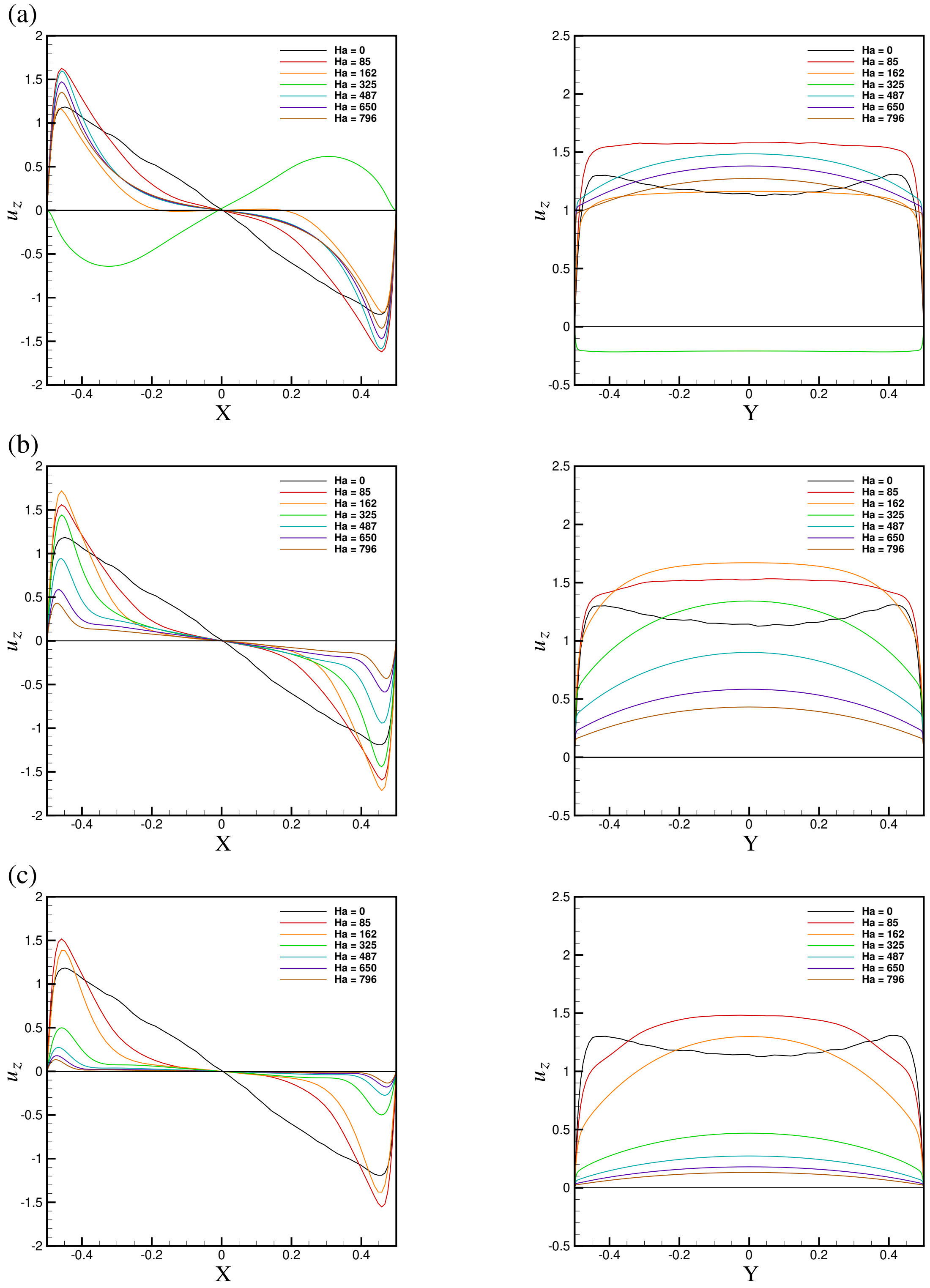

Figure 5.7: Timed-averaged profiles of vertical velocity along the lines $y = 0$, $z = 0$ (left) and $x = -0.47$, $z = 0$ (right) shown in Fig. 5.1b. Results obtained for $C_w = 0$ *(a)* and the configuration A with $C_w = 0.01$ *(b)* and $C_w = 0.1$ *(c)* are shown for various Ha.

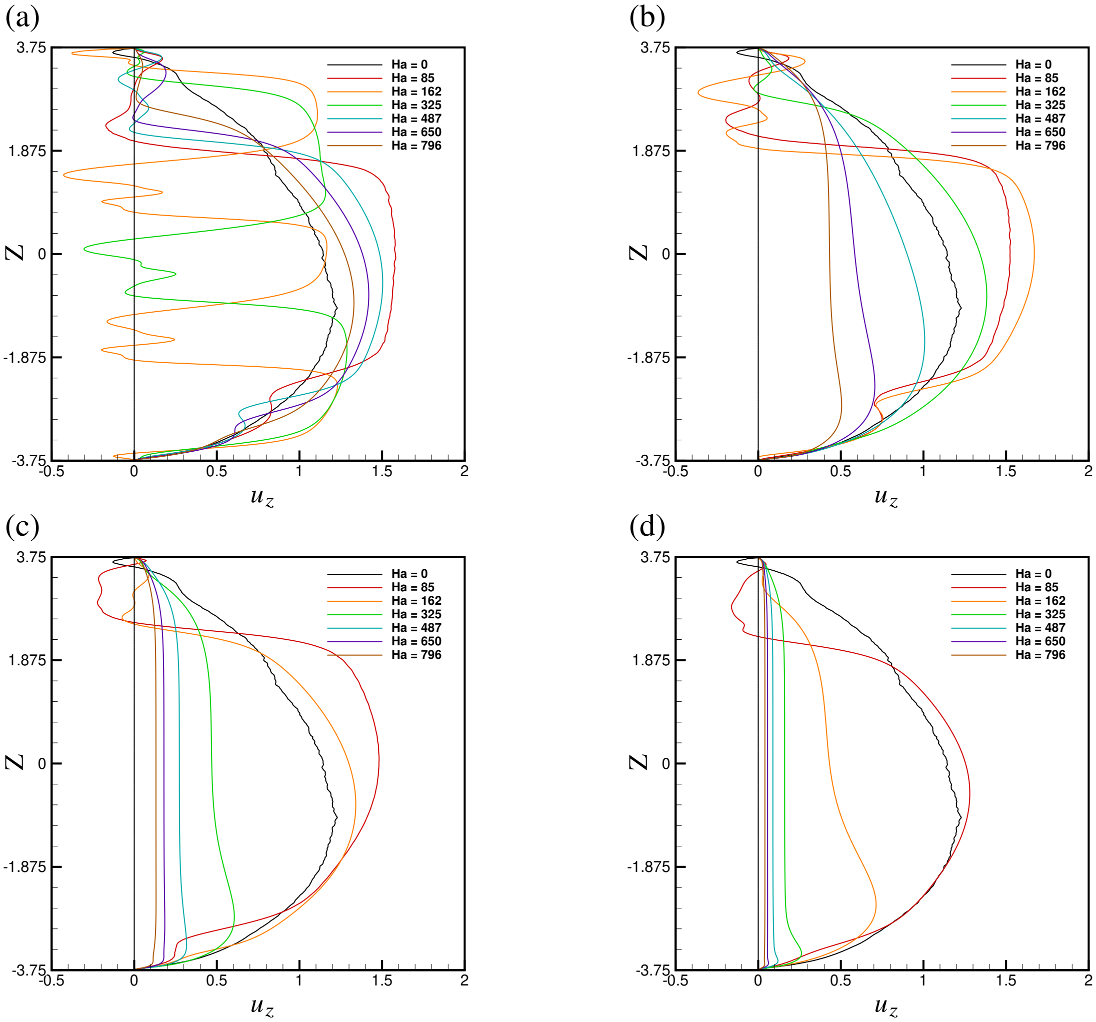

Figure 5.8: Timed-averaged profiles of vertical velocity along the line $x = -0.47$, $y = 0$ shown in Fig. 5.1b. Results obtained for $C_w = 0$ *(a)* and the configuration A with $C_w = 0.01$ *(b)* $C_w = 0.1$ *(c)*, and $C_w = 1.0$ *(d)* are shown for various Ha. A black dotted line indicates $u_z = 0$.

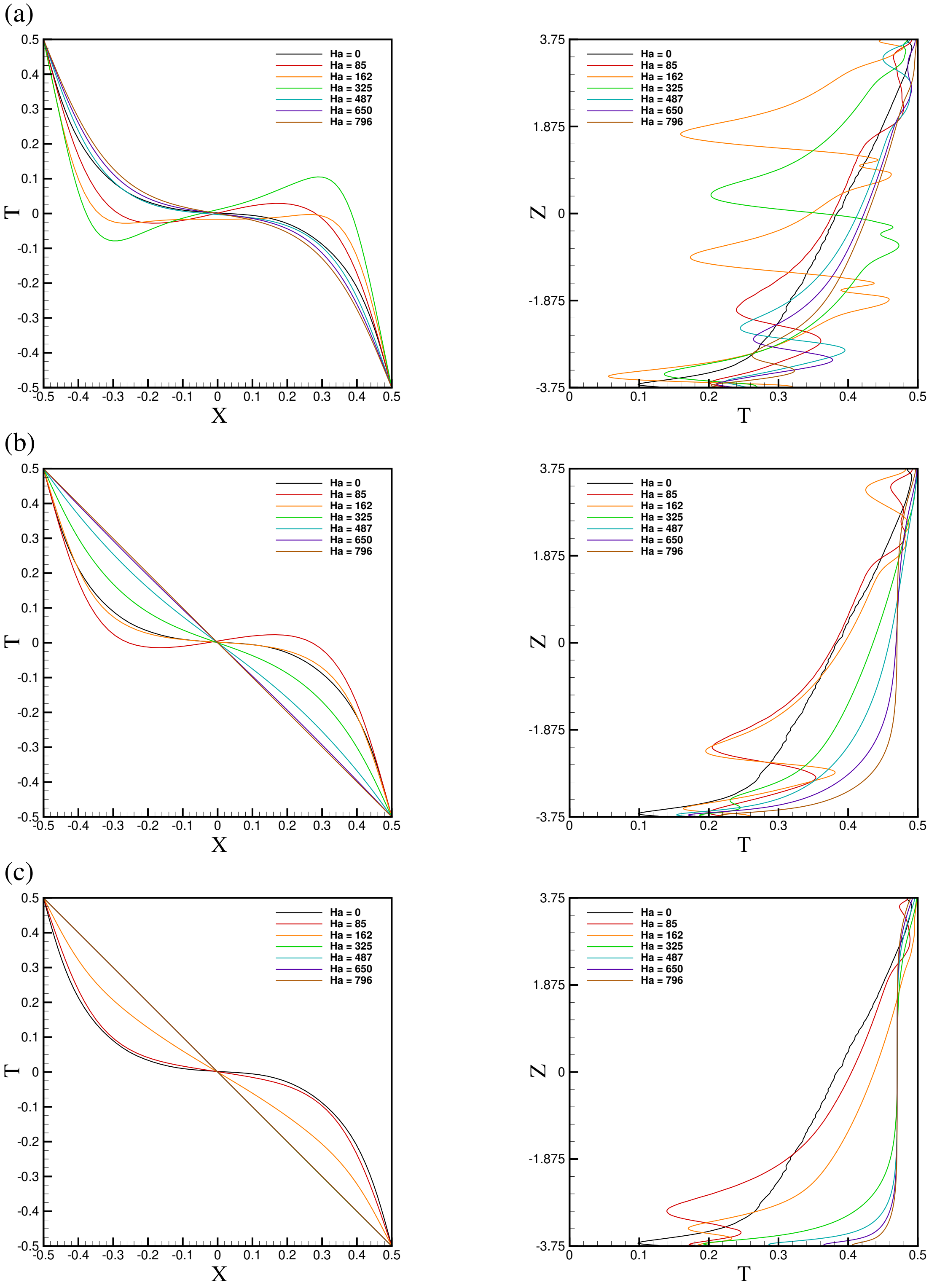

Figure 5.9: Timed-averaged profiles of temperature along the lines $y = 0$, $z = 0$ (left) and $x = -0.47$, $y = 0$ (right) shown in Fig. 5.1b. Results obtained for $C_w = 0$ *(a)* and the configuration A with $C_w = 0.01$ *(b)* and $C_w = 0.1$ *(c)* are shown for various Ha.

that a higher value of wall electrical conductivity has a same effect. For the case with $Ha = 85$, it is observed that increasing wall conductivity lowers the amplitude of fluctuations. The cases that demonstrate no flow fluctuations, reach to their steady state within the first 50 time units, but in order to rule out any further development of the flow, the simulations continued to reach 200 time units.

Looking at the time averaged flow, for all values of Ha number if $C_w > 0$, only one large scale vortex is formed in the domain (see Fig. 5.4 and Fig. 5.8 for an illustration). Since the jump in heat transfer rate observed when all the walls are electrically insulated is mainly due to formation of more than one large scale vortices, a same jump in Nu is not seen for the cases with $C_w > 0$. Both Nu and E decrease monotonically with increasing Ha or C_w. At $C_w \geq 0.1$ and large Ha, $E \sim 10^{-5} - 10^{-3}$ and Nu is close to the pure conduction value 1.0 (see Tables 5.3 and 5.4 and Fig. 5.3). This effect is further illustrated by the velocity and temperature profiles in Figs. 5.7-5.9. We see in Figs. 5.7 and 5.8 that velocity of near-wall jets decreases as either Ha or C_w increases. The effect is considerably higher at higher values of Ha. For example, comparing the results for when $C_w = 0$ and $C_w = 0.01$, the maximum jet velocity for $Ha = 85$ experience less than 10% speed reduction, however for the $Ha = 487$ and $Ha = 796$, the reduction in speed is about 50% and 70% respectively. Weakened convective heat transfer results in temperature distributions approaching pure conduction distributions with exception of the regions near the top and bottom walls, where a horizontal flow persists (see Figs. 5.4 and 5.9).

The apparent inconsistency between the profile of vertical velocity in the case of $Ha = 325$ and $C_w = 0$ and the other profiles (see Figs. 5.7a and 5.15a) is a result of a peculiar flow regime at these parameters. One can see in the first column of Table 5.7 and Figs. 5.8a and 5.16a that in this case the flow consists of two major eddies of the same circulation (upward flow near the hot wall). A similar flow is shown in Fig. 5.12e for the case with $Ha = 400$ and $C_w = 1.0$. Such a flow structure means that there must be a smaller reversed circulation eddy sandwiched between the two large eddies. Since the velocity profiles in Figs. 5.7a and 5.15a are drawn along the line in the middle of domain (see Fig. 5.1b), the vertical velocity profiles corresponding to the smaller eddy and, therefore, having the opposite direction is captured.

It should be noted that in this comparison, it is important to make sure the number large vortices are the same, otherwise the jets will not have the same space to develop and it will result in different jet velocities. It is important to mention, that the maximum vertical velocities found from 5.7 , do not represent the maximum jet velocities for each case, as it is measured in the middle of the box, and it can be seen 5.7 and 5.8 that the location of the maximum jet velocity can vary in both y and z directions.

One apparent exception from the just described transformation is the case of the flows with $C_w = 0.01$ and Ha increasing from 85 to 162. Fig. 5.8b shows increase of the maximum vertical velocity in the core of the jet. Analysis of three-dimensional velocity distributions, however, demonstrates the accompanying decrease of the jet's width (see Fig. 5.7b), so the values of Nu are nearly the same at $Ha = 85$ and 162, and E is substantially smaller at $Ha = 162$ (see Tables 5.3 and 5.4).

An important observation can be made based on the velocity distributions shown in Figs. 5.5 and 5.6 and the velocity profiles in the right-hand side columns of Fig. 5.7b,c. The assumption of quasi-two-dimensionality often used in the analysis of high-Ha MHD flows is generally inaccurate for the flows considered here. One sees in Fig. 5.7c, that even in the case with the highest $Ha = 796$ the velocity variation in the core flow along the magnetic field line (the y-direction) is non-negligible. Similar behavior is demonstrated by the profiles of the mean velocity at all $C_w > 0$. The curvature is higher at moderately high values of Ha, such as $Ha = 400$ or 325 (see Fig. 5.7). The phenomenon can be attributed to the shape of the zones of strong flow in the upward and downward jets. The horizontal cross-section has the much larger y-dimension in the direction of the magnetic field than the x-dimension. In that sense, the jet flow is similar to flows within narrow ducts with magnetic fields in the transverse direction parallel to the longer side. Quasi-two-dimensionality is not achieved in such flows even at high Ha (see, e.g., Ref. [47] for an illustration).

On the other hand temperature profiles along Y axis does not show such behavior, and in most cases especially for high Ha and high C_w temperature variations outside the Hartmann boundary layer are very small. Such behavior is expected due to the nature of temperature boundary condition and low flow velocities which results in a temperature profile similar to fully conduction temperature distribution. Such behavior stresses the need to measure velocity distributions in addition to temperature along the magnetic field direction as well as other directions.

Looking at the vertical velocity profiles along with the temperature profiles, it can be seen that, in cases with lower jet velocities which do not separate from the walls, as jets ascend and their temperature increases, their temperature reaches the temperature of the fully conductive temperature profile (0.47 for the plots in figure 5.9), they rise with a constant speed, until they reach to area near box ceiling, where they have no more room to travel and start to decelerate.

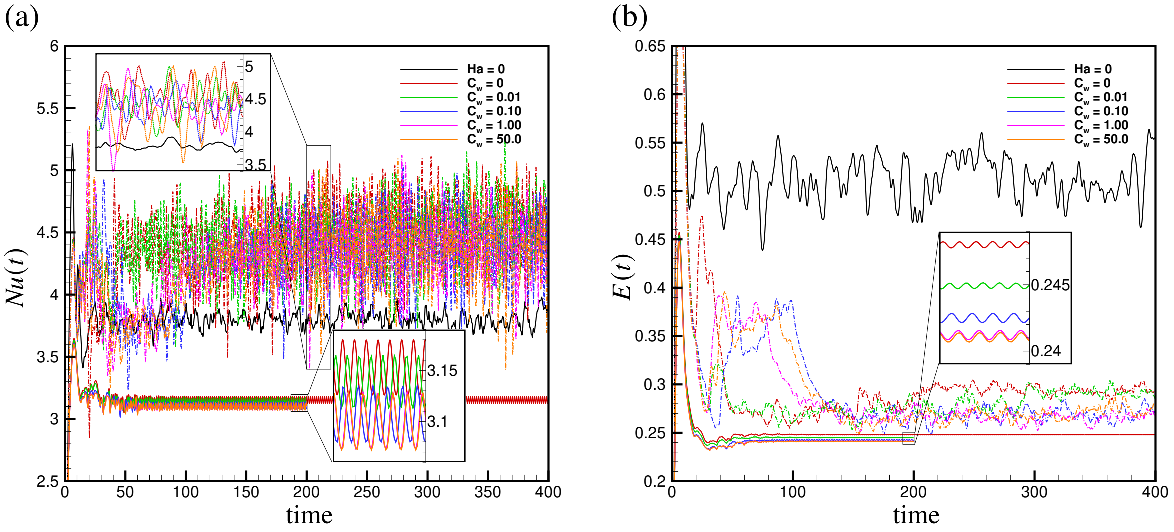

Figure 5.10: *(a)* $Nu(t)$ and *(b)* $E(t)$ (see (3.3) and (3.4)) for $Ha = 325$ (dashed line) and $Ha = 650$ (solid line) for the configuration B of the wall conductivity conditions. Black solid line represents the case $Ha = 0$.

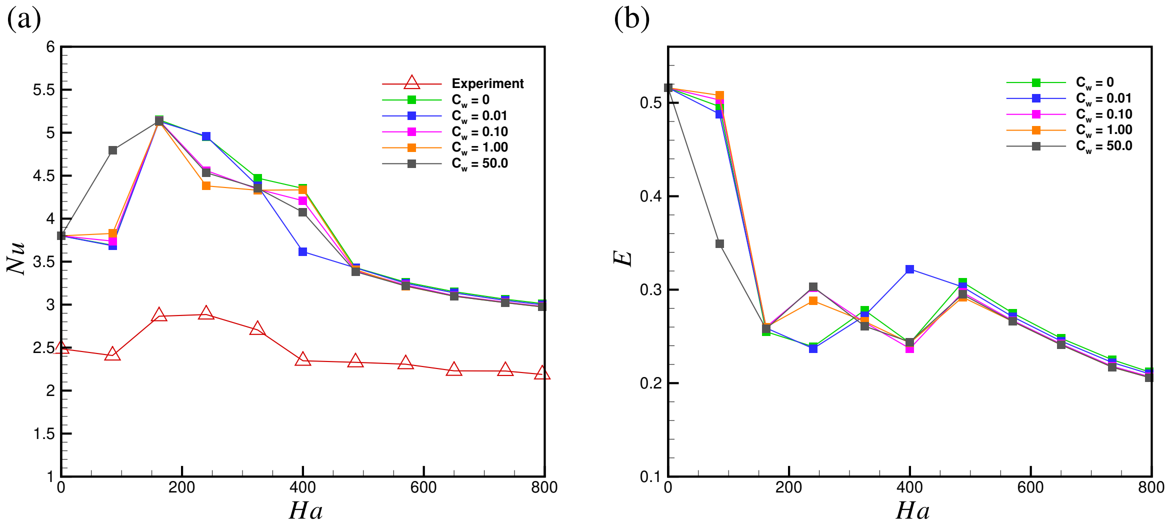

Figure 5.11: Time averaged values of *Nu* and *E* for configuration B (only hot and cold walls are electrically conducting). Data for the case of all walls electrically insulating and the experimental data [16] (available only for *Nu*) are shown for comparison.

5.2 Configuration B: only hot and cold walls are electrically conducting

In experimental setups like those mentioned in [40], the walls responsible for heating and cooling are usually made from copper. This allows the walls to be kept at a constant temperature, while provide adequate heating and cooling. Although in the setup mentioned in [40], the copper walls are coated with an extremely thin layer of epoxy, to make them electrically insulating, it is a reasonable to study the effect of the electrical wall conductivity of these two walls on the evolution and behavior of the flow. Considering these walls to be electrically conducting while other walls are electrically insulating, results in an entirely different flow than what is observed in section 5.1.

Fig. 5.10 shows time signals $Nu(t)$ (3.3) and $E(t)$ (3.4) during the entire simulations for flows at moderately high and high values of *Ha*. It can be seen that unlike the flows with all walls electrically conducting, the fluctuations are only mildly affected by the magnetic field. The flows remain time-dependent at all $0 \leq C_w \leq 50$ and all, but the largest value of *Ha*. At a given value of *Ha* the amplitude of the fluctuations is not significantly affected by C_w. This is illustrated for Ha = 325 and 650 in Fig. 5.10, and is true for all the explored values of *Ha*.

		C_w				
		0	0.01	0.1	1	50
Ha	0			$\overline{3.80}$		
	85	$\overline{3.69}$	$\overline{3.68}$	$\overline{3.74}$	$\overline{3.83}$	$\overline{4.80}$
	162	$\overline{5.15}$	$\overline{5.13}$	$\overline{5.14}$	$\overline{5.13}$	$\overline{5.14}$
	240	$\overline{4.95}$	$\overline{4.96}$	$\overline{4.56}$	$\overline{4.38}$	$\overline{4.53}$
	325	$\overline{4.47}$	$\overline{4.38}$	$\overline{4.34}$	$\overline{4.33}$	$\overline{4.36}$
	400	$\overline{4.35}$	$\overline{3.62}$	$\overline{4.21}$	$\overline{4.34}$	$\overline{4.08}$
	487	$\overline{3.43}$	$\overline{3.43}$	$\overline{3.39}$	$\overline{3.41}$	$\overline{3.38}$
	570	$\overline{3.26}$	$\overline{3.25}$	$\overline{3.23}$	$\overline{3.21}$	$\overline{3.22}$
	650	$\overline{3.15}$	$\overline{3.14}$	$\overline{3.11}$	$\overline{3.10}$	$\overline{3.10}$
	735	$\overline{3.06}$	$\overline{3.05}$	$\overline{3.03}$	$\overline{3.02}$	$\overline{3.02}$
	796	3.01	3.00	2.98	2.97	2.97

Table 5.5: Time averaged values of *Nu* (3.3) computed for the configuration B (hot and cold walls have the same conductance ratio C_w). Values marked with an overline indicate cases in which $Nu(t)$ fluctuates significantly in a fully developed flow. The signal at Ha = 796 is steady-state after an initial transient.

Time averaged results are presented in tables 5.5 and 5.6 and figures 5.11 - 5.17. Tables 5.5 and 5.6 show time-averaged values of *Nu* and *E* respectively for the configuration B. These values are presented in figure 5.11 as well. In contrary to the observations for the configuration A, wall conductivity does not affect the flow drastically, however it still causes changes in the flow field, specially in the low to moderately high Hartmann numbers, in which the flow is sensitive to changes. The values of *Nu* are follows the same trend as the case with electrically insulating walls. It increases to a maximum value in moderate Hartmann numbers and then decrease monotonically by increasing magnetic field intensity. The values of mean kinetic energy *E* have almost the same value as in the case with no wall conductivity, which is explained in section 5.1.1. For some values of Hartmann number, there can be seen a difference between the values of both *Nu* and *E* caused by change in the wall conductance ratio. These changes can be explained by the change in the number of vortices of the large-scale circulation. Table 5.7 shows the number of large vortices that is observed for different values of *Ha* and C_w. In counting these circula-

		C_w				
		0	0.01	0.1	1	50
	0			$\overline{5.16 \times 10^{-1}}$		
	85	$\overline{4.96 \times 10^{-1}}$	$\overline{4.88 \times 10^{-1}}$	$\overline{5.03 \times 10^{-1}}$	$\overline{5.08 \times 10^{-1}}$	$\overline{3.49 \times 10^{-1}}$
	162	$\overline{2.55 \times 10^{-1}}$	$\overline{2.59 \times 10^{-1}}$	$\overline{2.60 \times 10^{-1}}$	$\overline{2.60 \times 10^{-1}}$	$\overline{2.58 \times 10^{-1}}$
	240	$\overline{2.39 \times 10^{-1}}$	$\overline{2.37 \times 10^{-1}}$	$\overline{3.02 \times 10^{-1}}$	$\overline{2.88 \times 10^{-1}}$	$\overline{3.03 \times 10^{-1}}$
Ha	325	$\overline{2.78 \times 10^{-1}}$	$\overline{2.72 \times 10^{-1}}$	$\overline{2.65 \times 10^{-1}}$	$\overline{2.66 \times 10^{-1}}$	$\overline{2.61 \times 10^{-1}}$
	400	$\overline{2.43 \times 10^{-1}}$	$\overline{3.22 \times 10^{-1}}$	$\overline{2.37 \times 10^{-1}}$	$\overline{2.43 \times 10^{-1}}$	$\overline{2.44 \times 10^{-1}}$
	487	$\overline{3.08 \times 10^{-1}}$	$\overline{3.03 \times 10^{-1}}$	$\overline{2.97 \times 10^{-1}}$	$\overline{2.92 \times 10^{-1}}$	$\overline{2.95 \times 10^{-1}}$
	570	$\overline{2.75 \times 10^{-1}}$	$\overline{2.71 \times 10^{-1}}$	$\overline{2.67 \times 10^{-1}}$	$\overline{2.66 \times 10^{-1}}$	$\overline{2.66 \times 10^{-1}}$
	650	$\overline{2.48 \times 10^{-1}}$	$\overline{2.45 \times 10^{-1}}$	$\overline{2.42 \times 10^{-1}}$	$\overline{2.41 \times 10^{-1}}$	$\overline{2.41 \times 10^{-1}}$
	735	$\overline{2.25 \times 10^{-1}}$	$\overline{2.22 \times 10^{-1}}$	$\overline{2.18 \times 10^{-1}}$	$\overline{2.17 \times 10^{-1}}$	$\overline{2.17 \times 10^{-1}}$
	796	2.12×10^{-1}	2.10×10^{-1}	2.07×10^{-1}	2.06×10^{-1}	2.06×10^{-1}

Table 5.6: Time averaged values of E (3.4) computed for the configuration B (hot and cold walls have the same conductance ratio C_w). Values marked with an overline indicate cases in which $Nu(t)$ fluctuates significantly in a fully developed flow. The signal at $Ha = 796$ is steady-state after an initial transient.

		C_w				
		0	0.01	0.1	1	50
	0			turbulent (1)		
	85	1	1	1	1	2
	162	3	3	3	3	3
	240	3	3	2	2	2
	325	2	2	2	2	2
Ha	400	2	1	2	2	2
	487	1	1	1	1	1
	570	1	1	1	1	1
	650	1	1	1	1	1
	735	1	1	1	1	1
	796	1	1	1	1	1

Table 5.7: The number of major eddies in the large-scale circulation for the flows of configuration B.

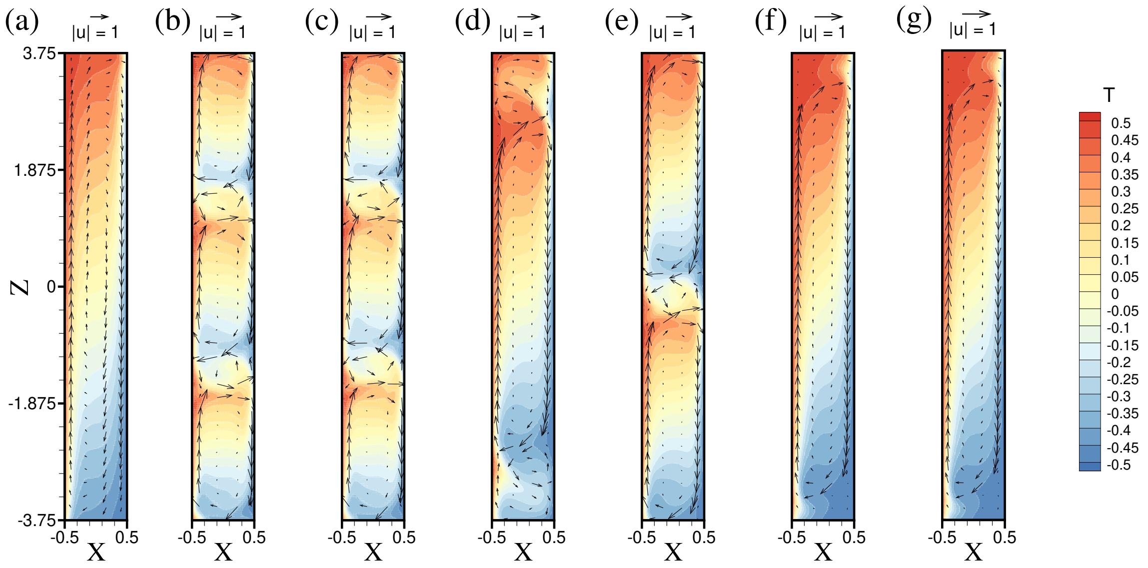

Figure 5.12: Time-averaged distributions of T and a projection of the velocity on the vertical mid-plane cross-section $y = 0$ perpendicular to the magnetic field direction (see Fig. 5.1c) for configuration B. Results for the flows with $Ha = 0$ *(a)*, $Ha = 162$, $C_w = 0.01$ *(b)*, $Ha = 162$, $C_w = 1.0$ *(c)*, $Ha = 400$, $C_w = 0.01$ *(d)*, $Ha = 400$, $C_w = 1.0$ *(e)*, $Ha = 796$, $C_w = 0.01$ *(f)* and $Ha = 796$, $C_w = 1.0$ *(g)* are shown.

tions, the small circulation that may appear in the corners as well as circulations that appear due the change in velocity direction between large cells are not considered.

It is also observed that changing wall conductivity can affect the amplitude of the fluctuations of the *Nu* and *E* by changing the flow structure. The amplitude of such fluctuation has a direct relationship with the number of large vortices that form in the flow field. Since an increase in the number of circulations, results in smaller structures in the flow domain, as well as formation of smaller vortices in between those large structure, and small structures tend to be more unstable, such behavior is expected.

Contrary to what is seen in the configuration A, the effect of electrical conductance of the wall is not substantial, however, it is still causing changes in the flow structure, especially in the moderate Hartman numbers, where the flow seems to be more sensitive to disturbance in the flow. Going past moderate Hartmann numbers, the effect of electrical wall conductivity on the volume averaged properties, e.g. *Nu* and *E*, becomes negligible.

The structure of the mean flow in the case of configuration B is illustrated by the mid-

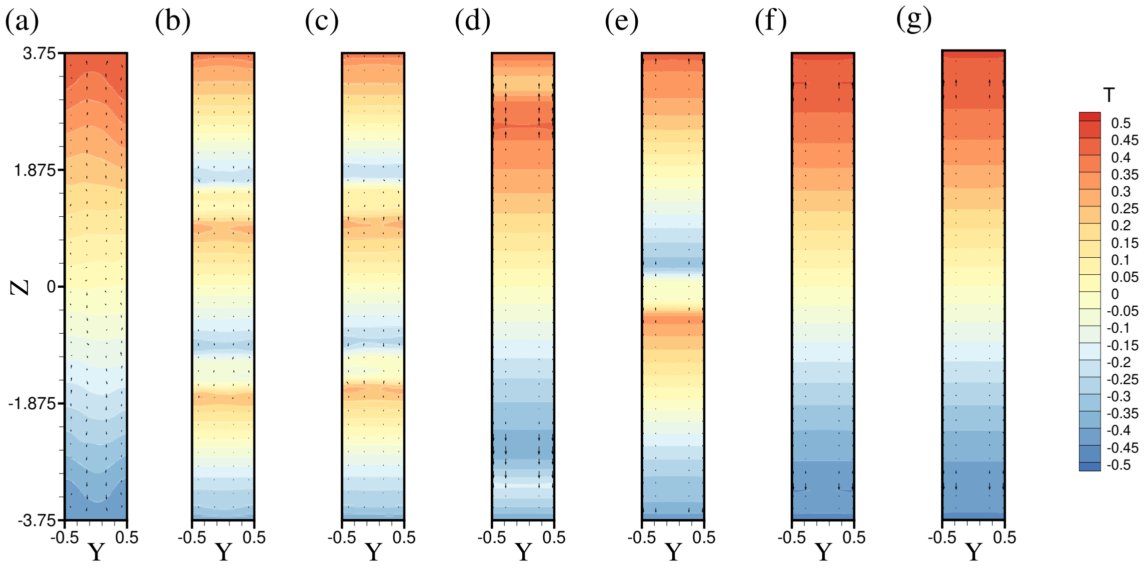

Figure 5.13: Time-averaged distributions of T and a projection of the velocity on the vertical mid-plane cross-section $x = 0$ parallel to the magnetic field direction (see Fig. 5.1c) for configuration B. Results for the flows with $Ha = 0$ *(a)*, $Ha = 162$, $C_w = 0.01$ *(b)*, $Ha = 162$, $C_w = 1.0$ *(c)*, $Ha = 400$, $C_w = 0.01$ *(d)*, $Ha = 400$, $C_w = 1.0$ *(e)*, $Ha = 796$, $C_w = 0.01$ *(f)* and $Ha = 796$, $C_w = 1.0$ *(g)* are shown.

plane distributions in Figs. 5.12, 5.13 and 5.14 and profiles of velocity and temperature in Figs. 5.15-5.17. We see that the effect of the Lorentz force on the flow structure is, in general, much weaker than in the case of configuration A. The width and maximum velocity of near-wall jets are practically unaffected by C_w in the entire range $0 \leq C_w \leq 50$ (only a slight decrease of jet velocity can identified). The effect of Ha at a given C_w is noticeable, but much weaker than for flows with all walls conducting (cf. Figs. 5.15, 5.16 and 5.7, 5.8). Strong jets and large-scale circulation are observed even at the largest $C_w = 50$, $Ha = 796$. Convective heat transfer associated with the strong circulation leads to mean temperature distributions varying only slightly with C_w and Ha and remaining far different from the pure conduction profiles (see Fig. 5.17).

This is behavior can be explained by looking at the current paths in the flow field. Most of current paths are going through Hartmann layer. Introducing wall conductivity results in some of these current paths go through constant temperature walls. In these locations, because the velocities are small, the electrical potential and thus electrical current density are small as well. This results, in small Lorentz force and thus small changes in the flow. However, by increasing the

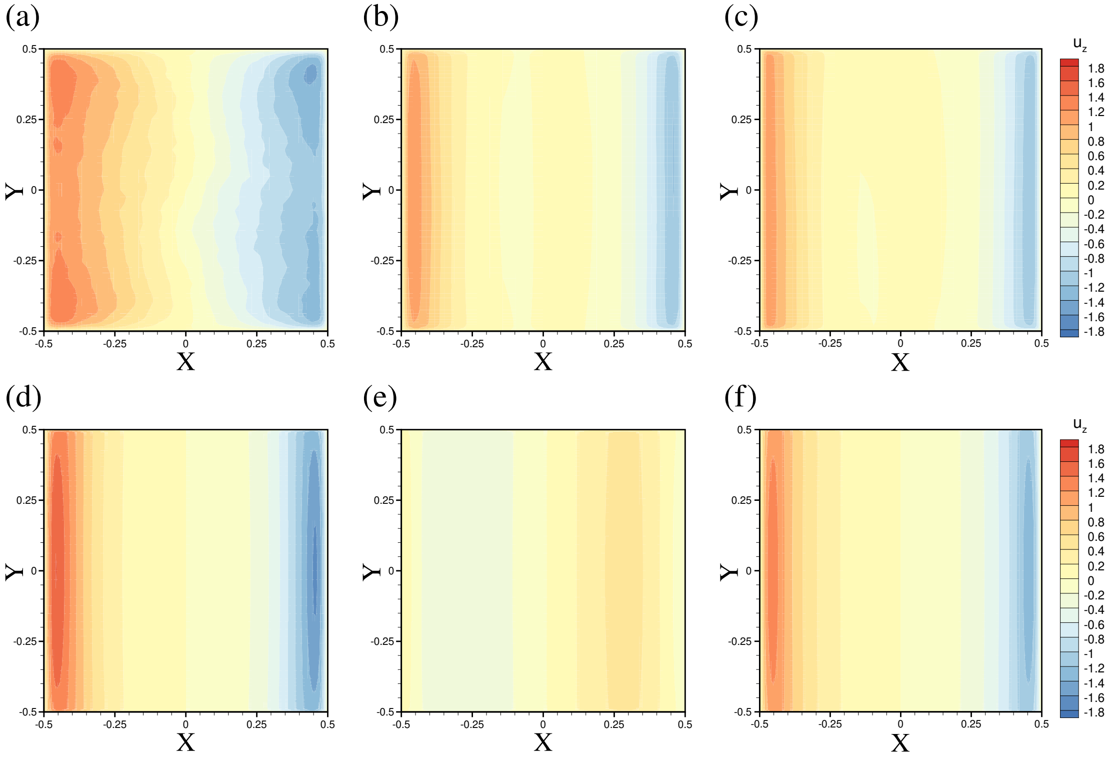

Figure 5.14: Time-averaged distributions of vertical velocity u_z on the horizontal mid-plane cross-section $z = 0$ (see Fig. 5.1c) for configuration B. Results for the flows with $Ha = 0$ *(a)*, $Ha = 162$, $C_w = 0.01$ *(b)*, $Ha = 162$, $C_w = 1.0$ *(c)*, $Ha = 400$, $C_w = 0.01$ *(d)*, $Ha = 400$, $C_w = 1.0$ *(e)* and $Ha = 796$, $C_w = 0.01$ *(f)* are shown.

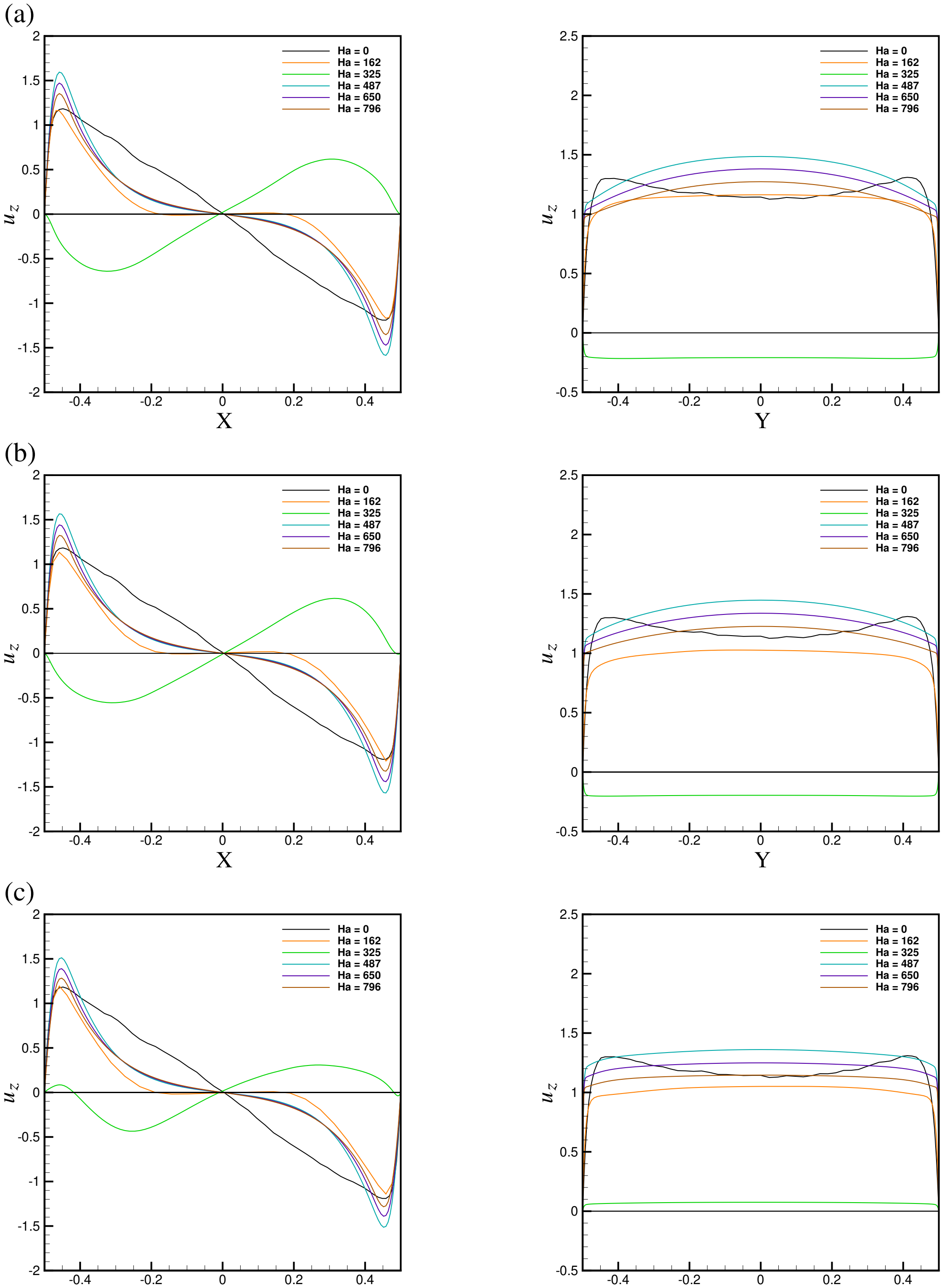

Figure 5.15: Timed-averaged profiles of vertical velocity along the lines $y = 0$, $z = 0$ (left) and $x = -0.47$, $z = 0$ (right) shown in Fig. 5.1b. Results obtained for $C_w = 0$ *(a)* and the configuration B with $C_w = 0.01$ *(b)* and $C_w = 0.1$ *(c)* are shown for various *Ha*.

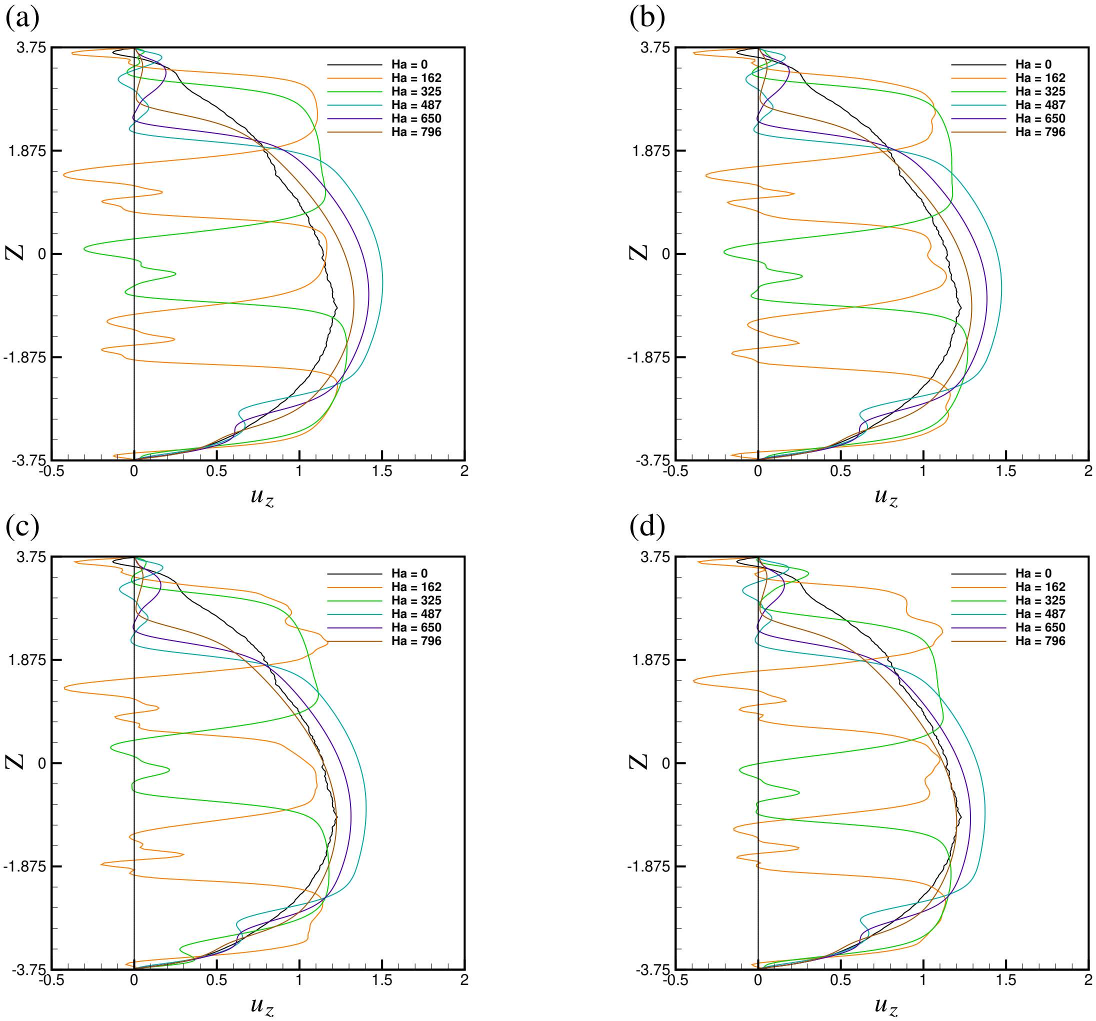

Figure 5.16: Timed-averaged profiles of vertical velocity along the line $x = -0.47$, $y = 0$ shown in Fig. 5.1b. Results obtained for $C_w = 0$ *(a)* and the configuration B with $C_w = 0.01$ *(b)* $C_w = 0.1$ *(c)*, and $C_w = 1.0$ *(d)* are shown for various Ha. A black dotted line indicates $u_z = 0$.

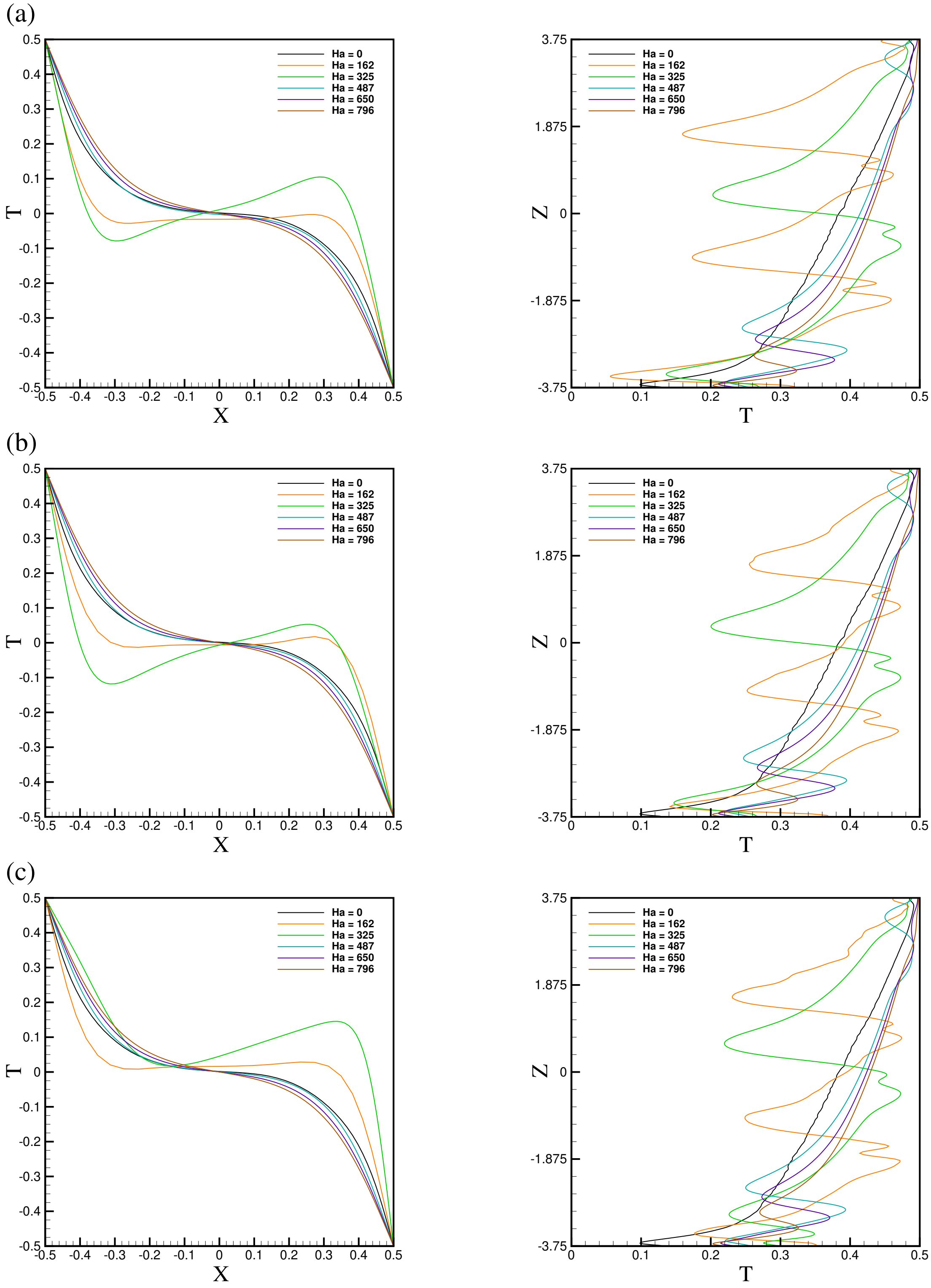

Figure 5.17: Timed-averaged profiles of temperature along the lines $y = 0$, $z = 0$ (left) and $x = -0.47$, $y = 0$ (right) shown in Fig. 5.1b. Results obtained for $C_w = 0$ *(a)* and the configuration B with $C_w = 0.01$ *(b)* and $C_w = 0.1$ *(c)* are shown for various *Ha*.

electrical conductivity of the flow, the portion of current paths going into the walls, increases and thus, the Lorentz force increases. This can explain slightly smaller values of *Nu* and E as wall conductance ratio increases.

The profiles of u_z in the right column of Fig. 5.15 illustrate that the flow approaches a quasi-two-dimensional state at high Ha. Curvature of the core flow profile is still visible, which, as before, can be attributed to large horizontal aspect ratio of the jet, but is much lower than in the case of configuration A. Increasing C_w results in a lower curvature and a more uniform vertical velocity profile in the core flow. The temperature distributions are nearly two-dimensional at high Ha. This indicates that a two-dimensional approximation can be used for the flow. This means that the Q2D approximation in domains similar to what described in this section can be accurate, and its accuracy increases as the electrical wall conductivity in wall at constant temperature increases.

Figure 5.17, shows time-averaged temperature profiles in X and Z directions along the lines shown in 5.1.c for select *Ha* numbers. As it can be seen the effect of wall conductivity on the temperature profiles is negligible, except for low to moderately high *Ha*, which are the flows that are more sensitive than higher flow at higher Ha. The temperature profile at $Ha = 325$ seems to be different than that of flows at other *Ha* due to the fact that this flow has two large scale vortices, which results in a reverse vortex between those two. This can also be seen in the vertical-velocity profile shown in figure 5.15.

5.3 Concluding remarks

A parametric study of the effect of electric conductivity of the walls on magnetoconvection in a tall box with vertical hot and cold walls is carried out. Two configurations of electric boundary conditions are explored. In configuration A, all walls of the box have the same finite electric conductance ratio C_w. In configuration B, only the hot and cold sidewalls are electrically conducting, with the same values of C_w. The other two sidewalls and the top and bottom walls

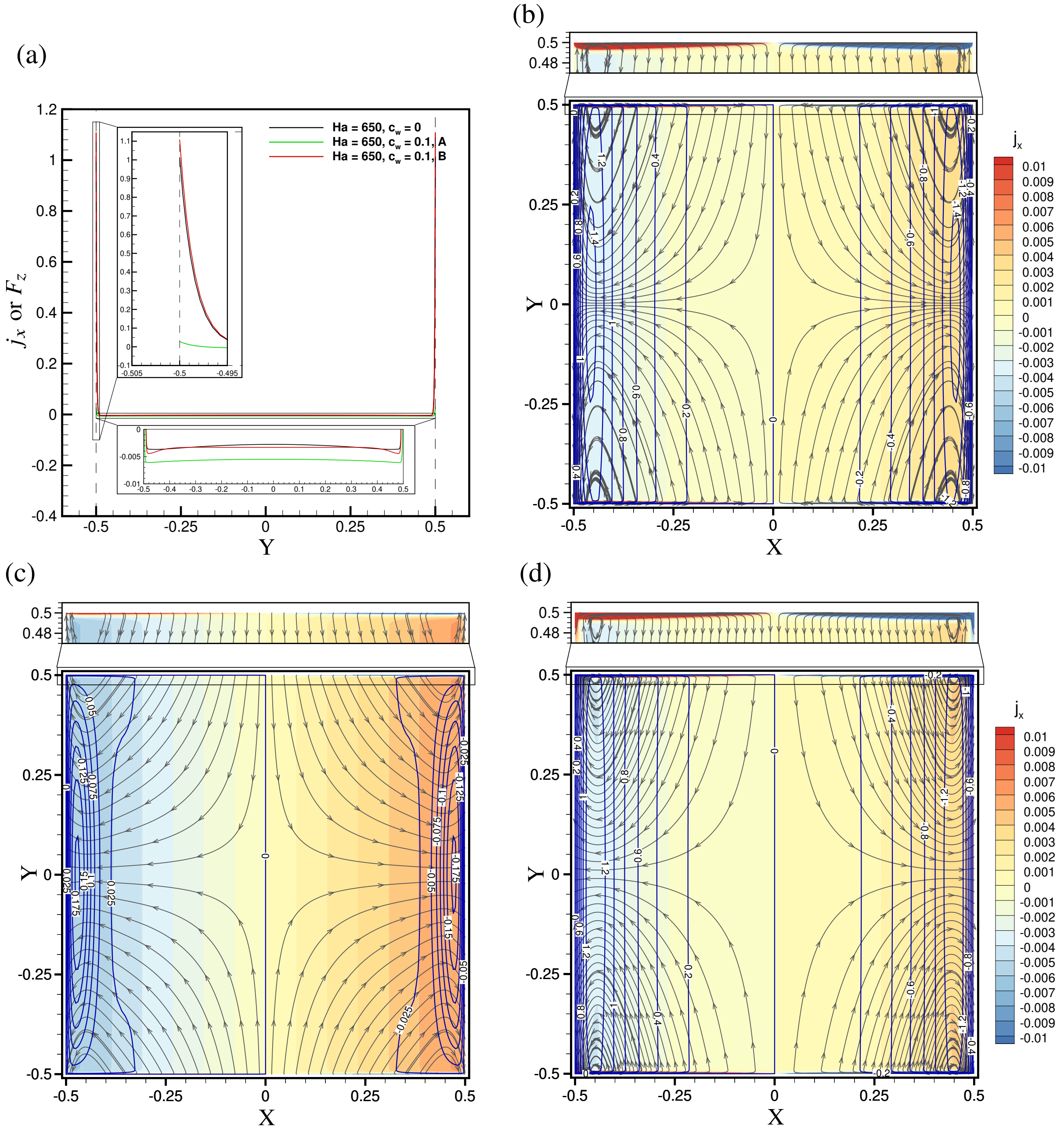

Figure 5.18: *(a)* Timed-averaged profiles of $j_x = F_z$ along the line $x = -0.47$, $z = 0$ parallel to the magnetic field (see Fig. 5.1b). Results obtained at $Ha = 650$ and three wall configurations: $C_w = 0$, configuration A with $C_w = 0.1$, and configuration B with $C_w = 0.1$ are shown. The two zoom-ins show the distributions within the Hartmann layer at the wall $y = -0.5$ and in the core flow. *(b-d)* Time-averaged distributions of the current paths (gray streamlines), the magnitude of $j_x = F_z$ (color), and the vertical velocity v_z (blue iso-lines) in the horizontal mid-plane cross-section $z = 0$ (see Fig. 5.1c). Results for the flows at $Ha = 650$ with $C_w = 0$ *(b)*, configuration A with $C_w = 0.1$ *(c)* and configuration B with $C_w = 0.1$ *(d)* are shown.

are electrically insulating. Numerical simulations are completed at $Pr = 0.025$, $Ra = 7.5 \times 10^5$, $0 \leq Ha \leq 796$, $0 \leq C_w \leq 50$. The new results obtained for flows with conducting walls are compared with those for insulating walls and with the experimental data of [40]. The focus of the analysis is on the effect of the magnetic field and wall conductivity on the structure of the mean flow and the integral properties, such as the Nusselt number Nu and the volume-averaged kinetic energy E.

The convection heat transfer is previously considered to be the result of turbulence on the flow field. This conclusion is mainly based on the studies done on normal (non-MHD) flows. However, results of this study show that at sufficiently high Ha, although the turbulent fluctuations are suppressed, heat transfer can still remains effective. This is a result of stabilization of large structures, i.e, large scale vortices, which are responsible for transferring heat by keeping the flow in motion.

The main finding of the study is the significant impact of the configuration of wall conductivities on the MHD transformation of the flow. When all walls are electrically conducting (configuration A), the transformation can be described as a straightforward suppression. Increasing the strength of the magnetic field leads to the damping of velocity fluctuations, reduction in the strength and simplification of the shape of large-scale circulation, and a decrease in Nu and E. The effect is stronger at higher C_w. At $C_w \geq 0.1$ and high Ha, the heat transfer is reduced to nearly pure conduction.

The effect of the magnetic field on the flow is entirely different when only the sidewalls parallel to the magnetic field are electrically conducting (configuration B). The suppression of the flow is much weaker. The flow retains strong large-scale circulation and high values of Nu and E in the entire range $0 \leq Ha \leq 796$. Velocity fluctuations persist in fully developed flows, except in the case of the highest considered value $Ha = 796$. Interestingly, the variation of the electric conductivity of the hot and cold walls in the range between perfect insulation $C_w = 0$ and nearly perfect conduction $C_w = 50$ does not have a significant impact on flow properties. The few exceptions are examples of a subtle effect, where a change in C_w alters the number of loops in the large-scale circulation.

To explain the profound difference between the MHD responses of the two wall configurations, we consider the typical time-averaged distributions of induced electric currents and Lorentz forces. The focus is on the vertical component F_z of the force, which directly affects near-wall jets. This component has the same value as the component j_x of the current. The flows at $Ha = 650$ are considered for three sets of wall conductivities: $C_w = 0$; $C_w = 0.1$ in configuration A; and $C_w = 0.1$ in configuration B.

In Fig. 5.18a, profiles of time-averaged j_x are shown along the line $x = -0.47$, $z = 0$, parallel to the magnetic field and located within the upward jet near the hot wall. The fields of time-averaged j_x, vertical velocity v_z, and current paths in the horizontal mid-plane cross-section $z = 0$ are depicted for each of the three aforementioned cases in Figs. 5.18b-d.

The explanation illustrated by Fig. 5.18 is based on the effect of the conductivity of the Hartmann walls at $y = \pm 0.5$ on the distribution of the induced electric currents. We have already discussed this effect, based on general physical arguments, in chapter 1. If the walls are electrically insulating (as in the case of $C_w = 0$ and in configuration B with $C_w = 0.1$), the current loops close within the thin Hartmann boundary layers (see the insert at $y = -0.5$ in Fig. 5.18a and Figs. 5.18b,d) implying strong currents and significant electric resistance to them. The cumulative result is the increase of the total electric resistance of the fluid domain to the induced electric currents. This does not occur or is weakened in the case of configuration A, when the walls at $y = \pm 0.5$ are electrically conducting, so the current loops may also close through them (see Fig. 5.18c).

We observe in Fig. 5.18 that wall conductivity does not have a significant effect on the pattern of induced currents in the core flow, including the zones of the upward and downward jets. However, it does significantly modify the current strength. The insert in Fig. 5.18a and the distributions of j_x in Figs. 5.18b-d show that the magnitude of j_x and, consequently, F_z in the jet's area is approximately twice as large in the case of configuration A compared to $C_w = 0$ or configuration B. Since the component F_z opposes the jet's vertical velocity, the damping of the jets by the Lorentz force is significantly stronger in the case of configuration A, i.e., when the walls perpendicular to the magnetic field are electrically conducting.

The just provided explanation is consistent with the effect of the wall conductivity of the integral flow properties detected in our simulations. The explanation implies a profound change of the flow and its integral characteristics when the value of $C_w^{Ha} = C_w Ha$ is not small. For the configuration A, this includes all our cases with non-zero C_w, since the smallest C_w^{Ha} found at C_w=0.01 and $Ha = 85$ is 0.85. The profound effect is visible for all the simulations with non-zero C_w in figure 5.3. The Hartmann walls remain insulating for all the simulations of the configuration B. Accordingly, the variations of Nu and E with C_w are small in figure 5.11.

Two other conclusions can be drawn from the results presented in this study. One concerns the applicability of the two-dimensional approximation, generally possible for high-Ha MHD flows, in which velocity and temperature distributions are nearly uniform in the direction of the magnetic field within the core flow, to magnetoconvection. It has been long understood that applicability of the approximation requires that the imposed temperature gradient is perpendicular to the magnetic field [11]. Our results show that the accuracy of the approximation can be low even when this requirement is met. We see in Figs. 5.8 and 5.16 that vertical velocity u_z varies significantly in the field direction in the core flow even at the highest Ha considered here.

Another comment concerns the disagreement between the data of the experiment [16] proposed as a benchmark for MHD numerical models [41] and our computational data (see Figs. 5.3a and 5.11a). A similar disagreement was observed in Ref. [16] and attributed in Ref. [41] to either imperfection of the experiment or insufficient accuracy of the numerical model in Ref. [16]. The fact that a similar disagreement is found in our simulations on a much finer grid allows us to exclude the latter possibility. The data in Fig. 5.11a also show that the disagreement cannot be caused by imperfect electric insulation of the hot and cold walls in the experiment. The most plausible remaining explanation appears to be the difficulty of maintaining the condition of constant uniform temperature of hot and cold walls in the experimental setup.

CHAPTER 6

Dynamics of A Thermal Plume Affected by A Magnetic Field

This study aims to understand how thermal plumes form, develop and behave in a liquid metal in the presence of an imposed strong magnetic field. Thermal plumes can exist in context of natural convection flows [48]. They are convective motion originated from localized heat sources, where hot fluid penetrates into a colder region above [49, 50]. The heat source causes an increase in the temperature of the fluid near it, which results in increasing buoyancy of the fluid. This lead to the development of a primary fluid pattern which evolves finally to a well known thermal plume [51].

Thermal plumes behavior under the influence of magnetic field is different from that of thermal plumes seen in normal (non-MHD) flows. They are elongated in the direction of the magnetic field, and, as they develop, they, based on the direction of the magnetic field, may become unstable and oscillate perpendicular to direction of the magnetic field [52, 53]. Previous studies of bubble-driven liquid metal plume in an enclosure revealed that the behavior of the plume depends on the direction of the applied magnetic field. A vertically applied magnetic field observed to results in a straight uniform damping of the mean flow [52]. However, transverse applied magnetic field is shown to lead to a completely different flow regime. It creates a transient structure which is oscillating with predominant frequencies [53].

It is important to mention that the Rayleigh-Bénard Convection in liquid metals has been subject of many studies [17, 54, 55, 56, 57, 58, 59]. One of the main mechanism of such convection flow is the formation of thermal plumes, which as it is previously stated, is the main mechanism of heat transfer. Unlike the previous researches done on the plumes in liquid metal flows or non-MHD plumes, in this work, artificially created isolated thermal plume is studied. To the best knowledge of author, this is the first analysis of an isolated MHD thermal plume.

The study was conducted with two different setups. In the first setup, an isolated plume was generated from a point heat source in the lower half of a cubic box with walls located far from heat source. The motivation for setup is to understand how a plume behaves when it has large enough space to grow. In the other setup, the artificial isolated plume is created using a thin wire located in the middle of an elongated vertical box. This setup is used to provide numerical simulations for possibility of comparison with future experiments.

In both of these cases the boundary temperatures are considered to be constant, and have the same non-dimensional value $T = 0$. A uniform temperature distribution of $T = 0$ is used to initialize the flow. The heat generation term q in (2.20) is chosen such that the volumetric average of the heat generation rate is $\forall^{-1}\left(\int q d\forall\right) = 1$. In order to identify if the flow reaches its fully-developed state, the total heat out-flux from the walls per unit volume $\langle q_{out}\rangle = q_{tot,out}/\forall$ is calculated and recorded with time, and the flow is considered to be in fully-developed state when this value is unity or it fluctuates around a constant mean.

6.1 Heat generation from point heat source

In this setup, the formation and behavior of an isolated thermal plume is studied. The flow domain is a cubic box with a point heat source located in the lower quarter of the box. Since in the numerical simulations, a point heat source result in numerical challenges, due to extreme gradients around the point, heat source is considered to be a sphere with diameter d. In the spherical heat generation region, three different heat generation functions q, were tested. A uniform function, in which all grid points inside the heating region has a same numerical value, hereon called Top-hat function. A cosine distribution to enhance the numerical properties by easing the transi-

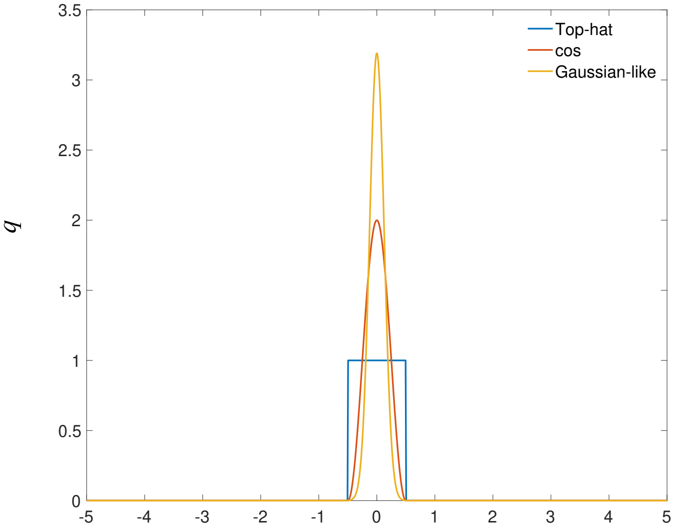

Figure 6.1: Two-dimension illustration of different heat generation functions.

tion between the inside and outside of heat generation region and avoiding high gradients at the sphere boundary. And last one, is a Gaussian-like function, to increase the heat generation in the middle of the sphere, thus make it more similar to a point heat source. These functions are:

$$q(x,y,z) = \begin{cases} c_1 & \text{Top-hat (uniform) function} \\ c_2\cos(\pi r)+1 & \text{cos function} \\ c_3\exp(-32r^2) & \text{Gaussian-like function} \end{cases} , \tag{6.1}$$

$$r(x,y,z) = \sqrt{(x-x_0)^2+(y-y_0)^2+(z-z_0)^2} , \tag{6.2}$$

where, r is the distance between the point (x,y,z) and the center of heating sphere (x_0,y_0,z_0). Values c_1, c_2 and c_3 chosen in a way to enforce volume average total heat generation to be unity. For points with $r > d/2$ the value for q is zero $q = 0$. For comparison, a two-dimension illustration of these functions are shown in figure 6.1.

In order to prevent imposed boundary limitation on the plume, the flow domain is taken to

Property	$L_x \times L_y \times L_z$	Ra	Pr	Ha
Value	$10 \times 10 \times 10$	10^4	0.025	$0, 50, 100, 200, 400$

Table 6.1: Non-dimensional geometry and parameters of the studied flow, (see text for a detailed discussion and definition of Ra, Pr, and Ha in (2.30)).

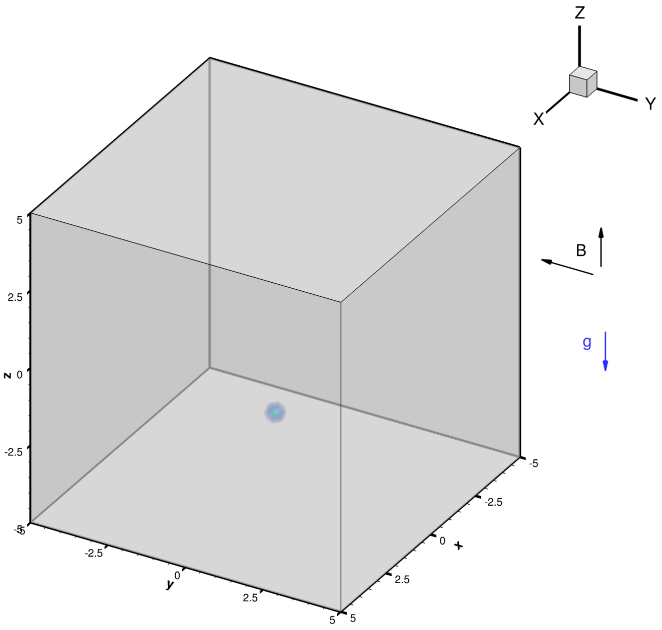

Figure 6.2: Three-dimensional illustration of the setup used to study isolated plume in a cubic box. The location of the heating sphere is shown in the box. The direction of the gravity is shown by the blue vector. The direction of imposed magnetic field is shown by black vectors.

be much bigger than the heat generation sphere $L_x = 10 \gg d$. The center of the heating zone is located at $(x_0, y_0, z_0) = (0, 0, -2.5)$. All surrounding walls have constant temperature $T|_{bnd} = 0$ and are electrically insulating $C_w = 0$. Two different directions of magnetic field are considered; transverse and vertical magnetic fields. It will be shown later, that these two result in completely different flow regimes. Table 6.1 lists the non-dimensional parameters for this setup. Figure 6.2 illustrates the flow domain as well as directions of magnetic field and gravity considered in this problem.

Five different numerical grids were used for this study. They are listed in table 6.2. Since our study showed that plume can start to oscillate and the location and the amplitude of these oscillations were not known, all the grids are uniform in all three directions. Another reason to use

Grid #	N_x	N_y	N_z	Clustering		
				x	y	z
1	64	64	64	$\gamma = 0$	$\gamma = 0$	$\gamma = 0$
2	128	128	128	$\gamma = 0$	$\gamma = 0$	$\gamma = 0$
3	256	256	256	$\gamma = 0$	$\gamma = 0$	$\gamma = 0$
4	384	384	384	$\gamma = 0$	$\gamma = 0$	$\gamma = 0$
5	512	512	512	$\gamma = 0$	$\gamma = 0$	$\gamma = 0$

Table 6.2: Different grid parameters used for grid sensitivity study of the plume generated by a point heat source. The last three columns show the types and parameters of grid clustering in each direction: blended Chebyshev and uniform grids (3.1) with the weight γ, hyperbolic tangent (3.2) with the clustering coefficient A, and a purely uniform grid $\gamma = 0$.

uniform grid was due to the fact that the numerical solver used for this study, will use cos transform rather than eigenvalue decomposition for unifor grids, which results in much faster simulations. The grid sensitivity study was done in different parts.

First using top-hat distribution for q (6.1), the non-MHD $Ha = 0$ flow was simulated using all five different grids for 100 non-dimensional time units. All of these simulations started from the same initial condition of uniform temperature distribution $T = 0$, and random velocity with amplitude of 10^{-3}. The time signals of the volume averaged outward heat flux $\langle q_{out} \rangle$, temperature T_{avg} and kinetic energy E_{avg} is shown in figure 6.3. It can be seen that the grid #1 ($N = 64$) cannot produce acceptable results. Other than that, other numerical grids appears to have acceptable results. However, looking at temperature distribution in the flow field, grid #2 ($N = 128$) produces regions with negative temperature which is physically incorrect. A further investigation showed that these negative temperatures are located exactly under the heat generating sphere, which was caused by high gradients resulting from top-hat q function.

As a result of this observation, two other heat generation distribution was tested. In order to understand the differences between these heat generation functions another set of simulations was performed. In these simulations, non-MHD flow $Ha = 0$ was solved using grids #2 ($N = 128$) and #3 ($N = 256$). The initial condition used for these analysis –except the top-hat simulation– was the result of the numerical study of the case with $Ha = 0$ and grid #5 ($N = 512$) after 100 non-dimensional time units. The results are shown in figure 6.4. Based on these results

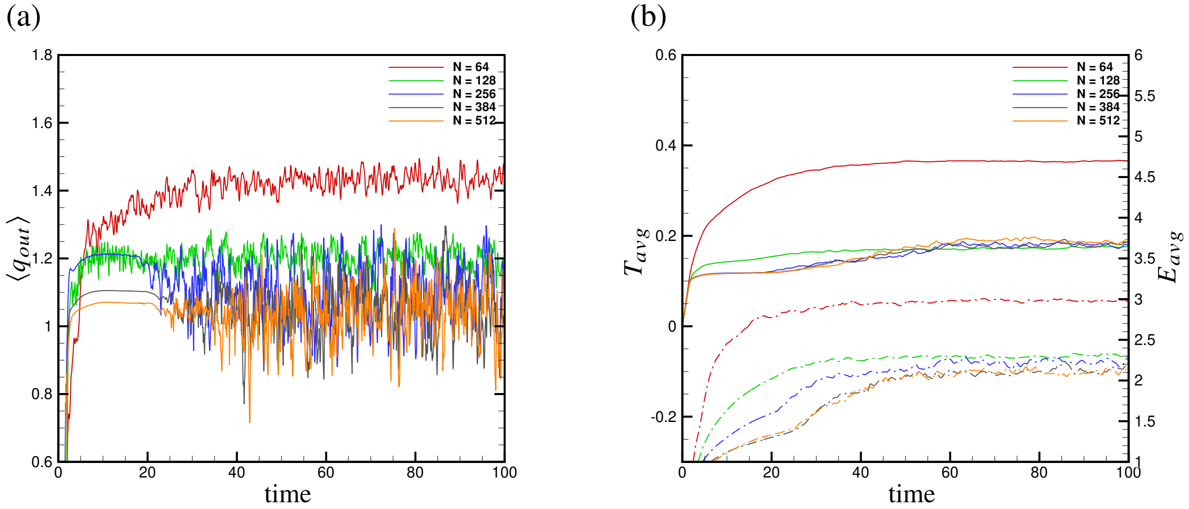

Figure 6.3: Time signals of $\langle q_{out} \rangle$ *(a)* and T_{avg} and E_{avg} *(b)* $Ha = 0$ and top-hat heat generation function for different grids. In figure *(b)* the T_{avg} and E_{avg} are shown using a solid line and a dashed line, respectively.

it was decided to perform the study using the Gaussian-like heat generation function.

In these simulation, also two different ways of calculating outward heat flux was used. One is calculating using the surface integral on all boundaries $\left(\int_A \left(\frac{\partial T}{\partial n}\right) dA\right)$ and the other was using the volume integral of Laplacian of the temperature $\left(\int_V \left(\nabla^2 T\right) dV\right)$. The difference between these two values is due to the numerical resolution of the grid. This was verified using numerical simulations over a much smaller domain $L_x = 2$.

Considering the results obtained from these simulations, the rest of the cases was simulated using Gaussian-like heat generation function and the solver calculated outward heat flux using $\left(\int_V \left(\nabla^2 T\right) dV\right)$. A new procedure was used to perform the grid studies for the cases with $Ha > 0$. Using the result of $Ha = 0$ and $N = 512$ as initial condition, the simulations were performed for different values of Ha and both the vertical and transverse magnetic field. These simulation were initially performed for 100 non-dimensional units on the grid #2 ($N = 128$). Then using the result from grid #2 simulations as initial condition, numerical studies were continued on grids #2 and #3 for another 100 non-dimensional time units. Lastly, using the result of grid #3 as initial condition for grid #4 ($N = 384$), simulation continued for either 50 or 100 non-dimensional time unites for all three grids. The decision to continue simulations further than 50

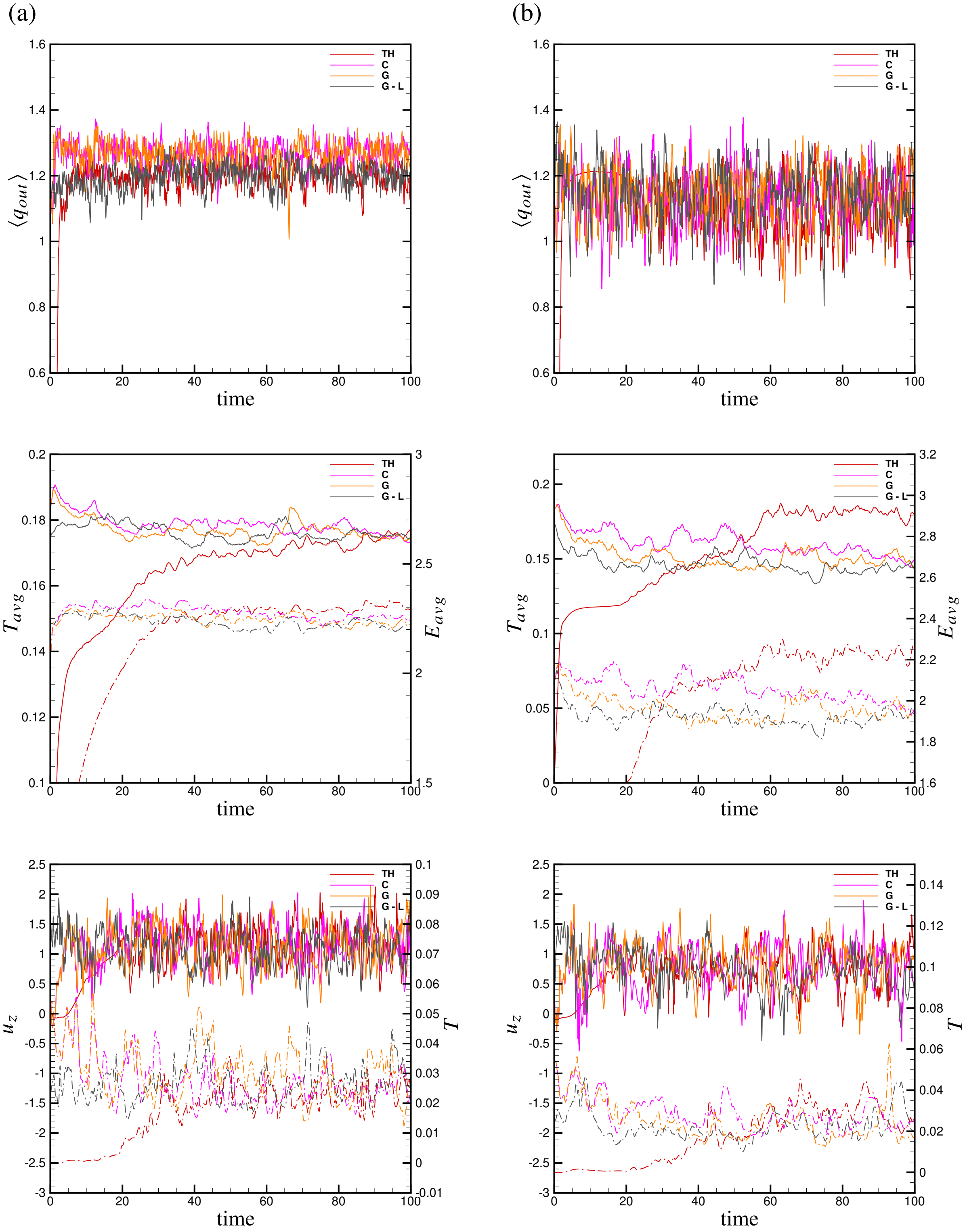

Figure 6.4: Time signals of $\langle q_{out} \rangle$ (top row), T_{avg} and E_{avg} (middle row) and u_z and T at $(x, y, z) = (-2.5, 0, 0)$ (bottom row) for $Ha = 0$ and $N = 128$ *(a)* and $N = 256$ *(b)* using different functions for heat source. T_{avg} and u_z are shown using a solid line. E_{avg} and T are shown using a dashed line. Black lines correspond to the simulation in which the $\langle q_{out} \rangle$ was calculated using $\nabla^2 T$.

time units were based on the development of time signals.

In what follows results of grid study are shown using time signals of volume averaged outward heat flux, volume averaged temperature and volume averaged kinetic energy. These results are discussed in two parts. First, the results of the flow with horizontal imposed magnetic field, and next results of the case with vertical imposed magnetic field.

6.1.1 Horizontal magnetic field

Figures 6.5 and 6.6 shows the time signals for volume averaged outward heat flux and volume averaged temperature and kinetic energy respectively. They show the numerical grid #2 is not producing sufficient results. On the other hand, the grids #3 and #4 shows a good agreement in both the volume averaged outward heat flux and temperature, except for the case with $Ha = 50$.

Based on the result of this grid study, two-dimensional contours of vertical velocity is shown through box mid-planes in figures 6.7, 6.8 and 6.9. Figure 6.9 also includes in-plane velocity vectors. For the case of non-MHD flow ($Ha = 0$), the plume and fluid flow around the plume is turbulent. One of the most prominent features of buoyant plumes is the phenomenon of puffing [60, 61], which is the periodic shedding of large vortical structures from the plume flows due to the buoyant flow instability. This puffing or periodic oscillatory behavior is the most prominent feature of buoyant plumes in the transitional regime [62]. This phenomenon can be observed in this state of the flow.

It is also important to point out that the volume averaged outward heat flux is expected to have an average value of unity, which is not the case in the time signals shown. This relates to the fact the the grid resolution used to perform the numerical study is not sufficient to capture gradients accurately. However, as the Ha increases and the fluctuation in the flow domain decreases the error of the outward heat flux decreases.

Introducing magnetic field, as expected, results in suppression of the gradients along the magnetic field, as well as suppression of turbulent structures. when there is no magnetic field, the flow has positive vertical velocity in the bottom, then reaches to top of the box, gets colder

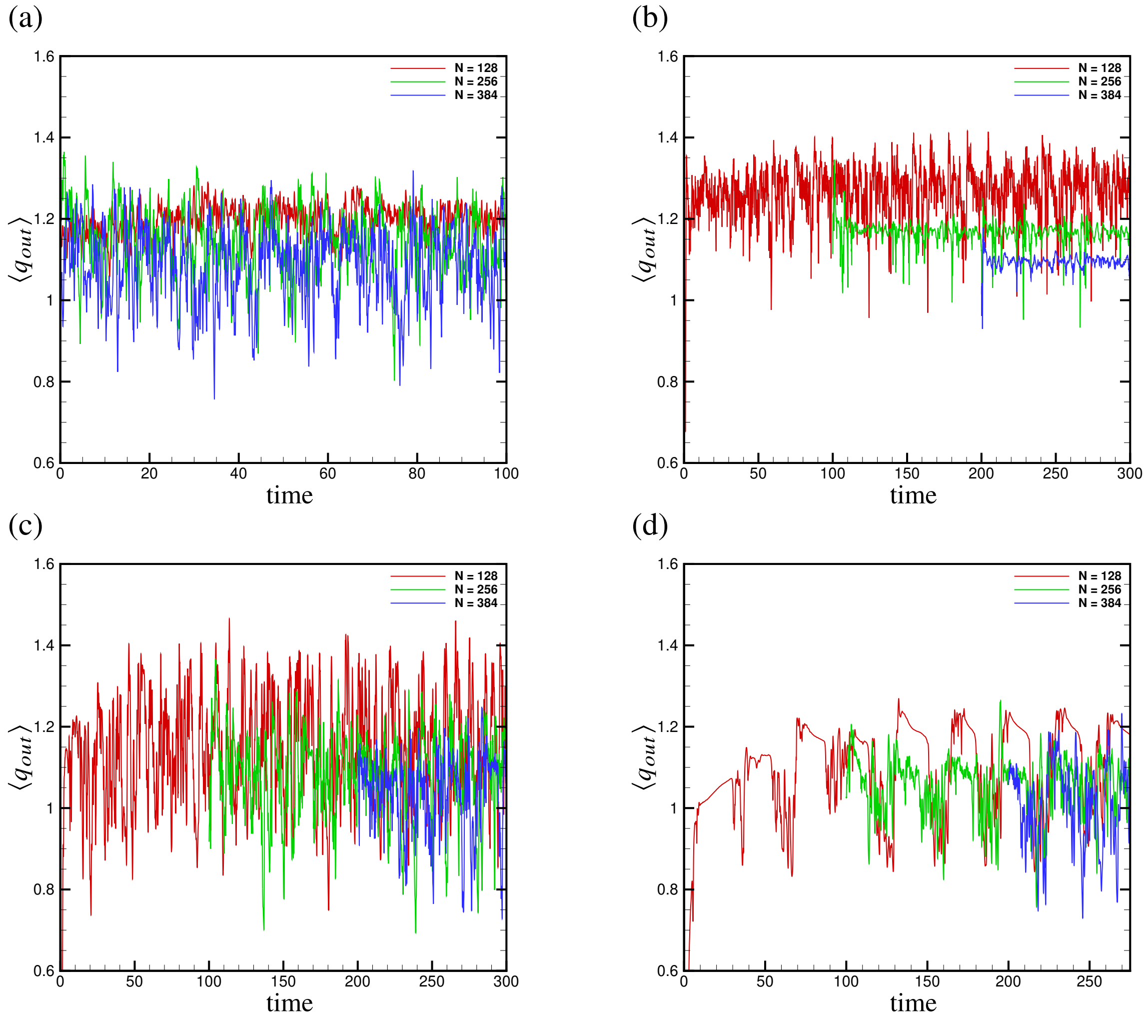

Figure 6.5: Time signals of $\langle q_{out} \rangle$ for $Ha = 0$ *(a)*, $Ha = 50$ *(b)*, $Ha = 100$ *(c)*, and $Ha = 200$ *(d)*. These results are for Gaussian-like heat generation and $\langle q_{out} \rangle$ is calculated using volume integral of $\nabla^2 T$.

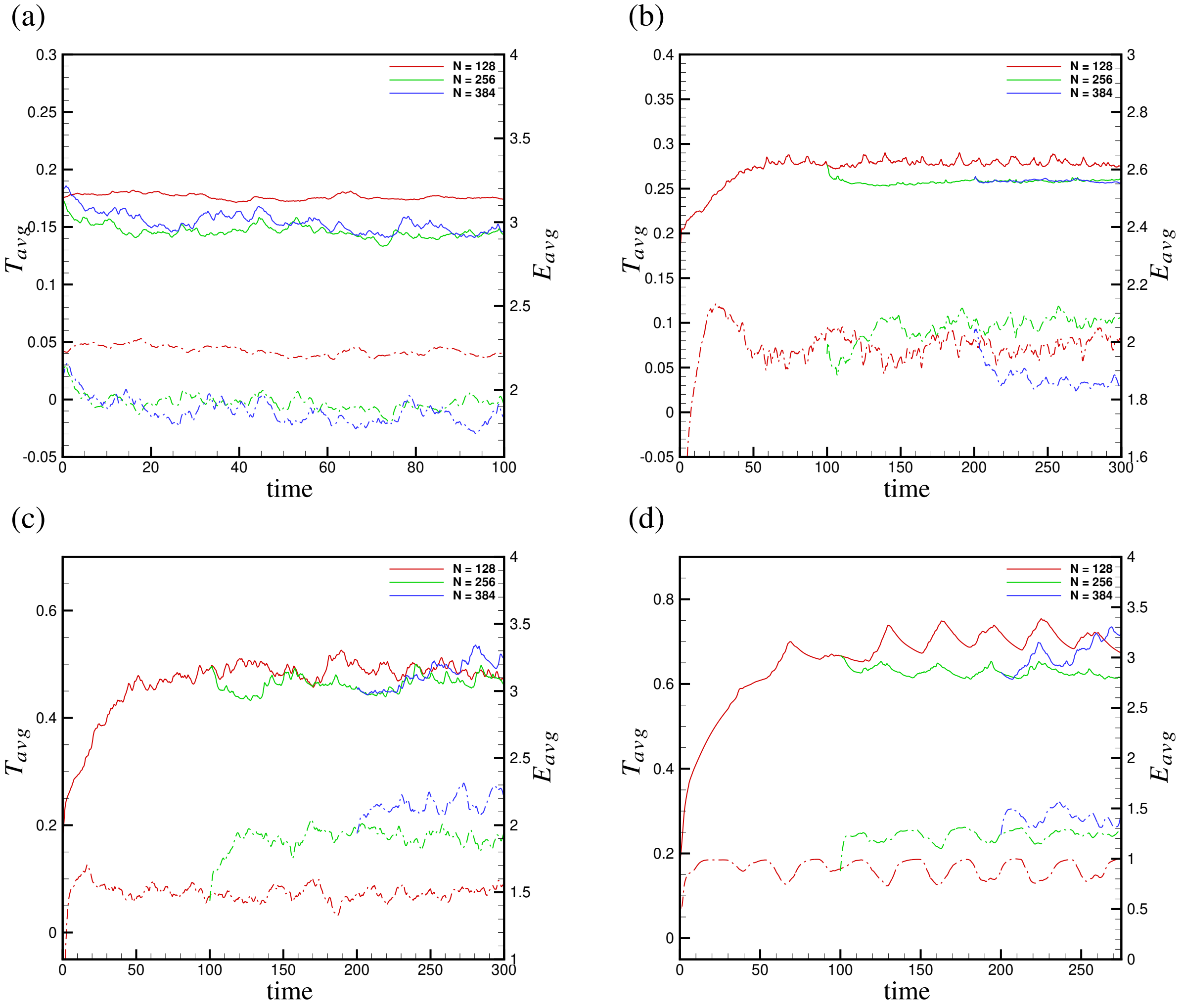

Figure 6.6: Time signals of T_{avg} and E_{avg} for $Ha = 0$ *(a)*, $Ha = 50$ *(b)*, $Ha = 100$ *(c)*, and $Ha = 200$ *(d)*. These results are for Gaussian-like heat generation and $\langle q_{out} \rangle$ is calculated using volume integral of $\nabla^2 T$. T_{avg} and E_{avg} are shown using a solid line and a dashed line, respectively.

and descend near the side walls of the box. However, when there is a horizontal magnetic field, the flow regime is completely different. The plume will be elongated in direction of the magnetic field which results in a combination of downward and upward flow near the Hartmann walls – walls perpendicular to the magnetic field. The main downward motion of the flow in these cases is happening at the other two side walls –parallel to the magnetic field.

Another important observation phenomenon is that at moderate magnetic field intensities $Ha \leq 200$, the plume has oscillating behavior. Amplitude and frequency of such oscillations increase from $Ha = 50$ to $Ha = 100$, subsequently decrease at $Ha = 200$ and eventually disappear at $Ha = 400$. This behavior can also be seen in the figures 6.5 and 6.6.

There are several issues with the numerical simulation of this problem. First, since the diameter of the heat generation zone is much smaller than the box dimensions, there is a high temperature gradient near the center of heat generation zone. In addition to that, introducing magnetic field, and the fact that the walls are electrically insulating, results in formation of the Hartmann boundary layers at Hartmann walls. The thickness of these boundary layers decrease as the intensity of the magnetic field increases. As a result higher resolution grid is required to be able to resolve those boundaries accurately.

6.1.2 Vertical magnetic field

Applying vertical magnetic field will result in a completely different flow formation. The first observation is all the fluctuation are suppressed. This may be in contrary to the time signals shown in figure 6.10, but those fluctuations are only seen in grid #2, which is a lower resolution grid. This behavior is believed to be a result of numerical artifacts rather then the physics of the problem.

Looking at vertical velocity contours, it can be seen that by increasing the intensity of the magnetic field, the plume becomes weaker which is an expected behavior of the MHD flows. On the other hand the instabilities seen at moderate Ha in the previous case is not seen here. The plume has no oscillating behavior.

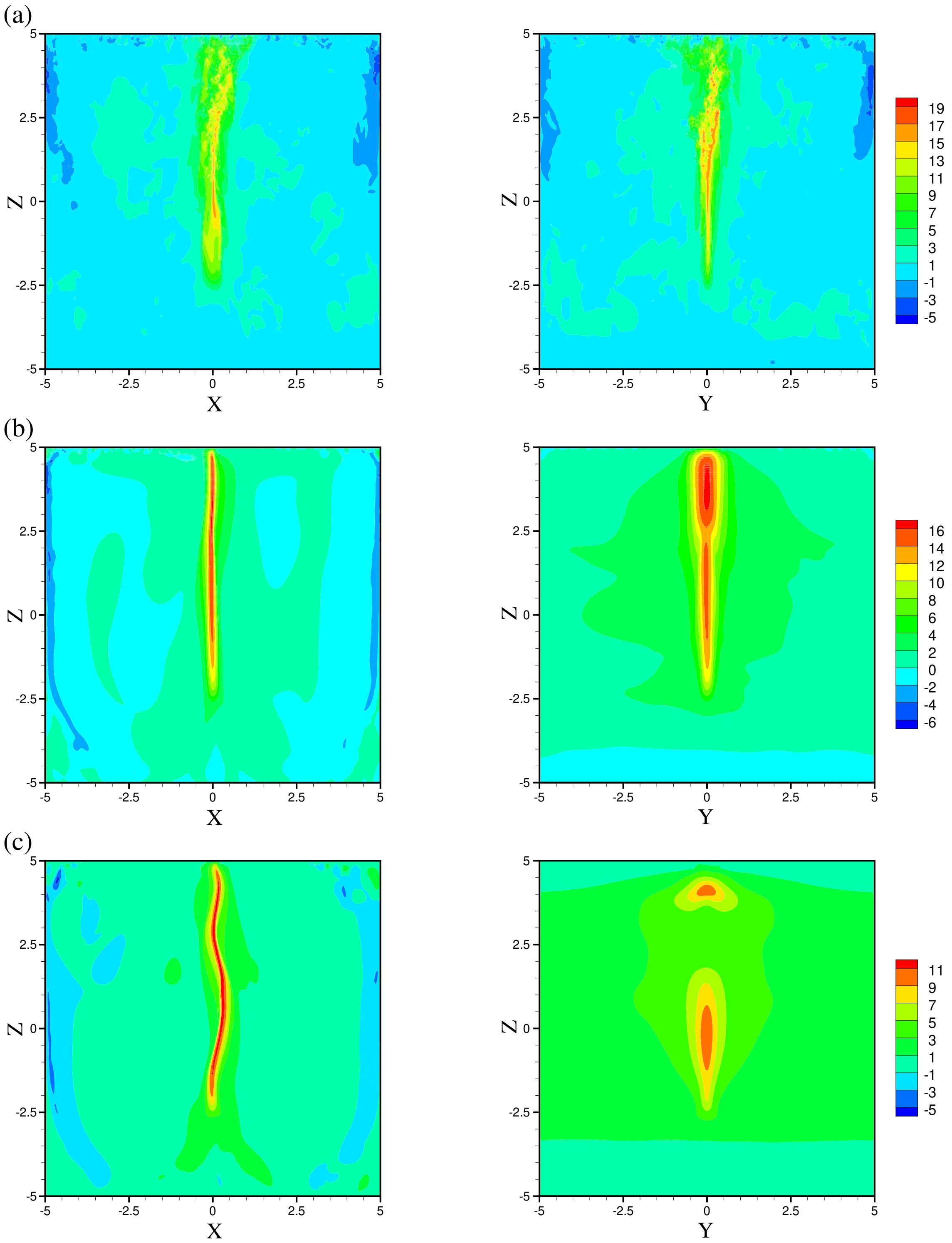

Figure 6.7: Two-dimensional vertical velocity u_z contours at vertical mid-planes for $Ha = 0$ *(a)*, $Ha = 50$ *(b)* and $Ha = 100$ *(c)* with horizontal imposed magnetic field

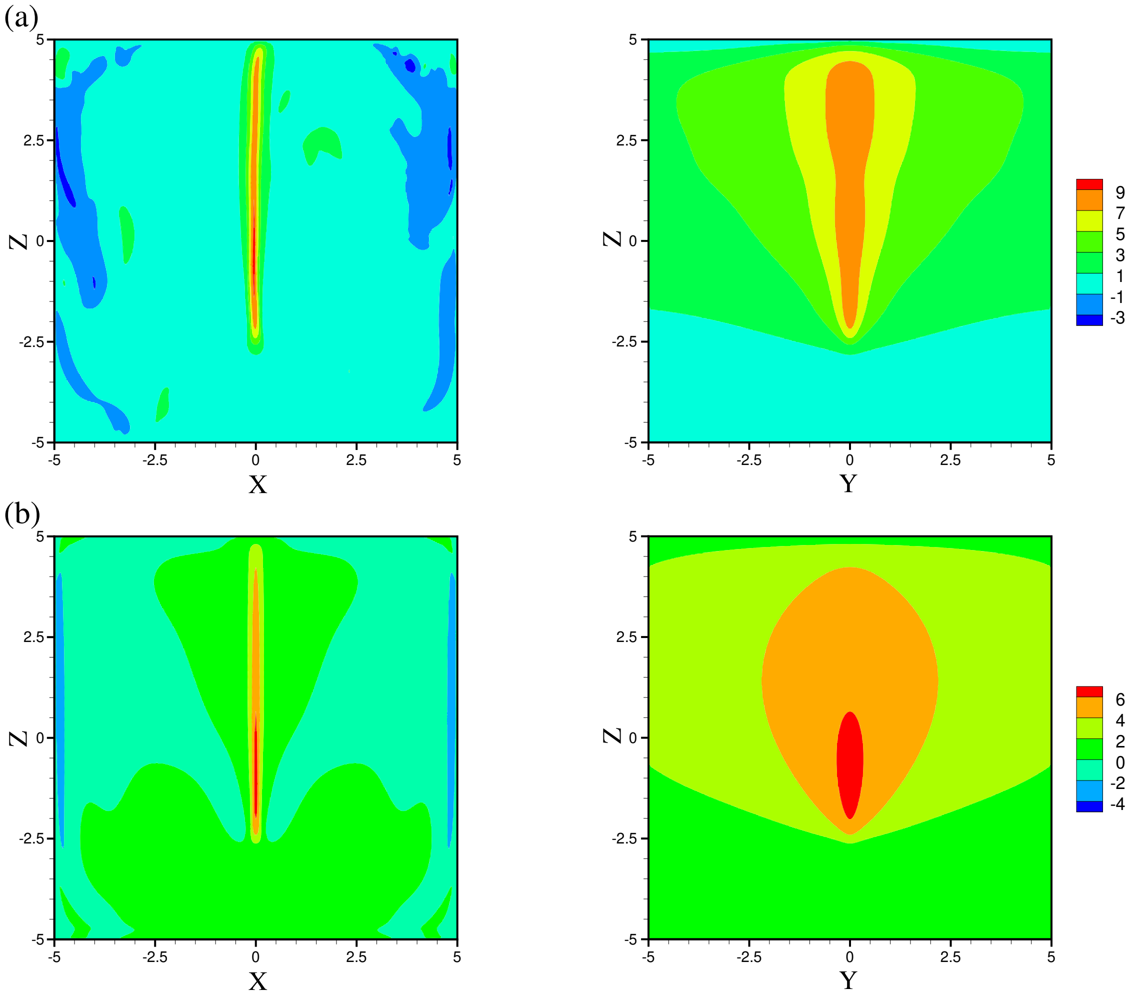

Figure 6.8: Two-dimensional vertical velocity u_z contours at vertical mid-planes for Ha = 200 *(a)* and Ha = 400 *(b)* and Ha = 100 with horizontal imposed magnetic field

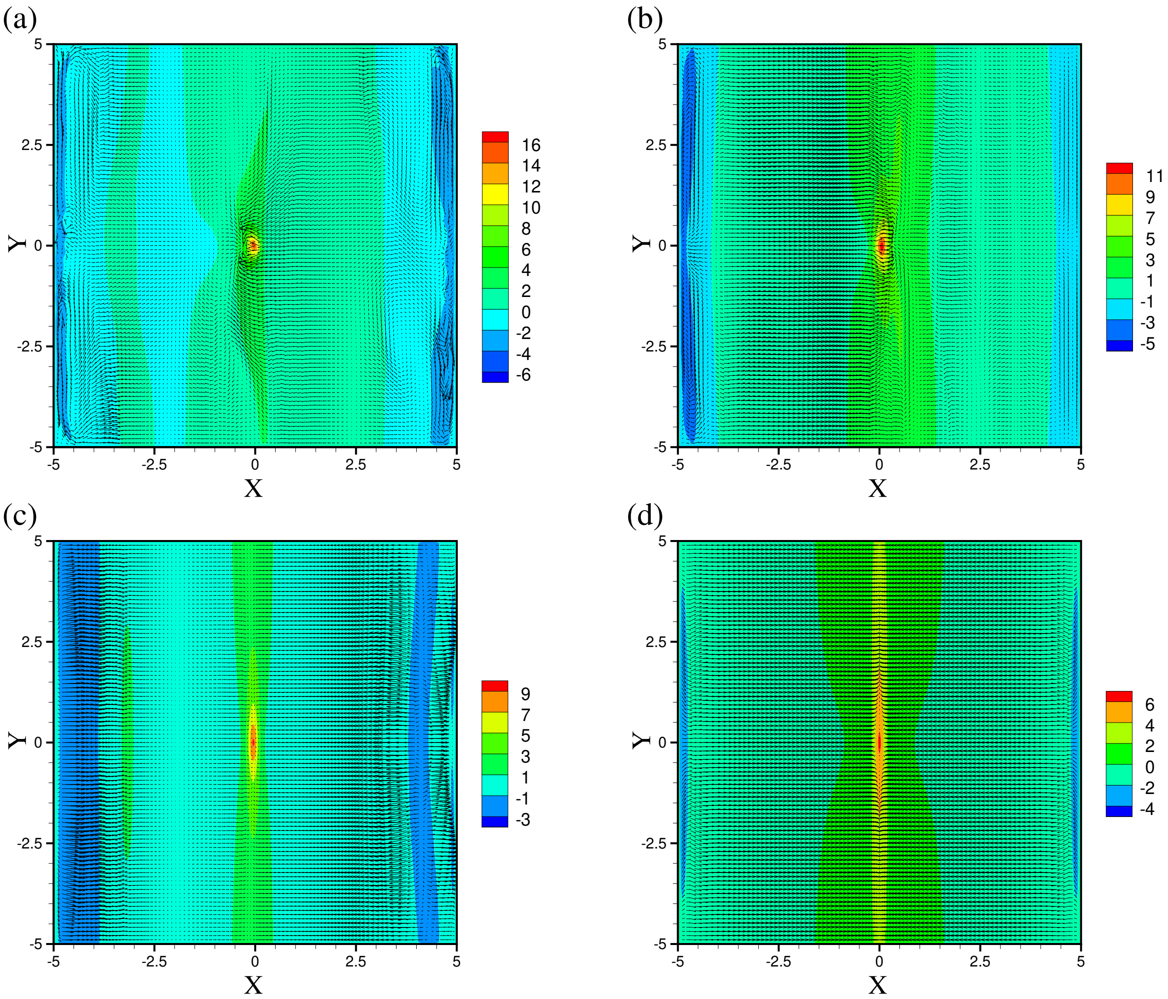

Figure 6.9: Two-dimensional vertical velocity u_z contours at the horizontal mid-plane for Ha = 50 *(a)*, Ha = 100 *(b)*, Ha = 200 *(c)* and Ha = 400 *(d)* with horizontal imposed magnetic field. In-plane velocity vectors are also shown.

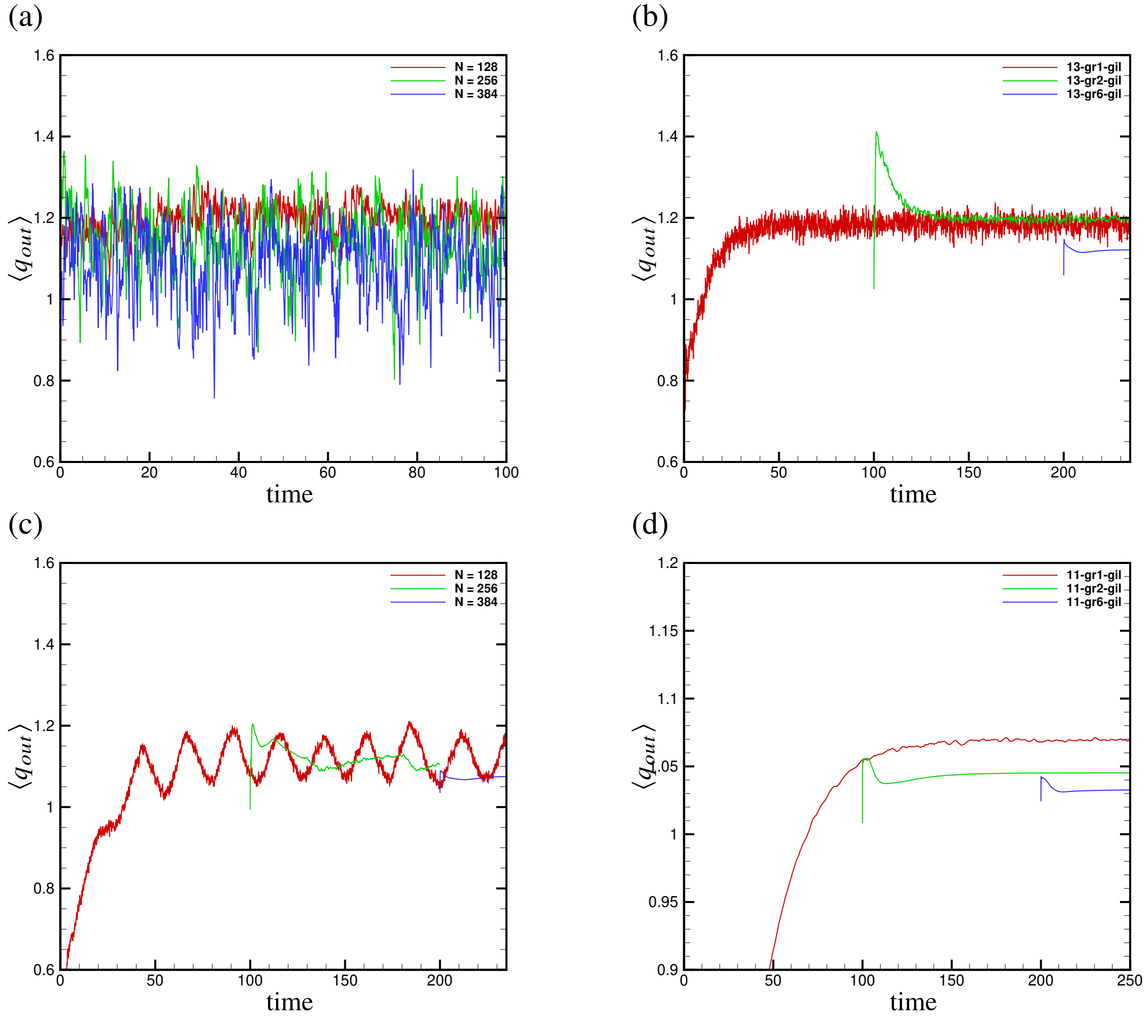

Figure 6.10: Time signals of $\langle q_{out} \rangle$ for $Ha = 0$ *(a)*, $Ha = 50$ *(b)*, $Ha = 100$ *(c)*, and $Ha = 200$ *(d)* when magnetic field is applied vertically. These results are for Gaussian-like heat generation and $\langle q_{out} \rangle$ is calculated using volume integral of $\nabla^2 T$.

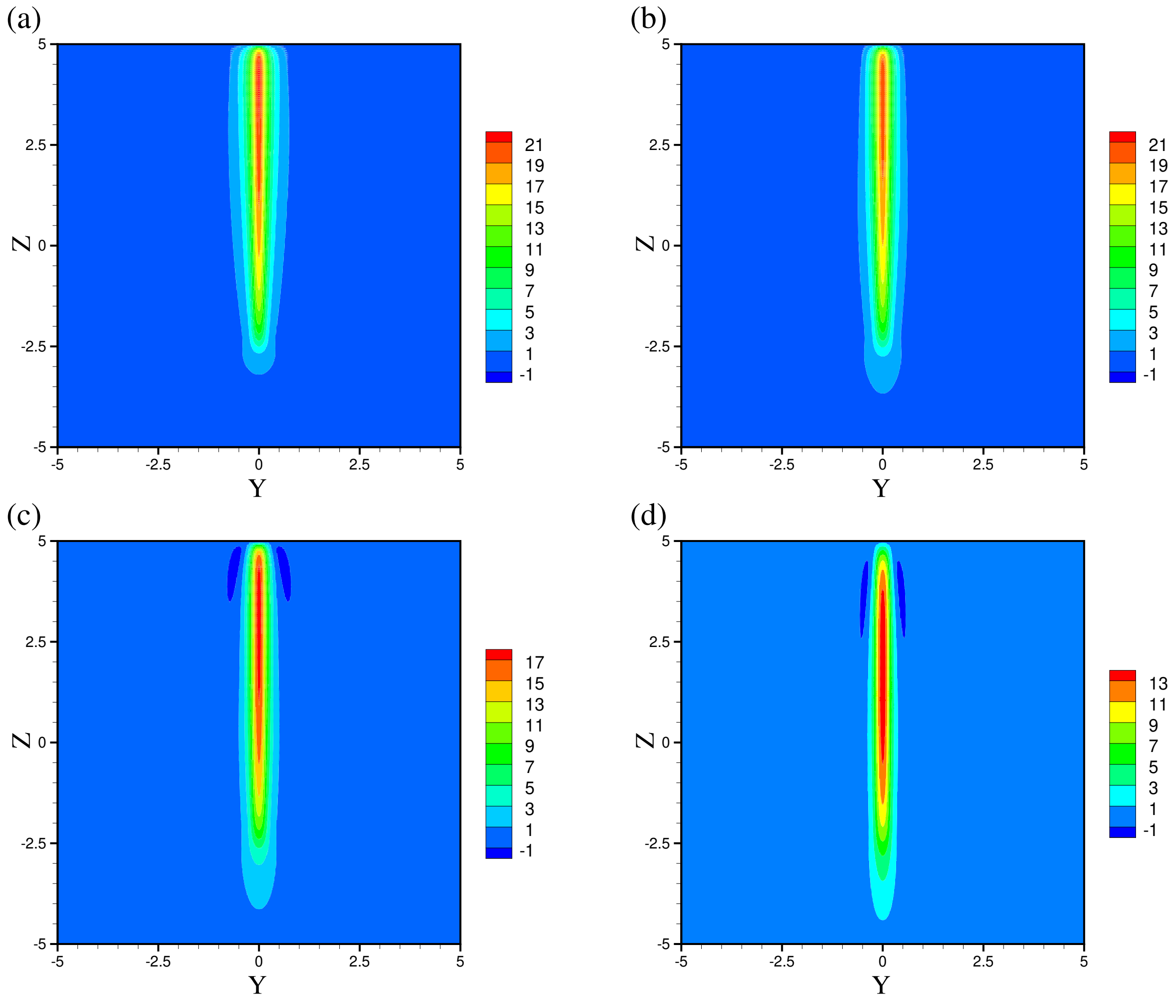

Figure 6.11: Two-dimensional vertical velocity u_z contours at one of the vertical mid-planes for Ha = 50 *(a)*, Ha = 100 *(b)*, Ha = 200 *(c)* and Ha = 400 *(d)* with horizontal imposed magnetic field. In-plane velocity vectors are also shown.

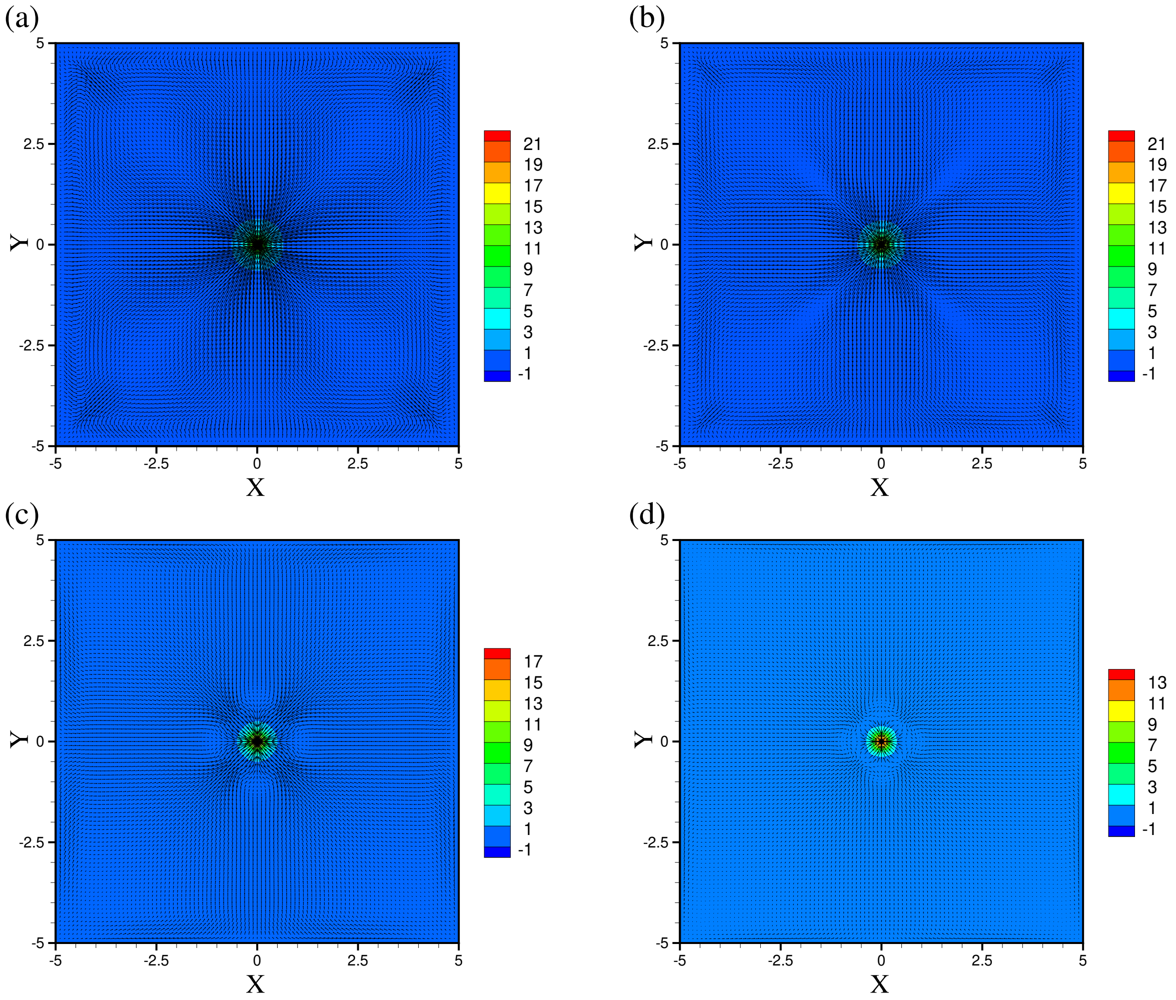

Figure 6.12: Two-dimensional vertical velocity u_z contours at the horizontal mid-plane for $Ha = 50$ *(a)*, $Ha = 100$ *(b)*, $Ha = 200$ *(c)* and $Ha = 400$ *(d)* with horizontal imposed magnetic field. In-plane velocity vectors are also shown.

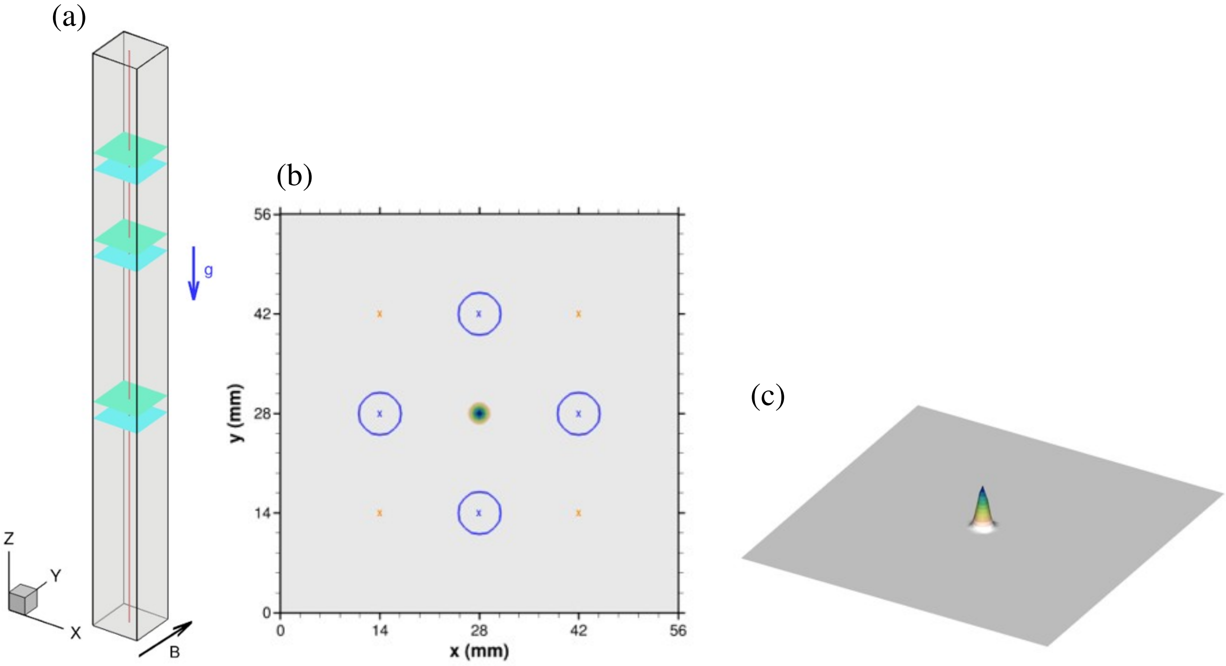

Figure 6.13: The setup for the study of the thermal plume generated by heat flux from a thin wire. The picture (a) demonstrates a 3D representation of the domain. The heated wire is shown in red. The blue and green cross-sections, show the location of the planes in which data gathering is performed. The picture (b) shows the exact location of the data probing points. In the experiment, data is gathered at the locations marked by a blue "X". The circle around them represents the uncertainty in the location of measurement. In the numerical setup time signal of temperature and vertical velocity is recorded at both orange and blue "X" locations. Picture (c) illustrates the values of volumetric heat generation q at any given horizontal slice.

6.2 Heat generation by thin wire

The setup for this part is inspired by an ongoing experiment, done by our colleagues at the Joint Institute of High Temperatures in Russia, which consists of an elongated vertical box with a square base containing mercury. The aspect ratio of the box is 1:1:12.32, with a square base of $56mm \times 55mm$. There is a thin wire located in the middle of the box and is stretched from bottom to the top. Electric current passes through the wire and the generated heat is transferred to the liquid metal. There is an external transverse uniform magnetic field applied to the box. All walls are electrically insulating. An illustration of this setup is shown in figure 6.13.

In this setup, in addition to recording the values representing the total state of the flow,

Property	$L_x \times L_y \times L_z$	Ra	Pr	Ha
Value	$2 \times 2 \times 24.64$	8×10^5	0.024	300, 600

Table 6.3: Non-dimensional geometry and parameters of the plume generated by a thin wire, (see text for a detailed discussion and definition of Ra, Pr, and Ha in (2.30)).

temperature and velocity components are also recorded at points shown in figure 6.13. Table 6.3 list the non-dimensional parameters used to study this problem. Calculated Ra and Ha numbers correspond to total heat generation of $250W$ and magnetic field intensity of $0.818T$, respectively.

In the numerical setup, since the wire diameter is much smaller than the typical length scale of the flow, its presence is neglected. The volumetric heat generation function at a horizontal cross section is shown in figure 6.13. Our preliminary results showed the formation of the plume starts by an increase in the temperature of the liquid metal, and subsequently an upward motion of liquid near the wire. Due to the presence of the magnetic field the plume, the gradient of the velocity parallel to the direction of magnetic field is small, on the other hand temperature distribution is elongated in direction perpendicular to the magnetic field. Figure 6.14 illustrates the vertical velocity and temperature fields in a horizontal plane.

To perform this study, due the problems mentioned in the section 6.1, the numerical grid is chosen to be uniform in all three directions. The grids used are listed in table 6.4. Using the grids #1 and #2, preliminary study of the problem was done. The results showed that the introducing magnetic field at $Ha = 300$ will result in the oscillating plume similar to the case of point heat source. Increasing the magnetic field intensity to $Ha = 600$ resulted in a complete suppression of fluctuations and a steady state flow. This, behavior however was not expected from the experimental results. To study the effect of surrounding disturbance, a random noise was added to the flow of $Ha = 600$ at every time step, which resulted in some fluctuations at the beginning but the magnetic field effects managed to dampen the amplitude of those fluctuations as well.

Grid #	N_x	N_y	N_z	Clustering		
				x	y	z
1	64	64	64	$\gamma = 0$	$\gamma = 0$	$\gamma = 0$
2	96	96	96	$\gamma = 0$	$\gamma = 0$	$\gamma = 0$
3	128	128	128	$\gamma = 0$	$\gamma = 0$	$\gamma = 0$

Table 6.4: Different grid parameters used for grid sensitivity study of artificially generated plume by hot wire. The last three columns show the types and parameters of grid clustering in each direction: blended Chebyshev and uniform grids (3.1) with the weight γ, hyperbolic tangent (3.2) with the clustering coefficient A, and a purely uniform grid $\gamma = 0$.

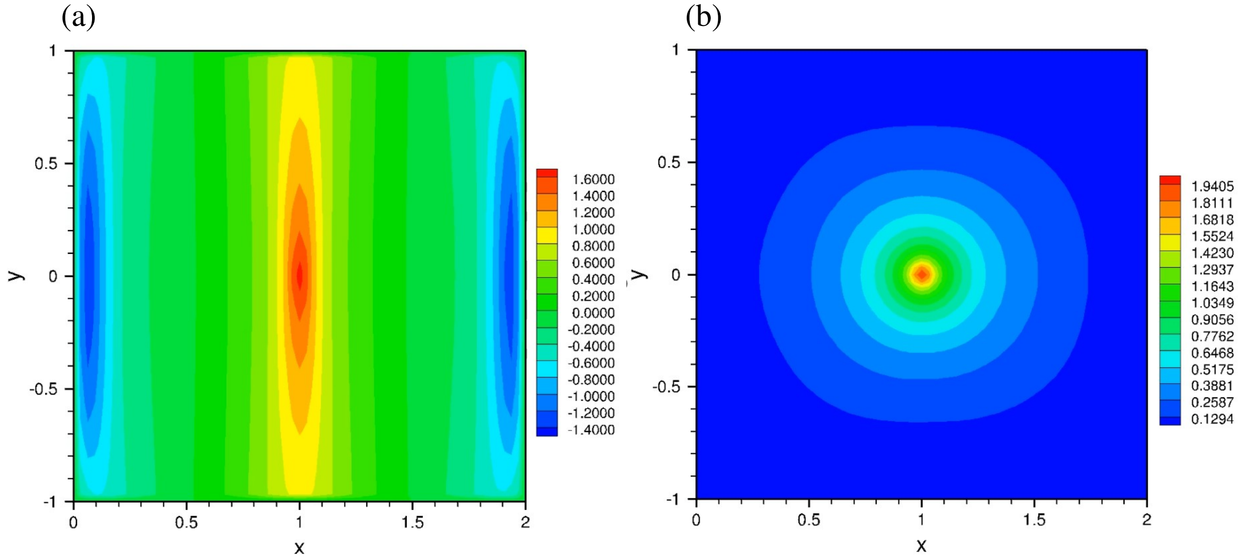

Figure 6.14: Vertical velocity (a) and temperature (b) fields in a horizontal cross section for the case with inward heat flux generation by a thin wire at $Ra = 8 \times 10^5$ and $Ha = 300$.

CHAPTER 7

Conclusion and Future Work

This dissertation presents a comprehensive study of magnetoconvection in systems with walls of finite electrical conductivity. The research focuses on understanding the intricate interaction between thermal convection and magnetic fields in electrically conducting fluids, such as liquid metals, within confined spaces. The primary contributions of this study are the development and validation of a robust numerical solver, a detailed parametric study on the effects of wall electrical conductivity, and an investigation into the dynamics of thermal plumes in strong magnetic fields.

7.1 Tensor-Product-Thomas Solver and Verification

A robust numerical solver based on a second-order finite difference scheme and the Tensor-product-Thomas (TPT) method was developed. This solver efficiently handles the boundary conditions associated with walls of finite electrical conductivity without iterative processes. The accuracy of the solver was validated through comparisons with established results for both electrically conducting and insulating walls, ensuring the reliability of the numerical simulations conducted in subsequent chapters.

7.2 Effect of Walls of Finite Electrical Conductivity

A detailed parametric study was conducted to investigate the effects of wall electrical conductivity on magnetoconvection. Various configurations were explored, including cases where all walls have the same electrical conductivity and scenarios with only specific walls being electrically conductive. The results revealed significant changes in the flow field and heat transfer patterns, underscoring the importance of considering wall conductivity in magnetoconvection studies.

Future exploration of other parameters such as Ra, can provide a deeper understanding of the internal magnetoconvection flows under bounded by electrically conducting walls. Another avenue to explore further in this problem is studying the effect of magnetic field direction as well as initial condition on the development of the flow, especially flow with low to moderate Ha, which shown to be sensitive to such changes.

7.3 Dynamics of A Thermal Plume Affected by A Magnetic Field

The dynamics of thermal plumes affected by magnetic fields were studied for two different plume generation configurations: a point heat source and a line heat source (e.g., thin wire). The study examined the effect of the magnetic field direction on the development of the flow. Results showed that a transverse magnetic field induces transient, oscillating plumes, with the transient behaviors decreasing as the magnetic field intensity increases. In contrast, a vertical magnetic field resulted in a completely different behavior. The study of artificially generated plume using a hot wire under the influence of a transverse impose magnetic field, confirmed the observation of the study of the plume generated by a point heat source. Both started with an oscillation and as intensity of the magnetic field increased the suppression of the flow became stronger until the flow is completely steady state.

Building on the findings of this study, several avenues for future research are identified. Extended studies on the dynamics of thermal plumes in different configurations and with varying magnetic field strengths are necessary. In addition to changing the parameters, a grid clustering method should be developed to increase the accuracy of numerical studies. It is worth mentioning adaptive mesh refinement methods can be used to increase accuracy of the grid at high gradient areas, however implementing such methods using the current solver was not feasible. The presented results are extremely helpful in identifying the regions that can benefit from grid clustering. Lastly, the effect of the wall conductivity on these plumes can be studied.

BIBLIOGRAPHY

[1] Peter Alan Davidson. *Introduction to magnetohydrodynamics*. Cambridge University Press, 2016.

[2] Nigel Oscar Weiss and Michael Richard Edward Proctor. *Magnetoconvection*. Cambridge Un. Press, 2014.

[3] Kevin Cukierski and Brian G Thomas. Flow control with local electromagnetic braking in continuous casting of steel slabs. *Metallurgical and Materials Transactions B*, 39(1):94–107, 2008.

[4] Douglas H Kelley and Tom Weier. Fluid mechanics of liquid metal batteries. *Applied Mechanics Reviews*, 70(2):020801, 2018.

[5] Y. Shen and O. Zikanov. Thermal convection in a liquid metal battery. *Theor. Comp. Fluid Dyn.*, 30(4):275–294, 2016.

[6] Hiroyuki Ozoe. *Magnetic convection*. London: Imperial College Press, 2005.

[7] Abdou, Mohamed and Morley, Neil B and Smolentsev, Sergey and Ying, Alice and Malang, Siegfried and Rowcliffe, Arthur and Ulrickson, Mike. Blanket/first wall challenges and required R&D on the pathway to DEMO. *Fusion Engineering and Design*, 100:2 – 43, 2015.

[8] Chiara Mistrangelo, Leo Bühler, Ciro Alberghi, Serena Bassini, Luigi Candido, Cyril Courtessole, Alessandro Tassone, Fernando R Urgorri, and Oleg Zikanov. MHD R&D Activities for Liquid Metal Blankets. *Energies*, 14(20):6640, 2021.

[9] Vittorio Coen. Lithium-lead eutectic as breeding material in fusion reactors. *Journal of nuclear materials*, 133:46–51, 1985.

[10] Chiara Mistrangelo and Leo Buehler. *Magnetoconvection in HCLL blankets*, volume 7672. KIT Scientific Publishing, 2014.

[11] Oleg Zikanov, Ivan Belyaev, Yaroslav Listratov, Peter Frick, Nikita Razuvanov, and Valentin Sviridov. Mixed convection in pipe and duct flows with strong magnetic fields. *Applied Mechanics Reviews*, 73(1):010801, 2021.

[12] Müller, Ulrich and Bühler, Leo. *Magnetohydrodynamics in channels and containers*. Springer, Berlin, 2001.

[13] L Bühler. Laminar buoyant magnetohydrodynamic flow in vertical rectangular ducts. *Physics of Fluids*, 10(1):223–236, 1998.

[14] T. Tagawa, G. Authié, and R. Moreau. Buoyant flow in long vertical enclosures in the presence of a strong horizontal magnetic field. Part 1. Fully- established flow. *Eur. J. Mech. B/Fluids*, 21(3):383–398, 2002.

[15] A Sterl. Numerical simulation of liquid-metal mhd flows in rectangular ducts. *J. Fluid Mech.*, 216:161–191, 1990.

[16] Guillaume Authié, Toshio Tagawa, and René Moreau. Buoyant flow in long vertical enclosures in the presence of a strong horizontal magnetic field. Part 2. Finite enclosures. *European Journal of Mechanics-B/Fluids*, 22(3):203–220, 2003.

[17] Ulrich Burr and Ulrich Müller. Rayleigh–Bénard convection in liquid metal layers under the influence of a horizontal magnetic field. *J. Fluid Mech.*, 453:345–369, 2002.

[18] Ivan Di Piazza and Michele Ciofalo. MHD free convection in a liquid-metal filled cubic enclosure. I. Differential heating. *International Journal of Heat and Mass Transfer*, 45(7):1477–1492, 2002.

[19] Zhi-Hong Liu, Long Chen, Ming-Jiu Ni, and Nian-Mei Zhang. Effects of magnetohydrodynamic mixed convection on fluid flow and structural stresses in the DCLL blanket. *Int. J. Heat Mass Transf.*, 135:847–859, 2019.

[20] Chiara Mistrangelo and Leo Bühler. Numerical study of fundamental magnetoconvection phenomena in electrically conducting ducts. *IEEE Trans. Plasma Sci.*, 40(3):584–589, 2011.

[21] Chiara Mistrangelo, Leo Bühler, and Giacomo Aiello. Buoyant-MHD flows in HCLL blankets caused by spatially varying thermal loads. *IEEE Trans. Plasma Sci.*, 42(5):1407–1412, 2014.

[22] Tyler J Rhodes, Gautam Pulugundla, Sergey Smolentsev, and Mohamed Abdou. 3D modelling of MHD mixed convection flow in a vertical duct with transverse magnetic field and volumetric or surface heating. *Fusion Eng. Des.*, 160:111834, 2020.

[23] E. Mas de les Valls, L. Batet, V. de Medina, and L. A. Sedano. MHD thermofluid flow simulation of channels with a uniform thermal load as applied to HCLL breeding blankets for fusion technology. *Magnetohydrodynamics*, 48(1), 2012.

[24] Hai-Tao Zhu, Long Chen, and Ming-Jiu Ni. Effects of wall conductivities on magnetoconvection in a cube. *Physical Review Fluids*, 9(4):043701, 2024.

[25] Dmitry Krasnov, Ali Akhtari, Oleg Zikanov, and Jörg Schumacher. Tensor-product-thomas elliptic solver for liquid-metal magnetohydrodynamics. *Journal of Computational Physics*, 474:111784, 2023.

[26] R. Moreau. *Magnetohydrodynamics*. Kluwer Academic Publishers, 1990.

[27] H. Branover. *Magnetohydrodynamic Flow in Ducts*. Wiley, Hoboken NJ, New York, 1978.

[28] P.L. Kirillov, M.I. Terentieva, and N.B. Deniskina. *Thermophysical properties of materials for nuclear engineering, 2nd ed. (in russian)*. Moscow, 2007.

[29] John S Walker. Magnetohydrodynamic flows in rectangular ducts with thin conducting walls. Part I: Constant area and variable area ducts with strong uniform magnetic fields. *Journal de Mécanique*, 20:79–112, 1981.

[30] Dmitry Krasnov, Oleg Zikanov, and Thomas Boeck. Comparative study of finite difference approaches to simulation of magnetohydrodynamic turbulence at low magnetic Reynolds number. *Computers & fluids*, 50:46–59, 2011.

[31] Oleg Zikanov, Yaroslav I Listratov, and Valentin G Sviridov. Natural convection in horizontal pipe flow with strong transverse magnetic field. *Journal of Fluid Mechanics*, 720:486–516, 2013.

[32] Helena Vitoshkin and Alexander Yu Gelfgat. On Direct and Semi-Direct Inverse of Stokes, Helmholtz and Laplacian Operators in View of Time-Stepper-Based Newton and Arnoldi Solvers in Incompressible CFD. *Communications in Computational Physics*, 14(4):1103–1119, 2013.

[33] Robert E Lynch, John R Rice, and Donald H Thomas. Direct solution of partial difference equations by tensor product methods. *Numerische Mathematik*, 6(1):185–199, 1964.

[34] Alexander Yu Gelfgat. Time-dependent modeling of oscillatory instability of three-dimensional natural convection of air in a laterally heated cubic box. *Theoretical and Computational Fluid Dynamics*, 31(4):447–469, 2017.

[35] Alexander Yu Gelfgat and Oleg Zikanov. Computational modeling of magnetoconvection: Effects of discretization method, grid refinement and grid stretching. *Computers & Fluids*, 175:66–82, 2018.

[36] Oleg Zikanov. *Essential computational fluid dynamics, 2nd Ed.* Wiley, Hoboken, NJ, 2019.

[37] Oleg Zikanov, Dmitry Krasnov, Thomas Boeck, and Semion Sukoriansky. Decay of turbulence in a liquid metal duct flow with transverse magnetic field. *J. Fluid Mech.*, 867:661–690, 2019.

[38] J. H. Ferziger and M. Perić. *Computational methods for fluid dynamics*. Springer, 2002.

[39] L Leboucher. Monotone scheme and boundary conditions for finite volume simulation of magnetohydrodynamic internal flows at high hartmann number. *Journal of Computational Physics*, 150(1):181–198, 1999.

[40] Guillaume Authié. *Convection naturelle sous champ magnétique en cavité verticale élancée-Application aux couvertures des réacteurs de fusion*. PhD thesis, Institut National Polytechnique de Grenoble, 2002.

[41] S Smolentsev, Santiago Badia, R Bhattacharyay, L Bühler, L Chen, Q Huang, H-G Jin, D Krasnov, D-W Lee, E Mas De Les Valls, et al. An approach to verification and validation of MHD codes for fusion applications. *Fusion Engineering and Design*, 100:65–72, 2015.

[42] Peter Huang, Rupanshi Chhabra, Ramakanth Munipalli, Gautam Pulugundla, Charlie Kawczynski, and Sergey Smolentsev. A comprehensive high performance predictive tool for fusion liquid metal hydromagnetics. Technical report, HyPerComp Inc., Westlake Village, CA (United States), 2017.

[43] Najmeh Foroozani, Dmitry Krasnov, and Jörg Schumacher. Turbulent convection for different thermal boundary conditions at the plates. *Journal of Fluid Mechanics*, 907:A27, 2021.

[44] Ali Akhtari, Oleg Zikanov, and Dmitry Krasnov. Magnetoconvection in a long vertical enclosure with walls of finite electrical conductivity. *arXiv preprint arXiv:2403.03899 - Accepted in International Journal of Thermal Sciences*, 2024.

[45] Jie Mao, Yang Cheng, and Liming Xie. Natural convection of MHD flow in a long vertical closed duct with different wall conductance ratios. *Magnetohydrodynamics (0024-998X)*, 57(4), 2021.

[46] D Suarez, Andrei Khodak, E Mas de les Valls, and L Batet. A formal verification and validation of a low magnetic Reynolds number MHD code for fusion applications. *IEEE Transactions on Plasma Science*, 50(11):4206–4212, 2022.

[47] Dmitry Krasnov, Oleg Zikanov, Maurice Rossi, and Thomas Boeck. Optimal linear growth in magnetohydrodynamic duct flow. *Journal of Fluid Mechanics*, 653:273–299, 2010.

[48] Bryan Travis and Peter Olson. Convection with internal heat sources and thermal turbulence in the earth's mantle. *Geophysical Journal International*, 118(1):1–19, 1994.

[49] John Stewart Turner. *Buoyancy effects in fluids*. Cambridge university press, 1973.

[50] VN Kurdyumov and A Linan. Free convection from a point source of heat, and heat transfer from spheres at small grashof numbers. *International journal of heat and mass transfer*, 42(20):3849–3860, 1999.

[51] RH Hernandez. Natural convection in thermal plumes emerging from a single heat source. *International Journal of Thermal Sciences*, 98:81–89, 2015.

[52] Chaojie Zhang, Sven Eckert, and Gunter Gerbeth. Modification of bubble-driven liquid metal flows under the influence of a dc magnetic field. *ISIJ international*, 47(6):795–801, 2007.

[53] X Miao, D Lucas, Z Ren, S Eckert, and G Gerbeth. Numerical modeling of bubble-driven liquid metal flows with external static magnetic field. *International Journal of Multiphase Flow*, 48:32–45, 2013.

[54] R. Akhmedagaev, O. Zikanov, D. Krasnov, and J. Schumacher. Rayleigh-Bénard convection in strong vertical magnetic field: flow structure and verification of numerical method. *Magnetohydrodynamics*, 56(2-3):157–165, 2020.

[55] Anna Kraszewska and Janusz Donizak. An analysis of a laminar-turbulent transition and thermal plumes behavior in a paramagnetic fluid subjected to an external magnetic field. *Energies*, 14(23):7972, 2021.

[56] Olga Shishkina and Claus Wagner. A fourth order accurate finite volume scheme for numerical simulations of turbulent rayleigh–bénard convection in cylindrical containers. *Comptes Rendus Mécanique*, 333(1):17–28, 2005.

[57] Jörg Schumacher, Janet D Scheel, Dmitry Krasnov, Diego A Donzis, Victor Yakhot, and Katepalli R Sreenivasan. Small-scale universality in fluid turbulence. *Proceedings of the National Academy of Sciences*, 111(30):10961–10965, 2014.

[58] PJ Sakievich, YT Peet, and RJ Adrian. Large-scale thermal motions of turbulent rayleigh–bénard convection in a wide aspect-ratio cylindrical domain. *International Journal of Heat and Fluid Flow*, 61:183–196, 2016.

[59] Xing-Xing Yu, Jie Zhang, and Ming-Jiu Ni. Numerical simulation of the rayleigh-benard convection under the influence of magnetic fields. *International Journal of Heat and Mass Transfer*, 120:1118–1131, 2018.

[60] Ahmed F Ghoniem, Issam Lakkis, and Marios Soteriou. Numerical simulation of the dynamics of large fire plumes and the phenomenon of puffing. In *Symposium (International) on Combustion*, volume 26, pages 1531–1539. Elsevier, 1996.

[61] A Hamins, JC Yang, and T Kashiwagi. An experimental investigation of the pulsation frequency of flames. In *Symposium (international) on combustion*, volume 24, pages 1695–1702. Elsevier, 1992.

[62] X Jiang and KH Luo. Direct numerical simulation of the puffing phenomenon of an axisymmetric thermal plume. *Theoretical and computational fluid dynamics*, 14(1):55–74, 2000.